The Sunyaev-Zel'dovich Effect
as a Probe of the
Large Scale Structure of the Universe

Dissertation
submitted for the award of the degree of

Master of Philosophy
in
Physics

by

Asif Iqbal Ahangar

Under the Supervision of

Dr. Manzoor A. Malik

Department of Physics,

University of Kashmir, Srinagar, 190 006

February, 2012

Acknowledgements

First of all, I am grateful to my supervisor for his continuous support and guidance in the early stages of my research to ongoing advice and encouragement. This has been invaluable on both academic as well as personal level. His wisdom, knowledge and commitment to the highest standards inspired and motivated me a lot. Additionally I thank prof. Javid Ahmed Sheikh and Ex H.O.D prof. Farooq Ahmad for boosting my knowledge in my M.Sc. years. I am thankful to Dr. Waseem Bari for his useful comments.

I am forever thankful to my parents for their undivided support and interest. They inspired and encouraged me to go my own way. I am eternally grateful to god for making me part of them. Also I would like to take this opportunity to thank my loving brother Atif Iqbal for gifting me some expensive foreign books.

I would like to thank seniors Raja Nissar and Waheed Ahmed for helping me in many Linux softwares. I am also extremely indebted to Abdul Wahid and Ajaz Ahmad for their advices. Special thanks to my special friends Shabir Ahamed, Inayat Bhat, Aashiq Hussian and Mubashir Hamid with whom I shared ups and downs of my life. Not to forget, great appreciation go to the rest of my colleagues Shuja Rasool, Bilal Ahmed, Asloob Ahmad, Sajad Bhat and Bilal Malik and others with whom I shared joyful memories.

I am extremely thankful to the officials at Inter University Centre for Astronomy and Astrophysics (IUCAA) for their hospitality during my stay there. My sincere thanks to Professor Tarun Souradeep for his useful advice and suggestions.

This note remains incomplete without the mention of my experience at Soura. It is there I made acquaintances with some wonderful people. Among these it is a pleasure to thank Ajaz Ahamed, Ajaz Ahangar, Hilal Ahmed and Sunil Bhat for helping me in every possible way. Above all I will never forget my first students there.

Lastly, I alone assumes full responsibility for any errors or inadequacies, if present.

Asif Iqbal Ahangar

Post Graduate Department of Physics
University of Kashmir, Srinagar

Certificate

This is to certify that the dissertation entitled "*The Sunyaev-Zel'dovich Effect as a Probe of the Large Scale Structure of the Universe*" submitted by *Asif Iqbal Ahangar*, in partial fulfillment for the award of the degree of *Master of Philosophy* in *Physics*, is the original research work carried out by him under my supervision and guidance. It is further certified that the dissertation has not been submitted for the award of M. Phil. or any other degree to this University or any other University. The scholar has attended the department for statutory period as required under rules.

Dr. Manzoor A. Malik
(*Supervisor*)

Dr. Manzoor A. Malik
(*Head of the department*)

Contents

List of Figures

Chapter 1

General Introduction

The Sunyaev-Zel'dovich effect (S-Z effect) is a distortion in the cosmic microwave background radiation (CMBR) [1, 2, 3, 4] due to the inverse Compton scattering of CMBR photons by the electrons in the intra-cluster medium (ICM) [5, 6, 7, 8, 9]. The effect is an interaction between Cosmic Microwave Background Radiation photons and the free electrons in the dense cores of galaxy clusters. These cores of clusters of galaxies are thought to contain hot ionized gas at $\sim 10^7$K [10]. This hot ionized gas is visible as X-ray emission. The free electrons in the gas contain a significant amount of kinetic energy, making them good sources for S-Z effect.

Generally speaking, the interaction between photons and the free electrons is called Compton scattering. The inverse process where a free electron scatters off a photon is called inverse Compton scattering (S-Z effect). Some of the kinetic energy that the energetic electrons possess is transferred to the photons. This is called up-scattering of photons. These scatterings will cause changes in the apparent brightness of the CMBR, modifying the spectrum of the CMBR photons. There are two ways by which S-Z effect can distort the CMBR, namely the thermal S-Z effect [5] and the kinematic S-Z effect [6]. The first occurs due to scattering from random motion of the hot electrons whereas the second is due to the scattering of the CMBR photons owing to the bulk motions of clusters. Some excellent recent reviews on the physics of the S-Z effect have been given by Rephaeli, Birkinshaw, Holder et al., and Carlstrom et al. [8, 9, 11, 12, 13, 14]. Even though there is a tremendous amount of gas contained in a cluster of galaxies, the probability that a CMBR photon will interact with any of the electrons in the cluster gas is small. The S-Z effect is therefore subtle, changing the brightness of CMBR blackbody

spectrum by at most 0.1%. The spectral distortion has a distinct signature: in low frequency part of CMBR spectrum, the S-Z effect scattering process causes the brightness of the CMBR to be diminished towards clusters, producing "holes" in the background radiation field. The scattered photons are shifted to higher energies, producing an excess in the high frequency part of the CMBR spectrum. When S-Z effect was first proposed, it proved exceptionally difficult to detect; accurate measurements are now possible using experimental techniques developed over the last few decades [15].

The S-Z effect is best known for allowing the determination of cosmological parameters when combined with other observational techniques like X-ray measurements from the inter-cluster gas [16], weak lensing by the cluster potential [17] etc. For example, the cluster distances have been determined from the analysis of S-Z effect and X-ray data, providing, independent estimates of the Hubble constant, as well as a measure of of the angular diameter distance relation to high redshifts [18], where it is highly sensitive to cosmological parameters. Similarly, the S-Z effect and X-ray measurements will allow us tight constraints on the cluster gas-mass fractions that can be used to estimate Ω_m [19]. The power of the S-Z effect comes about because the effect is caused by scattering, rather than emission, and so scales with density of scattering electrons. A cluster of galaxies may therefore appear quite different in its X-ray and S-Z effect structures, and a comparison of those structures can provide interesting information on the physics of clusters and their atmospheres. A remarkable property of the S-Z effect is that its brightness depends only on the properties of cluster gas - unlike most emission mechanisms, the brightness of the S-Z Effect does not depend on redshift and does not suffer $(1 + z)^{-4}$ fading. This is because the effect is a fractional change in the brightness of the CMBR, and the CMBR's energy density itself increases with redshift as $(1 + z)^{-4}$, canceling out the dimming effect of cosmology. The total S-Z effect flux detected will be proportional to the total temperature-weighted mass and inversely proportional to the square of the angular distance. Recent work [20] shows that with precise determinations of S-Z source it may be possible to provide new and orthogonal constraints on the dark energy equation of state. Additionally, S-Z effect observations have been used to infer the presence and nature of dark matter in the large scale structures [21]. Besides, Sunyaev-Zel'dovich effect signal together with the gravitational lensing measurements have been used to test whether the cluster cores are in hydrostatic equilibrium, with the inference that departures from equilibrium are modest in cluster cluster cores. The kinematic S-Z effect is a unique and powerful cosmological tool because it is only known way to measure large-scale veloc-

ity fields at high redshifts [22]. The spectrum of kinematic S-Z effect is identical to the spectrum of intrinsic CMBR anisotropies. Therefore, the kinematic S-Z effect cannot be spectrally discriminated from intrinsic CMBR anisotropies. Fortunately, the CMBR fluctuations are dumped on arc-minute scales and can be effectively removed by applying a spatial filter. The S-Z effect has also been studied as a probe of black holes. Realization of the potential of S-Z effect has led to major improvements in the observational techniques and instruments, recent among which are the South Pole Telescope [23], APEX [24], SZA [25], ACT [26]. Besides Planck Surveyor Satellite is expected to provide an S-Z effect all-sky survey at unprecedented resolution that should find on the order $10^4 - 10^5$ clusters, most of them at $z < 1$. This upcoming information is not only precious for its astrophysical impact but it is also crucial for the possible cosmological use of galaxy clusters as a probe of the structure of universe. Because of the wealth of cosmological information that S-Z effect has given and promises to give in future, we, in this work, will study the secondary distortion due to S-Z effect, in different astrophysical contexts, as a probe of large scale structure of universe.

1.1   CMBR Power Spectrum

One of the major achievements of COBE observations was the detection of slight variation of CMBR temperature [3, 27]: first at 10^{-3} level associated with the motion of our local group of galaxies (dipole anisotropy), then at 10^{-5} level believed to be generated at the moment of last scattering by very tiny cosmological fluctuations, the ancestors of the present cosmological structures. CMBR signatures can be generally classified into two main components: primary and secondary anisotropies, separated by the Surface of Last Scattering. Both of these components include contributions from two distinctive phases: a surface marking the threshold of decoupling of ions and electrons from hydrogen atoms in primary signals, and a surface of reionization marking the start of multiphase secondary contributions through nonlinear structure evolution, star formation, and radiative feedback from the small scales to the large. Here, we present the basic formalism needed for a description of the CMBR anisotropy.

The CMBR temperature has a directional dependence $T(\theta, \phi)$ with an average of

$$< T >= \frac{1}{4\pi} \int T(\theta, \phi) d\theta d\phi = 2.725 \text{K}. \tag{1.1}$$

The fluctuations can be expressed as,

$$\frac{\delta T}{T}(\theta, \phi) \equiv \frac{T(\theta, \phi) - <T>}{<T>},$$ (1.2)

and have a root mean square value of

$$\left\langle \frac{\delta T}{T} \right\rangle^{1/2} \approx 1.1 \times 10^{-5},$$ (1.3)

after taking off 10^{-3} dipole anisotropy.

While studying the temperature anisotropies on the celestial sphere it is frequently expanded using a basis of spherical harmonics,

$$\frac{\delta T}{T} = \sum_{l=0}^{\infty} \sum_{m=-l}^{l} a_{lm} Y_{lm}(\theta, \phi),$$ (1.4)

where the sum runs over $l = 1, 2, 3......$ and $m = -l.....l$ giving $2l+1$ values of m for each l. The multipole number l represents the number of nodes (location of zero amplitude) between equator and poles, while m is the longitudinal node number. The basis functions obey orthonormality i.e.

$$\int Y_{lm}^* Y_{l'm'} d\Omega = \delta_{ll'} \delta_{mm'},$$ (1.5)

and the addition theorem i.e.

$$\sum_m Y_{lm}^* Y_{lm} = \sum_m |Y_{lm}(\theta, \phi)|^2 = \frac{2l+1}{4\pi}.$$ (1.6)

Since CMBR anisotropy is due to the primordial perturbations, and therefore it reflects their Gaussian nature. Because one gets the values of the a_{lm} from the other perturbation quantities through linear equations (in first-order perturbation theory), the a_{lm} are also Gaussian random variables. Since they represent a deviation from the average temperature, their expectation value is zero [1],

$$< a_{lm} >= 0,$$ (1.7)

and the quantity we want to calculate from theory is the variance $< |a_{lm}|^2 >$ to get the prediction for the typical size of the a_{lm}. The isotropic nature of the random process show

up in the a_{lm} so that these expectation values depend only on l not m (l are related to the angular size of the anisotropy pattern, whereas the m are related to orientation or pattern). Since $< |a_{lm}|^2 >$ is independent of m, we can define

$$C_l \equiv < |a_{lm}|^2 >= \frac{1}{2l+1} \sum_m < |a_{lm}|^2 >, \qquad (1.8)$$

and is called the (theoretical) angular power spectrum. It is analogous to the power spectrum $P(k)$ of density perturbations. For Gaussian perturbations, the C_l contains all the statistical information about the CMBR anisotropy and this is all we can predict from theory. Thus the analysis of the CMBR anisotropy consists of calculating the angular power spectrum from the observed CMBR and compare it to the C_l predicted by theory. The different a_{lm} are independent random variables, so that,

$$< a_{lm}^* a_{l'm'} >= \delta_{ll'} \delta_{mm'} C_l. \qquad (1.9)$$

From Eq. (1.4) we have,

$$
\begin{aligned}
\left\langle \left(\frac{\delta T}{T}\right)^2 \right\rangle &= \left\langle \sum_{lm} a_{lm} Y_{lm}(\theta, \phi) \sum_{l'm'} a_{l'm'}^* Y_{l'm'}^*(\theta, \phi) \right\rangle \\
&= \sum_{ll'} \sum_{mm'} Y_{lm} Y_{l'm'}^* < a_{lm} a_{l'm'}^* > \\
&= \sum_l C_l \sum_m |Y_{lm}(\theta, \phi)|^2 \\
&= \sum_l \frac{2l+1}{4\pi} C_l, \qquad (1.10)
\end{aligned}
$$

where we have used Eqs. (1.9) $\&$ (1.6).

Thus if we plot $\frac{(2l+1)C_l}{4\pi}$ on the linear l scale or $\frac{l(2l+1)C_l}{4\pi}$ on the logarithmic l scale, the area under curve gives the temperature variance, i.e. the expectation value for the squared deviation from the average temperature. It has become customary to plot the angular power spectrum as $\frac{l(l+1)C_l}{2\pi}$ which is neither of these, but for large l approximates the second case.

Eq. (1.10) represents the expectation value from the theory and thus it is same for all directions θ, ϕ. The actual, realized, value varies from one direction θ, ϕ to another. We can imagine ensemble of universes, otherwise like our own, but represents a different

realization of the same random process of producing the primordial perturbations. Then $<>$ represents the average over such an ensemble.

Now since theory predicts expectation values $< |a_{lm}|^2 >$ from the random process responsible for CMBR anisotropies, but we can observe only one realization of this random process, the set a_{lm} of our CMBR sky. We can define the observed angular power spectrum as the average,

$$\widehat{C}_l = \frac{1}{2l+1} \sum_m |a_{lm}|^2 \tag{1.11}$$

of these observed values.

The variance of the observed temperature anisotropy is the average of $\left(\frac{\delta T(\theta,\phi)}{T}\right)^2$ over the celestial sphere,

$$
\begin{aligned}
\frac{1}{4\pi} \int \left[\frac{\delta T(\theta,\phi)}{T}\right]^2 d\Omega &= \frac{1}{4\pi} \int d\Omega \sum_{lm} a_{lm} Y_{lm}(\theta,\phi) \sum_{l'm'} a^*_{l'm'} Y^*_{l'm'}(\theta,\phi) \\
&= \frac{1}{4\pi} \sum_{lm} \sum_{l'm'} a_{lm} a^*_{l'm'} \underbrace{\int Y_{lm}(\theta,\phi) Y^*_{l'm'}(\theta,\phi) d\Omega}_{\delta_{ll'}\delta_{mm'}} \\
&= \frac{1}{4\pi} \sum_l \underbrace{\sum_m |a_{lm}|^2}_{(2l+1)\widehat{C}_l} \\
&= \sum_l \frac{2l+1}{4\pi} \widehat{C}_l.
\end{aligned}
\tag{1.12}
$$

Contrast this with Eq. (1.10) which gives the variance of $\frac{\delta T}{T}$ at an arbitrary location on the sky over different realizations of the random process which produced the primordial perturbations; whereas Eq. (1.12) gives the variance of $\frac{\delta T}{T}$ of our given sky over the celestial sphere.

The expectation value of the observed spectrum $\widehat{C}_l$ is equal to C_l, the theoretical spectrum of Eq. (1.8), i.e.

$$< \widehat{C}_l >= C_l, \tag{1.13}$$

but its actual realized value is not, although we expect it to be close to the observed spectrum. The expected squared difference between $\widehat{C}_l$ and C_l is called the cosmic variance. Cosmic variance is small for large l because we have a large $(2l+1)$ statistical sample of a_{lm} available for calculating $\widehat{C}_l$ At this moment, the best current data comes from the
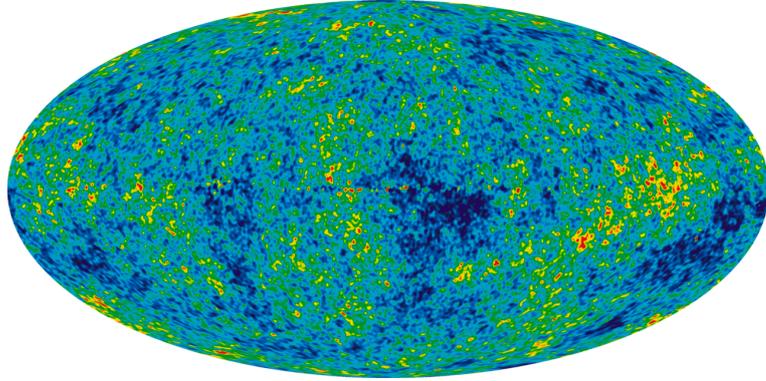
Figure 1.1: The Cosmic Microwave Background temperature fluctuations from the 7-year Wilkinson Microwave Anisotropy Probe data seen over the full sky. The image is a mollweide projection of the temperature variations over the celestial sphere. The average temperature is 2.725 Kelvin, and the colors represent the tiny temperature fluctuations, as in a weather map. Red regions are warmer and blue regions are colder by about 0.0002 degrees. Source-http://wmap.gsfc.nasa.gov/media/101080, NASA.

Wilkinson Microwave Anisotropy Probe (WMAP) [27]. The temperature map from the first seven year WMAP data is show in Fig. (1.1).

The temperature fluctuations in the CMBR at higher multipoles, $l \geq 2$ are generally interpreted as being mostly the result of perturbations in the density of the very early universe and then especially at the surface of last scattering. Though, all higher multipoles result from perturbations in the density, they do not have the same origin. Different regions in l have different physical origins. There are roughly 4 main regions as shown in Fig. (1.2), namely ISW rise ($l \lesssim 10$) [29], Sachs-Wolfe plateau ($10 \lesssim l \lesssim 100$) [30], Acoustic Peaks ($100 \lesssim l \lesssim 1000$) [31, 32] and the Damping Tail ($l \gtrsim 1000$) [33].

CMBR anisotropies induced by S-Z effect is the main source of secondary anisotropy on angular scales of few arc-minutes. Because of this and the great interest in this range of angular scale-multipoles $l > 1000$, the S-Z anisotropy has been studied extensively in the last few decades [34, 35, 36]. The basic goal has been to map its predicted l dependence in viable cosmological, large scale structure, and ICM gas models. The strong motivation for this is the need to accurately calculate the power spectrum of the full anisotropy in order to make precise global parameter determinations from stratospheric and satellite database. In addition, mapping the S-Z anisotropy will yield direct information on the evolution of the cluster population.
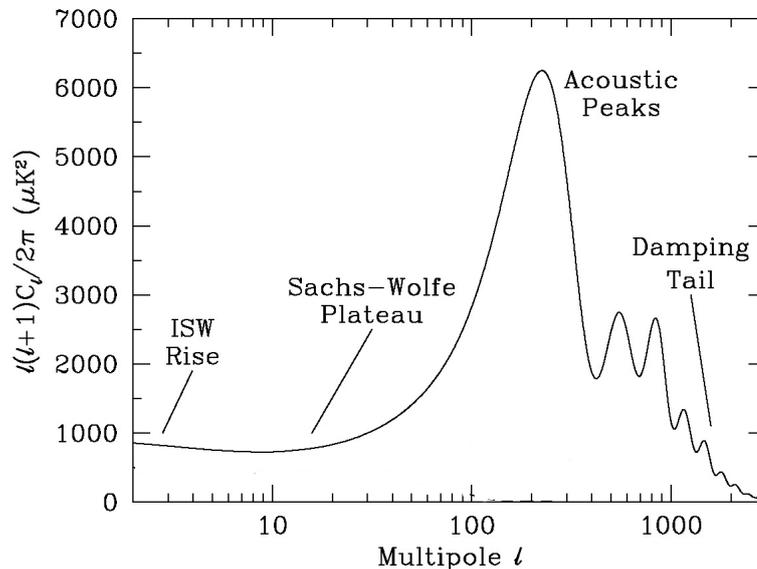
Figure 1.2: Plot of the theoretical CMBR anisotropy power spectrum, using a standard ΛCDM model. The x-axis is logarithmic here. The regions are labeled as in the text: the ISW Rise: Sachs-Wolfe Plateau: Acoustic Peaks: and Damping Tail [28].

1.2 Photon Scattering

The theoretical foundation of the Sunyaev-Zel'dovich effect was laid in the early 1970s by Sunyaev and Zel'dovich and is based on the interactions of photons and free electrons [37]. In this section, we will briefly discuss such interactions and energy changes accompanying them. When an energetic photon interacts with a charged particle such as an electron, it gives impulse transferring momentum, losing energy in the process. This is known as Compton scattering. One also encounters opposite effect, of energetic particles transferring momentum to low energy photons, which is known as inverse Compton scattering. These two processes can be thought as manifestation of the same process viewed in two different frame of references. If the observer is at rest with respect to energetic electron, the inverse Compton scattering would appear as a normal Compton scattering, since to the observer the photon would appear to be highly energetic and being scattered by a stationary particle.

We first consider scattering of a photon in rest frame of electron. Let the four momenta of photon before and after scattering be P_i and P_f respectively. And let the initial

and final four momenta of the electron be Q_i and Q_f. we then have,

$$\left. \begin{array}{ll} P_i = \left(\frac{\epsilon_i'}{c} \vec{n}_i, i\frac{\epsilon_i'}{c} \right), & P_f = \left(\frac{\epsilon_f'}{c} \vec{n}_f, i\frac{\epsilon_f'}{c} \right) \\ Q_i = (0, im_ec), & Q_f = \left(p, \frac{iE}{c} \right) \end{array} \right\}, \tag{1.14}$$

where $\vec{n}_i$ and $\vec{n}_f$ are the initial and final directions of photon.

According to four momentum conservation,

$$Q_f{}^2 = (P_i + Q_i - P_f)^2. \tag{1.15}$$

Using the fact that,

$$Q_i{}^2 = -m_ec^2, P^2 = 0, \tag{1.16}$$

we have,

$$P_i.P_f = Q_i.(P_i - P_f). \tag{1.17}$$

or

$$\frac{\epsilon_i'\epsilon_f'}{m_ec^2}(\vec{n}_i.\vec{n}_f - 1) = -\epsilon_i' + \epsilon_f'. \tag{1.18}$$

Let $\vec{n}_i.\vec{n}_f = \cos\theta'$, then we have,

$$\epsilon_f' = \frac{\epsilon_i'}{1 + \frac{\epsilon_i'}{m_ec^2}(1 - \cos\theta')}. \tag{1.19}$$

Solving the above equation, we get,

$$\lambda' - \lambda = \lambda_c(1 - \cos\theta'), \tag{1.20}$$

where the Compton wavelength is defined to be $\lambda_c = \frac{h}{m_ec}$. Note that $\lambda' > \lambda$ for all values of θ, in other words photon seems to always lose energy in the rest frame of electron (Compton scattering).

By using Binomial theorem ($\epsilon_i' \ll m_ec^2$), Eq. (1.19) can be written as,

$$\epsilon_f' = \epsilon_i' \left[1 - \frac{\epsilon_i'}{m_0c^2}(1 - \cos\theta') \right], \tag{1.21}$$

which on further simplification gives,

$$\frac{\Delta\epsilon'}{\epsilon'} = -\frac{\epsilon'}{m_e c^2} 1(-\cos\theta'). \tag{1.22}$$

In order to find the mean fractional change in energy, one has to average Eq. (1.22) over θ'. In the rest frame of the electron, the scattering has front-back symmetry, making $\cos\theta' = 0$. Hence the average fractional energy lost by the photon per collision is [38, 39],

$$\frac{<\Delta\epsilon'>}{<\epsilon'>} = -\frac{<\epsilon'>}{m_e c^2}. \tag{1.23}$$

When we transform to observer frame, the energy of scattered photon by Doppler formula is given as,

$$\epsilon_f = \gamma\epsilon'_f(1 + \beta\cos\theta'), \tag{1.24}$$

where γ is Lorentz factor. For an average angle of $\theta' = \frac{\pi}{2}$, we then have,

$$\epsilon_f \approx \gamma\epsilon'_f. \tag{1.25}$$

If we consider the low energy Thomson scattering where $\epsilon'_i << m_e c^2$, then $\epsilon'_i \approx \epsilon'_f$, so that,

$$\epsilon_f \approx \gamma\epsilon'_i. \tag{1.26}$$

Again using the Doppler formula, we have,

$$\epsilon'_i = \gamma\epsilon_i(1 - \beta\cos\theta). \tag{1.27}$$

For an average angle of $\theta = \frac{\pi}{2}$, which implies,

$$\epsilon'_i \approx \gamma\epsilon_i, \tag{1.28}$$

so from Eq. (1.26), we have,

$$\epsilon_f \approx \gamma^2\epsilon_i. \tag{1.29}$$

From the above discussion it is clear that , for relativistic electrons $(\gamma^2 - 1) >> \frac{\epsilon'_i}{m_e c^2}$, initially low energy photons gain energy by a factor of γ^2 in the observer frame at the expense of the kinetic energy of the electrons. This process, therefore, converts radio photons to UV photons, far-IR photons to X-ray photons, and optical photons to gamma-ray photons. The energy of the photon before scattering in the rest frame of electron, and

after scattering are in approximate ratios $1 : \gamma : \gamma^2$ [39].

1.3   Inverse Compton Power for Single Scattering

In the previous section we discussed how the energy of moving electrons decreases when it scatters photons. Now let us discusses the energy transfer for the case of a given isotropic distribution of photons scattering off a given isotropic distribution of electrons.

Let $dn = n(\epsilon)d\epsilon$ be the density of photons having energy in the range $d\epsilon$. But dn, in terms of the differential number of particles dN (Lorentz invariant), and the three dimensional volume element dV can be written as,

$$dn = \frac{dN}{dV}. \tag{1.30}$$

As the four dimensional volume element $dX = dx_0 dx_1 dx_2 dx_3 = dx_0 dV$ is Lorentz invariant, therefore $dn = \frac{dN}{dX}dx_0$ transforms like time component (x_0) of the photon position-vector. Further, since photon four momentum P_μ and position X_μ are parallel four-vectors (i.e., their spatial components are related to their time components in the same way), the ratio $\frac{dx_0}{p_0}$ is invariant. This in turn implies $\frac{dn}{\epsilon}$ is Lorentz invariant, since $\frac{dN}{dX}$ is invariant. In other words we can have,

$$\frac{dn}{\epsilon} = \frac{dn'}{\epsilon'}$$
$$\Rightarrow \frac{nd\epsilon}{\epsilon} = \frac{n'd\epsilon'}{\epsilon'}. \tag{1.31}$$

We assume the scattering in the rest frame of the electron is elastic (i.e. $\gamma h\nu << m_e c^2$), so that in the rest frame of electron , the total power emitted (scattered) is given by,

$$\frac{dE'_f}{dt'} = c\sigma_t \int \epsilon'_f n(\epsilon'_i)d\epsilon'_i, \tag{1.32}$$

where σ_t is the Thomson scattering cross section. Further $\frac{dE'_f}{dt'}$ is also invariant, since it too is the ratio of the same components of two parallel four vectors. Thus,

$$\frac{dE'_f}{dt'} = \frac{dE_f}{dt}. \tag{1.33}$$

From Eq. (1.31), we obtain,

$$\begin{aligned}
\frac{dE_f}{dt} &= c\sigma_t \int \epsilon'_f n(\epsilon'_i) d\epsilon'_i \\
&= c\sigma_t \int \epsilon'^2_i \frac{n(\epsilon_i)}{\epsilon_i} d\epsilon_i,
\end{aligned} \tag{1.34}$$

where we have used $\epsilon'_f \approx \epsilon'_i$. Now substituting $\epsilon'_i = \gamma\epsilon_i(1 - \beta\cos\theta)$ in above equation we get,

$$\frac{dE_f}{dt} = c\sigma_t\gamma^2 \int \epsilon_i(1 - \beta\cos\theta)^2 n(\epsilon_i) d\epsilon_i, \tag{1.35}$$

which refers solely to quantities in the observer frame. For an isotropic distribution of photons we have,

$$\left\langle (1 - \beta\cos\theta)^2 \right\rangle = 1 + \frac{1}{3}\beta^2, \tag{1.36}$$

since $< \cos\theta >=0$ and $< \cos\theta^2 >= \frac{1}{3}$. Thus Eq. (1.34) takes the form,

$$\frac{dE_f}{dt} = c\sigma_t\gamma^2 \left(1 + \frac{1}{3}\beta^2\right) U_{rad}, \tag{1.37}$$

where $U_{rad} = \int \epsilon_i n(\epsilon_i) d\epsilon_i$ is the initial photon or radiation density. Above equation gives the power in the scattered photons which are added to radiation field, but the scattering also removes energy from the radiation field at a rate $c\sigma_t U_{rad}$ for an isotropic photon distribution. Thus the difference between two rates must be supplied by the energy of the electron. Therefore the rate of energy loss of the electrons is given by,

$$\begin{aligned}
-\frac{dE_e}{dt} &= c\sigma_t\gamma^2 \left(1 + \frac{1}{3}\beta^2\right) U_{rad} - c\sigma_t U_{rad} \\
&= \frac{4}{3}c\sigma_t\gamma^2\beta^2 U_{rad},
\end{aligned} \tag{1.38}$$

where we used $\gamma^2 - 1 = \gamma^2\beta^2$. Thus the net power lost by electron, and thereby converted into increased radiation is,

$$\begin{aligned}
P_{compt} &= \frac{dE_{rad}}{dt} \\
&= \frac{4}{3}c\sigma_t\gamma^2\beta^2 U_{rad}.
\end{aligned} \tag{1.39}$$

When the energy transfer in the electron rest frame becomes significant then [37],

$$-\frac{dE_e}{dt} = \frac{4}{3}c\sigma_t\gamma^2\beta^2 U_{rad}\left[1 - \frac{63}{10}\frac{\gamma}{m_e c^2}\frac{<\epsilon^2>}{<\epsilon>}\right]. \tag{1.40}$$

For a power law distribution of electron energies, the total power is given by summing over the distribution of γ,

$$P_{tot} = \int P_{compt} N(\gamma) d\gamma. \tag{1.41}$$

If $N(\gamma) = C\gamma^{-p}$ between $\gamma_{min} \leq \gamma \leq \gamma_{max}$, then with $\beta \sim 1$, we obtain,

$$P_{tot} = \frac{4}{3}c\sigma_t U_{rad}\frac{C}{3-p}\left(\gamma_{max}^{3-p} - \gamma_{min}^{3-p}\right). \tag{1.42}$$

For a thermal distribution of non-relativistic electrons with electron density n_e, the total power is,

$$P_{tot} = \frac{4k_B T_e}{m_e c^2}c\sigma_t n_e U_{rad}, \tag{1.43}$$

where we have used $<\beta^2> = \frac{3k_B T}{m_e c^2}, \gamma \approx 1$ in Eq. (1.39).

Now we can calculate the average power gained by the photon field from the electron, as follows: the mean number of photons scattered per second is,

$$\begin{aligned} N_c &= c\sigma_t n_{rad} \\ &= \frac{c\sigma_t U_{rad}}{<\epsilon>}, \end{aligned} \tag{1.44}$$

where $<\epsilon>$ is the average energy of photon define by $<\epsilon> = \frac{U_{rad}}{n_{rad}}$. Hence the average energy gained by the photon in one collision is,

$$<\Delta\epsilon> = \frac{P_{compt}}{N_c}. \tag{1.45}$$

Substituting Eq. (1.44) in Eq. (1.45), and using Eq. (1.39), we have,

$$\left\langle\frac{\Delta\epsilon}{\epsilon}\right\rangle = \frac{4}{3}\gamma^2\left(\frac{v}{c}\right)^2. \tag{1.46}$$

When $v \ll c, \gamma \approx 1$ and for a thermal distribution of non-relativistic electrons, $m_e v^2 =$

$3k_BT_e$, the above equation can be written as,

$$\left\langle \frac{\Delta\epsilon}{\epsilon} \right\rangle_{NR} \approx \frac{4k_BT_e}{m_ec^2}. \tag{1.47}$$

However, this ignores electrons recoil (we assumed elastic scattering in the electron rest frame). So we can incorporate the effect of recoil by simply subtracting the mean energy loss by photon given by $\approx -\frac{<\epsilon>}{m_ec^2}$, which comes from our earlier result. Combining this with Eq. (1.47), we have have a simple equation for energy gain or loss for photons as [38, 39],

$$\left\langle \frac{\Delta\epsilon}{\epsilon} \right\rangle_{NR} \approx \left(\frac{4k_BT_e}{m_ec^2} - \frac{<\epsilon>}{m_ec^2} \right). \tag{1.48}$$

If $4k_BT_e > <\epsilon>$, the net transfer of energy is from electrons to photons (inverse Compton scattering), otherwise net transfer is from photons to electrons.

In ultra-relativistic limit $\beta = \frac{v}{c} \to 1$, ignoring the energy transfer in the electron rest frame, Eq. (1.46) becomes,

$$\left\langle \frac{\Delta\epsilon}{\epsilon} \right\rangle_{R} \approx \frac{4}{3}\gamma^2. \tag{1.49}$$

Assuming the non-degenerate thermal distribution of ultra-relativistic electrons, we have [39],

$$\langle \gamma^2 \rangle = \frac{\langle E^2 \rangle}{(m_ec^2)^2} = 12 \left(\frac{k_BT}{m_ec^2} \right)^2, \tag{1.50}$$

then Eq. (1.49) becomes,

$$\left\langle \frac{\Delta\epsilon}{\epsilon} \right\rangle_{R} \approx 16 \left(\frac{k_BT}{m_ec^2} \right)^2. \tag{1.51}$$

The processes described above act as a major source of cooling for relativistic plasma as well as a mechanism for producing hight-energy photons. The time scale for a Compton cooling of an individual relativistic electron is given by,

$$t_{cool} \simeq \frac{\gamma m_ec^2}{P_{compt}}. \tag{1.52}$$

Substituting the value of P_{compt} and noting that $U_{rad} = \sigma T_{rad}^4$, where T_{rad} is a radiation temperature we have,

$$t_{cool} \simeq \frac{3m_ec^2}{4\sigma_t\gamma\sigma\beta^2 T^4{}_{rad}}. \tag{1.53}$$

If the electrons are non-relativistic (i.e. $\gamma \approx 1$) then,

$$t_{cool} \simeq \frac{k_B T_e}{P_{compt}}. \tag{1.54}$$

1.4   Multiple Scatterings (Compton y-parameter)

If multiple scatterings occur which is generally the case, the spectrum can be significantly affected. This is know as Comptonization. An important parameter is the Compton y-parameter defined as

$$y \equiv \left[\text{average fractional change in energy} \left(\frac{\Delta E}{E} \right) \text{ per scattering} \right]$$
$$\times \left[\text{mean number of scattering} \right], \tag{1.55}$$

which measures whether a photon will significantly change its energy when traversing a medium. When the electrons and photons co-exist in a region of size l, the repeated scatterings of the photons by the electrons will distort the original spectrum of the photons (i.e. Comptonization). We know that the mean free path of the photons due to Thomson scattering is $\lambda_\gamma = (n_e \sigma_t)^{-1}$. Thus if the size of the region l is such that $\frac{l}{\lambda_\gamma} \gg 1$, then the photon will undergo several collisions in this region. But if $\frac{l}{\lambda_\gamma} \ll 1$, then there will be few collisions. Therefore let us define optical depth $\tau_e \equiv \frac{l}{\lambda_\gamma} = n_e \sigma_t$ so that $\tau_e \gg 1$ implies strong scattering.

If $\tau_e \gg 1$, then the photon undergoes $N_s (\gg 1)$ collisions in traveling a distance l. From standard random-walk arguments we have [39],

$$N_s \approx \begin{cases} \tau_e^2 & \text{for } \tau_e \gg 1 \\ \tau_e & \text{for } \tau_e \ll 1 \end{cases}. \tag{1.56}$$

For most order-of-magnitude estimates it is sufficient to use $N_s \approx \tau_e^2 + \tau_e$ or $N_s \approx \max(\tau_e, \tau_e^2)$ [39] for any optical thickness.

Combining Eqs. (1.47), (1.51) and (1.55), we then obtain expressions for Compton

y-parameter for non-relativistic and relativistic thermal distribution of electrons:

$$\left.\begin{aligned} y_{NR} &= \frac{4k_B T}{m_e c^2}\mathrm{max}(\tau_e, \tau_e^2) \\ y_R &= 16\left(\frac{k_B T}{m_e c^2}\right)^2 \mathrm{max}(\tau_e, \tau_e^2) \end{aligned}\right\}, \tag{1.57}$$

where we have assumed that the energy transfer in the electron rest frame is small i.e. $4k_B T_e \gg \epsilon$. In literatures Compton y-parameter is defined as,

$$y = \frac{k_B T_e}{m_e c^2}\int \sigma_t n_e(r) dl, \tag{1.58}$$

where first part of the expression, $\frac{k_B T_e}{m_e c^2}$ represents the typical fractional energy change imparted to CMBR photon in one scattering, while the second part $\tau = \int \sigma_t n_e(r) dl$ is the optical depth to scattering.

Therefore, a fraction of the CMBR photons after decoupling ($z \approx 1100$) can be inverse Compton scattered by hot electrons in the intra-cluster medium as they traverse through the cluster. This can then lead to an apparent change in the temperature of the CMBR in the direction of the cluster defined in terms of Compton y-parameter and thus it is possible to detect galaxy clusters by observing small fluctuations in the CMBR. However a number of other astrophysical processes will also create S-Z distortions. These include S-Z distortion from peculiar velocities during reionization [40], supernova driven galactic winds [41] kinematic S-Z from Lyman break galaxy outflow [42], hot proto galactic gas [43] and supernovae from first generation of stars [44]. In this dissertation, we will mainly study the S-Z distortions from the galaxy clusters and discuss how it can act as strong cosmological probe.

Since only a small percent of the background photons passing through the cluster gets scattered, there is only a fractional change in the CMBR sky temperature due to the S-Z effect. It is easy to obtain an order of magnitude for such distortion in terms of Compton y-parameter. Let us assume that a cluster of galaxy has a total mass of $M = 5 \times 10^{14} \mathrm{M}_\odot$ and extends up to an virial radius $R_v = 2\mathrm{Mpc}$. As the intra-cluster medium (ICM) is assumed in hydrostatic equilibrium within the gravitational potential, it must obey the equation,

$$k_B T_e = \frac{GMm_p}{2R_v}, \tag{1.59}$$

where m_p is the mass of the proton and T_e is the electron temperature of the ionized

intra-cluster gas given by,

$$k_B T_e \approx 6.65 \text{KeV}. \tag{1.60}$$

This temperature of ICM is hot enough to ionize the gas and the ionized electrons of ICM inverse Compton scatter the CMBR photons. Since, the scatterings are essentially non-relativistic in nature (i.e. $k_B T_e \ll m_e c^2$), one can take the scattering cross-section to be Thompson cross section σ_t. The scattering optical depth, τ_e, for the cluster can then be written as,

$$\tau_e = n_e \sigma_t (2R_v) \approx 5.25 \times 10^{-3}. \tag{1.61}$$

In a single scattering, the frequency of the photon is slightly shifted, with up-scattering more probable than down scattering, because of the higher temperature of electrons relative to the photons. The mean fractional change in photon energy, due to the single scattering (to order of magnitude) is given by Eq. (1.45),

$$\left\langle \frac{\Delta \epsilon}{\epsilon} \right\rangle \approx \frac{k_B T_e}{m_e c^2} \approx 1.33 \times 10^{-2}, \tag{1.62}$$

where we have used Eq. (1.59), which in turn gives,

$$\frac{\Delta T_\gamma}{T_\gamma} \approx 1 \times 10^{-4}. \tag{1.63}$$

Combining Eqs. (1.61), (1.62) and using the fact that for small τ_e the number of scattering is equal to τ_e, one can get mean change in the CMBR sky temperature due to the S-Z effect from cluster to be $y \approx 7 \times 10^{-5}$ and this distortion is almost order of magnitude larger than that due to the primary anisotropies.

Similarly, an order of magnitude estimate ca be made for the kinematic S-Z effect. In this case all the photons get Doppler shifted by a factor $\frac{v}{c}$, where v is the line of sight component of the peculiar velocity of the cluster. Bulk peculiar velocities are expected to be less than 1000 km/s. One can then multiply the temperature change due to the bulk motion with the scattering optical depth, to get

$$\frac{\Delta T_\gamma}{T_\gamma} \approx \frac{v}{c} \times (5.25 \times 10^{-3}). \tag{1.64}$$

Typically, peculiar velocities are ~ 300km/s, which clearly implies, for cluster of galaxies thermal S-Z effect dominates over kinematic S-Z effect. In contrast to the general distribution of the CMBR, S-Z effect is localized, and seen only in the direction towards

galaxy clusters. In particular, since the effect, is linearly sensitive to electron temperature as well as to optical depth it becomes very concentrated towards dense and hot regions.

1.5   Structure of the Dissertation

The simplest cosmological use of the Sunyaev-Zel'dovich effect is to prove that CMBR is genuinely a cosmological phenomenon: the appearance of an effect from a cluster of galaxies at $z = 0.5455$ (CL $0016 + 16$) proves that the CMBR originates at $z > 0.54$, higher-redshift detections push this limit even further. However, it is a probe of cosmological parameters, and as a distance-independent probe of earlier phases of the universe that the S-Z effect has attracted most interest, and such uses of the effect are the focus of this study. The dissertation is organized as under:

In chapter 2, we will discuss S-Z effect in relation with large scale structure of universe. We will give a detailed analysis of both thermal and kinematic Sunyaev-Zel'dovich effect. We will also discuss non-thermal S-Z effect. In the last section we will discuss S-Z effect from quasars.

In chapter 3, we will see how S-Z effect, along with X-ray observations of clusters can help us in determining cluster morphology. We will discuss various uncertainties in determining parameters by this technique. At the end of chapter we will find the expression of S-Z effect in the presence of the cooling flow.

In chapter 4, we deal with S-Z cluster surveys and S-Z power spectrum and demonstrate the constraints in determination of the cosmological parameters. At the end of this chapter we will discuss evolution of gas mass fraction along with S-Z effect and the constraints on the cosmological models.

In chapter 5, we will give a summary of the work presented in this dissertation and suggest some future extensions of this work for my Ph. D.

Chapter 2

Sunyaev-Zel'dovich Effect with Large Scale Structure of Universe

2.1 Introduction

Recent developments in the theory and observation of the large-scale structure of the universe have made it a fruitful field of study. Most research centers on following the time evolution of matter densities and velocities in our universe, using both perturbation theory and non-linear approaches. In addition, the imprints of the large-scale structure and its evolution on the cosmic microwave background, in the form of the Sunyaev-Zeldovich effect are being explored. Because it is proportional to the gas pressure integrated along the line of sight, the thermal Sunyaev-Zel'dovich effect, provides a direct measure of large-scale structure and of cosmological parameters [5, 19]. The kinematic S-Z effect arising from Doppler effect by non-linear density fluctions associated with the virialized objects like galaxy clusters, quasars can be used to probe large scale velocity fields [6].

The Sunyaev-Zel'dovich effect thus provides a unique way to map the large scale structure of the universe as traced by massive clusters of galaxies. As a spectral distortion of the cosmic microwave background, the S-Z effect is insensitive to the redshift of the astrophysical objects, making it well-suited for studies of clusters at all redshifts, and especially at reasonably high redshifts, where the abundance of clusters is critically dependent on the underlying cosmology. Recent high signal-to-noise detections of the S-Z effect have enabled interesting constraints on cosmology density of the universe using small samples of galaxy clusters.

19

In this chapter we will discuss mathematical aspects of S-Z effect (both relativistic and non-relativistic) in relation to large scale structure of universe. and its importance in their detection and measurements.

2.2   Kompaneets Equation

Comptonization is the name given to the process by which electron scattering brings a photon to equilibrium. Because photons have a negligible cross-section for scattering by other photons (although for photons with frequencies ν_1 and ν_2 satisfying $h^2\nu_1\nu_2 \geq m_e^2 c^4$ photon-photon pair production and subsequent annihilation have the effect of photon-photon scattering), they can only come to equilibrium by interaction with matter. In the laboratory, the walls of an enclosure are available to absorb and re-emit the radiation, but in the astrophysical problems there are no walls and the absorptive processes in the matter are often low. In hot fully ionized matter, therefore, most frequent and important process is scattering. The finite electron mass leads to an electron recoil as a result of the scattering, and tends, on an average, to transfer energy from photons to electrons. The random electron velocities produce random Doppler shifts of the scatterers in the laboratory frame, which on an average, tend to increase the photon energy at the expense of the electron energy. The former effect increases with photon frequency, and the later with electron energy; if the photons have a thermal equilibrium distribution at the same temperature as that of the electrons, the two effects will balance. The term Comptonization is used if the electrons are in thermal equilibrium at temperature T_e, and if both $k_B T_e$ and $h\nu$ are much less than $m_e c^2$. In this non-relativistic limit, a number of powerful approximations are possible, and a differential equation of Fokker-Plank form of time evolution of the photon occupation number $n(\nu)$, assumed isotropic, is obtained. This equation was first published by Kompaneets, and is generally referred to as the Kompaneets equation [45]. The fully relativistic case is computationally much more complex and cannot be reduced to a Fokker-Planck equation.

Comptonization is likely to be important when the temperature is high and density is low, so that matter is fully ionized, and absorption process (generally proportional to the square of density) are less important than scattering (proportional to density). This is typically the situation in ICM (and accretion flows around compact objects, ionized bubbles around high redshift quasars). The low energy photons available there can be transferred to high energy protons and this is what is seen in the Thermal S-Z effect for

clusters of galaxies and predicted for other astrophysical sources of hot plasma.

We start with Boltzmann equation assuming an isotropic distribution of photons. Let $n(\nu)$ be the phase space density of photons and $f_e(E)$ be the phase space density of the electrons. We will also assume non-relativistic electrons followed by a Maxwellian distribution at a temperature T_e. If $f_e(E)$ and $f_e(E')$ are the distribution functions of electrons before and after scattering and $n(\nu)$ and $n(\nu')$ are the distribution functions of photon before and after the scattering then the Boltzmann equation is given as [46, 39]

$$\frac{\partial n(\nu)}{\partial t} = c \int d^3P \int \frac{d\sigma}{d\Omega} d\Omega \big[f_e(E')n(\nu')\big(1 + n(\nu)\big) - f_e(E)n(\nu)\big(1 + n(\nu')\big) \big], \quad (2.1)$$

where c is the velocity of light and $\frac{d\sigma}{d\Omega}$ is the scattering cross-section. The first term in the square bracket represents the scattering of photons from frequency ν to frequency ν' by the electrons. The factors $\big(1 + n(\nu)\big)$ and $\big(1 + n(\nu')\big)$ are due to the bosonic character of photons, and the corresponding fermionic factors $\big(1 - f_e(E)\big)$ and $\big(1 - f_e(E')\big)$ are ignored, since the electrons are assumed to be non-degenerate ($f_e \ll 1$). The second term similarly represents scattering from frequency ν' to frequency ν .

We consider the scattering,

$$E + \nu \rightleftharpoons E' + \nu'. \qquad (2.2)$$

In Eq. (2.1), $\frac{d\sigma}{d\Omega}$ is the electron-photon scattering cross-section (Thomson scattering) and the integration over d^3p takes into account all the electrons with energy $E = \frac{p^2}{2m_e}$. A detailed analysis of the evolution of the spectrum in the presence of the repeated scattering off relativistic electrons is difficult because the energy transfer per scattering is large and one must solve the integro-differential equation i.e. Eq. (2.1). However, when the electrons are non-relativistic, the fractional energy change ($h\Delta\nu$) per scattering is small. In particular Eq. (2.1) may be expanded to second order in this small quantity $\Delta\nu$ yielding an approximation called the Fokker-Planks equation. This equation was developed by Kompaneets and is called Kompaneets equation [45]. For a thermal distribution of non-relativistic electrons, $f_e(E)$ is given by,

$$f_e(E) \propto \exp\left(-\frac{E}{k_B T_e}\right). \qquad (2.3)$$

Considering situation in which $\Delta\nu \ll 1$ and expand $n(\nu') = n(\nu + \Delta\nu)$ and $f_e(E') =$

$f_e(E - h\Delta\nu)$ in a Taylor series in $\Delta\nu$, we get,

$$\left.\begin{aligned}
n(\nu') &= n(\nu) + \Delta\nu\frac{\partial n}{\partial\nu} + \frac{1}{2}(\Delta\nu)^2\frac{\partial^2 n}{\partial\nu^2} + \cdots \\
f_e(E') &= f_e(E) - h\Delta\nu\frac{\partial f_e}{\partial E} + \frac{1}{2}h^2(\Delta\nu)^2\frac{\partial^2 f_e}{\partial E^2} + \cdots
\end{aligned}\right\}. \tag{2.4}$$

Put $x = \frac{h\nu}{k_B T_e}$ and using Eq. (2.3) in above equation, we get,

$$\left.\begin{aligned}
n(\nu') &= n(\nu) + h\frac{\Delta\nu}{k_B T_e}\frac{\partial n}{\partial x} + \frac{1}{2}h^2\left(\frac{\Delta\nu}{k_B T_e}\right)^2\frac{\partial^2\nu}{\partial x^2} + \cdots \\
f_e(E') &= f_e(E) + h\frac{\Delta\nu}{k_B T_e}f_e(E) + \frac{1}{2}h^2\left(\frac{\Delta\nu}{k_B T_e}\right)^2 f_e(E) + \cdots
\end{aligned}\right\}. \tag{2.5}$$

substituting Eq. (2.5) in Eq. (2.1) we have,

$$\begin{aligned}
\frac{\partial n}{\partial t} &= \frac{h}{k_B T_e}\left[\frac{\partial n}{\partial x} + n(n+1)\right]I_1 + \\
&\quad \frac{1}{2}\left(\frac{h}{k_B T_e}\right)^2\left[\frac{\partial^2 n}{\partial x^2} + 2(1+n)\frac{\partial n}{\partial x} + n(n+1)\right]I_2,
\end{aligned} \tag{2.6}$$

where,

$$\left.\begin{aligned}
I_1 &= \int d^3p\int d\Omega\frac{d\sigma}{d\Omega}cf_e(E)\Delta\nu \\
I_2 &= \int d^3p\int d\Omega\frac{d\sigma}{d\Omega}cf_e(E)(\Delta\nu)^2
\end{aligned}\right\}. \tag{2.7}$$

Thus the integro-differential equation Eq. (2.1) has been reduced to a differential equation, the effect of scattering being factored out in the integrals.

To proceed further, we need to estimate $\Delta\nu$ in the individual scattering. The conservation of energy and momentum in the electron-proton scattering can be expressed respectively as

$$\left.\begin{aligned}
h\nu + \frac{p^2}{2m_e} &= h\nu' + \frac{p'^2}{2m_e} \\
\frac{h\nu}{c}\vec{n} + \vec{p} &= \frac{h\nu'}{c}\vec{n}' + \vec{p}'
\end{aligned}\right\}, \tag{2.8}$$

where $\vec{n}, \vec{n}'$ are the directions of incident and scattered photons respectively. Rearranging Eq. (2.8) we get,

$$h\Delta\nu = -\frac{h\nu c\vec{p}.(\vec{n} - \vec{n}') + h^2\nu^2(1 - \vec{n}.\vec{n}')}{m_e c^2 + h\nu(1 - \vec{n}.\vec{n}') - c\vec{p}.\vec{n}'}. \tag{2.9}$$

Considering the leading terms only, one gets,

$$h\Delta\nu = -\frac{h\nu\vec{p}.(\vec{n} - \vec{n}')}{m_e c}. \tag{2.10}$$

This can be understood as follows: In Eq. (2.9) if we take $h\nu \sim k_B T_e \sim O(m_e v^2)$, then in the numerator, the second term is an $O(\frac{v}{c})$ correction to the first term. In the denominator, the second term is an $O(\frac{v^2}{c^2})$ correction to the first term and the third term in the denominator is also an $O(\frac{v}{c})$ correction to first term. Hence, to lowest order, the Eq. (2.9) reduces to Eq. (2.10). Substituting for $\Delta\nu$ from the Eq. (2.10) into second part of Eq. (2.7), we have,

$$I_2 = \left(\frac{\nu}{m_e c}\right)^2 c \int d^3 p \int d\Omega \frac{d\sigma}{d\Omega} f_e(E)[\vec{p}.(\vec{n} - \vec{n}')]^2. \tag{2.11}$$

Let ψ be the angle between $\vec{p}$ and the vector $(\vec{n} - \vec{n}')$, so that the above equation can be written as,

$$I_2 = \left(\frac{\nu}{m_e c}\right)^2 c \int d^3 p \int d\Omega \frac{d\sigma}{d\Omega} f_e(E) p^2 |(\vec{n} - \vec{n}')|^2 \cos^2 \psi. \tag{2.12}$$

Since $dp^3 = p^2 dp d\Omega$ and factor $|(\vec{n} - \vec{n}')|$ does not depend on p therefore can be taken out of the integral over electron momentum space. We can therefore write,

$$
\begin{aligned}
I_2 &= \left(\frac{\nu}{m_e c}\right)^2 c \int d^3 p\, p^2 \cos^2 \psi f_e(E) \int d\Omega \frac{d\sigma}{d\Omega} |(\vec{n} - \vec{n}')|^2 \\
&= \left(\frac{\nu}{m_e c}\right)^2 c \int_0^\infty p^2 dp \int_{-1}^{+1} \cos^2 \psi \, d(\cos\psi) \int_0^{2\pi} d\phi\, p^2 f_e(E) \int d\Omega \frac{d\sigma}{d\Omega} |(\vec{n} - \vec{n}')|^2 \\
&= \frac{1}{3}\left(\frac{\nu}{m_e c}\right)^2 c \int_0^\infty 2p^2 dp \int_0^{2\pi} d\phi\, p^2 f_e(E) \int d\Omega \frac{d\sigma}{d\Omega} |(\vec{n} - \vec{n}')|^2 \\
&= \frac{1}{3}\left(\frac{\nu}{m_e c}\right)^2 c \left[\int_0^\infty 4\pi p^2 dp\, p^2 f_e(E)\right] \int d\Omega \frac{d\sigma}{d\Omega} |(\vec{n} - \vec{n}')|^2. \tag{2.13}
\end{aligned}
$$

The integral in square brackets in the above integral is simply $n_e \times <p^2>$, where n_e is the number density of the electrons or $2m_e$ times the electron kinetic energy density. Because $f_e(E)$ is Maxwellian this is $3k_B T_e m_e n_e$. Then,

$$I_2 = \left(\frac{\nu}{m_e c}\right)^2 c k_B T_e m_e n_e \int d\Omega \frac{d\sigma}{d\Omega} |(\vec{n} - \vec{n}')|^2. \tag{2.14}$$

In the non-relativistic limit, the differential cross-section is Thomson cross-section given by $\frac{d\sigma_t}{d\Omega} = \frac{1}{2}r_e^2 \left[1 + (\vec{n}.\vec{n}')^2\right]$, where $r_e = \frac{e^2}{m_e c^2}$ is the classical electron radius. Then Eq. (2.14) transforms as,

$$
\begin{aligned}
I_2 &= \left(\frac{\nu}{m_e c}\right)^2 ck_B T_e m_e n_e \int d\Omega \frac{1}{2}r_e^2 \left[1 + (\vec{n}.\vec{n}')^2\right] |(\vec{n} - \vec{n}')|^2 \\
&= \left(\frac{\nu}{m_e c}\right)^2 ck_B T_e m_e n_e \frac{1}{2}r_e^2 \int_{-1}^{+1} \left(1 + \cos^2 \psi\right) 2(1 - \cos \psi) d(\cos \psi) \int_0^{2\pi} d\phi \\
&= \left(\frac{\nu}{m_e c}\right)^2 ck_B T_e m_e n_e 2\pi r_e^2 \left[\cos \psi - \frac{\cos^2 \psi}{2} + \frac{\cos^3 \psi}{3} - \frac{\cos^4 \psi}{4}\right]_{-1}^{+1} \\
&= \left(\frac{\nu}{m_e c}\right)^2 ck_B T_e m_e n_e r_e^2 \frac{16\pi}{3} \\
&= 2\left(\frac{\nu}{m_e c}\right)^2 ck_B T_e m_e n_e \sigma_t,
\end{aligned}
\tag{2.15}
$$

where $\sigma_t = \frac{8\pi}{3}r_e^2$ is the Thomson cross-section. Although I_1 can be calculated the same forward way like I_2, it is more difficult than I_2. A faster and more elegant way is to use photon number conservation. Since the number of photons should not change with time, so the integral of photon density over the phase space should remain constant in time. Also since x is proportional to momentum, then the change in number of photons per unit volume, which much vanish is proportional to,

$$
\frac{d}{dt}\int nx^2 dx = \int \frac{\partial}{\partial t}x^2 dx = 0.
\tag{2.16}
$$

Since the phase space photon density within any volume can only change by photons leaving or entering the volume, it must be proportional to a flux j. This flux should be chosen, such that,

$$
\frac{\partial n}{\partial t} = -\frac{1}{x^2}\frac{\partial}{\partial x}[x^2 j(x)].
\tag{2.17}
$$

Above equation simply implies that the change in total flux arises only from flux through the boundaries as,

$$
\frac{d}{dt}\int nx^2 dx = -\int_0^\infty \frac{1}{x^2}\frac{\partial}{\partial x}[x^2 j(x)] = -x^2 j(x)|_0^\infty.
\tag{2.18}
$$

It is obvious, that j can only depend on n', n and x. Now Eq. (2.6) contains a term equal to $\frac{\partial^2 n}{\partial x^2}$ times a function of x but not n. Because Eq. (2.17) describes the same function

it must have the same form, so that the term in j proportional to $\frac{\partial n}{\partial x}$ cannot contain any other dependence on n. Hence j must be of the form,

$$j(n, x) = g(x) \left[\frac{\partial n}{\partial x} + h(n, x) \right],$$ (2.19)

where g and h are functions yet to be determined. The photons follow the Bose-Einstein distribution given by,

$$n = \frac{1}{e^{x+\alpha} - 1},$$ (2.20)

where α is a chemical potential. So that,

$$\frac{\partial n}{\partial x} = -n(n+1).$$ (2.21)

Now $\frac{\partial n}{\partial t} = 0$ requires that current density $j(x) = 0$. Thus one gets from Eq. (2.19)

$$\frac{\partial n}{\partial x} = -h(x, n)$$
$$h(x, n) = n(n+1).$$ (2.22)

Using Eq. (2.17) and Eq. (2.19), we have,

$$\frac{\partial n}{\partial t} = -\left(g'n' + gn'' + gh' + hg' + 2\frac{g}{x}n' + 2\frac{hg}{x} \right),$$ (2.23)

where the primes are derivatives with respect to x. $g(x)$ can be determined if we compare the coefficients of $\frac{\partial^2 n}{\partial x^2}$ in Eq. (2.23) and Eq. (2.6), and then substituting the value of I_2 from Eq. (2.15).

$$g(x) = -\frac{cx^2 n_e \sigma_t k_B T_e}{m_e c^2}.$$ (2.24)

Using Eq. (2.22) and Eq. (2.24) we get full form of $j(x)$ as,

$$j(x) = -\frac{cx^2 n_e \sigma_t k_B T_e}{m_e c^2} [n' + n(n+1)].$$ (2.25)

Using $j(x)$ of above form in Eq. (2.17), one finally arrives at the Kompaneets equation,

$$\frac{\partial n}{\partial t} = \frac{c n_e \sigma_t k_B T_e}{m_e c^2} \frac{1}{x^2} \frac{\partial}{\partial x} \left[x^4 \left(\frac{\partial n}{\partial x} + n + n^2 \right) \right] \tag{2.26}$$

$$\frac{\partial n}{\partial t_c} = \left(\frac{k_B T_e}{m_e c^2} \right) \frac{1}{x^2} \frac{\partial}{\partial x} \left[x^4 \left(\frac{\partial n}{\partial x} + n + n^2 \right) \right], \tag{2.27}$$

where the quantity $t_c = (n_e \sigma_t c)$ is the time measured in units of mean time between scattering, since scattering time scale $t_s = \frac{1}{n_e \sigma_t c}$.

By defining $\eta = \frac{h\nu}{k_B T_\gamma} = x\frac{T_e}{T_\gamma}$, where T_γ is the CMBR temperature, then Eq. (2.26) can be rewritten (substituting $x = \frac{T_\gamma}{T_e}\eta$) [10]

$$\frac{\partial n}{\partial t} = \frac{c n_e \sigma_t k_B T_e}{m_e c^2} \left(\frac{T_e}{T_\gamma} \right)^2 \frac{1}{\eta^2} \frac{T_e}{T_\gamma} \frac{\partial}{\partial \eta} \left[\left(\frac{T_\gamma}{T_e}\eta \right)^4 \left(\frac{T_e}{T_\gamma} \frac{\partial n}{\partial \eta} + n + n^2 \right) \right]. \tag{2.28}$$

If the temperature of the electrons is large compared to the temperature of radiation, which is the case of cluster gas (keV electrons) with reference to CMBR (meV photons) then the first term in above equation dominates, and the Kompaneets equation takes the following form [47],

$$\begin{aligned}
\frac{\partial n}{\partial t} &= \frac{c n_e \sigma_t k_B T_e}{m_e c^2} \frac{1}{\eta^2} \frac{\partial}{\partial \eta} \left[\eta^4 \left(\frac{\partial n}{\partial \eta} \right) \right] \\
&= \frac{c n_e \sigma_t k_B T_e}{m_e c^2} \frac{1}{\eta^2} \left[4\eta^3 \frac{\partial n}{\partial \eta} + \eta^4 \frac{\partial^2 n}{\partial \eta^2} \right] \\
&= \eta \frac{c n_e \sigma_t k_B T_e}{m_e c^2} \left[\eta \frac{\partial^2 n}{\partial \eta^2} + 4 \frac{\partial n}{\partial \eta} \right].
\end{aligned} \tag{2.29}$$

This approximation could also have been achieved, if the bosonic corrections in the Boltzmann equation would have been ignored in the beginning. But at that point, it was more general to keep these corrections, although the photon gas of the CMBR is of course not degenerate.

The general theoretical aspects of Sunyaev-Zel'dovich will be investigated in the proceeding sections for scattering of photons from a plasma cloud using the Kompaneets equation of the form Eq. (2.26).
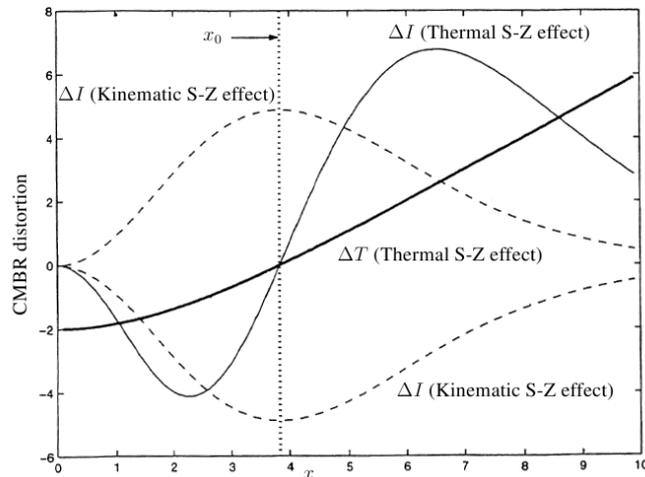
Figure 2.1: Frequency dependence of Thermal S-Z effect and Kinematic S-Z effect. Thick line shows the frequency dependence of $\frac{\Delta T_\gamma}{T_\gamma}$ for Thermal S-Z effect, whereas the thin solid line shows the same for the change in spectral intensity ΔI. The thin dashed lines show the change in spectral intensity for Kinematic S-Z effect, The upper one for approaching source of distortion and lower for a receding one. The vertical dotted line shows the scaled frequency at which the Thermal S-Z effect is zero and Kinematic S-Z effect is maximum. In the above plot y I_0 and T_γ are scaled to unity [50].

2.3 Thermal Sunyaev-Zel'dovich Effect

As defined earlier, Sunyaev-Zel'dovich (S-Z) effect is a scattering of CMBR from energetic electrons in a gravitationally bound plasma in a cluster of galaxies [5, 9, 48, 49, 50, 51]. Low energy CMBR photons travel from the surface of last scattering and are boosted in energy by the few keV thermal electrons via Thomson scattering. The probability of scattering depends on the electron density of cluster and is of the order of 1% for any given photon. This is the thermal S-Z effect and it results in unique spectral distortion to the CMBR intensity spectrum as shown in Fig. (2.1). The CMBR thus acts as a back-light to the cluster, which appears as a cold patch at frequencies below $\sim 218\mathrm{GHz}$ and a hot patch above $\sim 218\mathrm{GHz}$. We begin by considering a cloud of Maxwellian electrons with $T_e \gg T_\gamma$ $(h\nu \ll k_B T_e)$. The rate of change of photon occupation number of the isotropic radiation field due to scattering by isotropic, non-relativistic Maxwellian electrons is given by Kompaneets equation Eq. (2.26). Using expression for Compton

y-parameter, Eq. (1.58), Kompaneets equation then takes the form,

$$\frac{\partial n}{\partial y} = \frac{1}{x^2}\frac{\partial}{\partial x}\left[x^4\left(\frac{\partial n}{\partial x} + n + n^2\right)\right] \tag{2.30}$$

Since $(h\nu \ll k_B T_e)$ and hence $x \ll 1$, then we have $\frac{\partial n}{\partial x} \gg n$ and n^2. Hence ignoring small terms above equation takes the form,

$$\frac{\partial n}{\partial y} = \frac{1}{x^2}\frac{\partial}{\partial x}\left(x^4\frac{\partial n}{\partial x}\right). \tag{2.31}$$

The homogeneity of the right hand side of the above equation allows us to substitute $x = \frac{h\nu}{k_B T_e}$ by $x = \frac{h\nu}{k_B T_\gamma}$. If the radiation is weakly scattered, the the approximate solution to above equation can be obtained by substituting on the right hand side the expression for occupation number of a purely Planckian radiation field, given by $n(x) = \frac{1}{e^x-1}$. Therefore, above equation takes the form,

$$\begin{aligned}\frac{\partial n}{\partial y} &= \frac{1}{x^2}\frac{\partial}{\partial x}\left[x^4\frac{\partial}{\partial x}\left(\frac{1}{e^x-1}\right)\right] \\ &= \frac{xe^x}{(e^x-1)^2}\left[\frac{x(e^x+1)}{e^x-1} - 4\right]. \end{aligned} \tag{2.32}$$

Now integrating along the path length through the cluster, we have,

$$\begin{aligned}\Delta n &= \frac{xe^x}{(e^x-1)^2}\left[\frac{x(e^x+1)}{e^x-1} - 4\right]y \\ \Rightarrow \frac{\Delta n}{n} &= \frac{xe^x}{(e^x-1)}\left[\frac{x(e^x+1)}{e^x-1} - 4\right]y. \end{aligned} \tag{2.33}$$

Since the change in radiation spectrum $\Delta I(x)$ at frequency x is given by $\Delta I(x) = x^3 \Delta n(x) I_0$, where $I_0 = \frac{2h}{c^2}\left(\frac{k_B T_\gamma}{h}\right)^3$, we have

$$\left.\begin{aligned}\Delta I(x) &= I_0 \frac{x^4 e^x}{(e^x-1)^2}\left[\frac{x(e^x+1)}{e^x-1} - 4\right]y \\ \frac{\Delta I(x)}{I(x)} &= \frac{\Delta n}{n}\end{aligned}\right\}. \tag{2.34}$$

From first part of Eq. (2.34), we have,

$$\Delta I(x) = I_0 G(x) y, \tag{2.35}$$
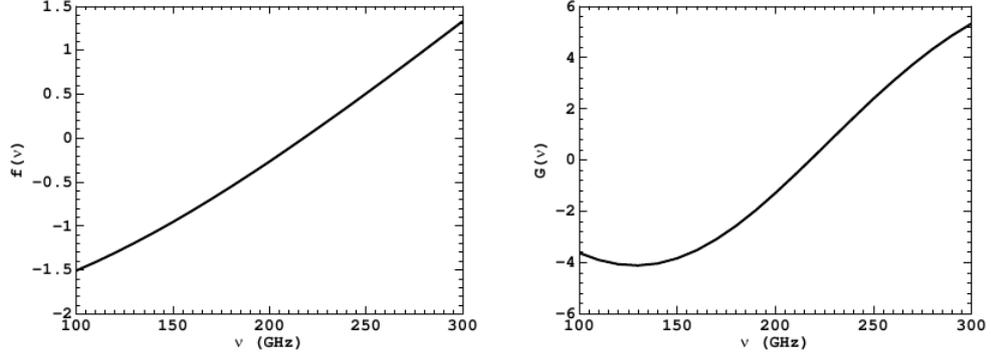
Figure 2.2: Frequency variation of the two functions $f(\nu)$ and $G(\nu)$, where $\nu = \frac{k_B T_\gamma x}{h}$.

where $G(x)$ is given by,

$$G(x) = \frac{x^4 e^x}{(e^x - 1)^2} \left[\frac{x(e^x + 1)}{e^x - 1} - 4 \right]. \tag{2.36}$$

Now we have the following transformation between intensity and temperature,

$$\Delta I(x) = \frac{2h\nu^3}{c^2} \frac{e^x}{(e^x - 1)^2} \frac{h\nu}{k_B T_\gamma^2} \Delta T. \tag{2.37}$$

Using Eq. (2.35), (2.36) and (2.37), we get,

$$\Delta T_\gamma = T_\gamma y f(x), \tag{2.38}$$

where $f(x)$ is given by relation,

$$f(x) = \left[\frac{x(e^x + 1)}{e^x - 1} - 4 \right]. \tag{2.39}$$

In Fig. (2.2), the functional dependence of $g(x)$ and $f(x)$ on frequency are shown for fixed value of CMBR temperature. At frequency ~ 218GHz the functions become zero. This frequency is defined as the null point frequency of the S-Z effect. In the Rayleigh-Jeans limit we have $x \to 0$, so that we get from Eq. (2.38),

$$\frac{\Delta T_\gamma}{T_\gamma} = -2y. \tag{2.40}$$

Thus we see that there would be an apparent decrease in the sky brightness in the CMBR sky towards objects like galaxy clusters which are capable of scattering the microwave background photons. This is sometimes referred to in the literature as hole in the sky [16]. In Wien region, it can be shown that the distortion goes as $x^2 y$. In most cases of interest in astrophysics, the approximation $x^2 y < 1$ is a valid assumption and we can use Eq. (2.38). However, when the condition $x^2 y < 1$ is not satisfied, then one may make use of a change in variables from $(x, y) \rightarrow (\xi, y)$ given by $\xi = 3y + \ln x$, so that Eq. (2.31) becomes [8, 7],

$$
\begin{aligned}
\frac{\partial n}{\partial y} &= \left(\frac{1}{e^{\xi - 3y}}\right)^2 \frac{\partial}{\partial \xi}\left[\left(e^{\xi - 3y}\right)^4 \frac{\partial n}{\partial \xi}\frac{\partial \xi}{\partial x}\right]\frac{\partial \xi}{\partial x} \\
&= \frac{\partial^2 n}{\partial \xi^2}.
\end{aligned}
\tag{2.41}
$$

The solution to such an equation is of the form of

$$
I(x) = \int_{\infty}^{\infty} P_k(s) I_0 \, ds.
\tag{2.42}
$$

In the above equation, the energy shift due to scattering is denoted by $e^s = \frac{\nu'}{\nu}$ and the Kompaneets scattering kernel is given by [52],

$$
P_k(s) = \frac{1}{\sqrt{4\pi y}}\exp\left[-\frac{(s + 3y)^2}{4y}\right].
\tag{2.43}
$$

With this we come to the end of non-relativistic treatment of the thermal S-Z effect. Before going over to the next section, we briefly discuss a few features of Eq. (2.38) . The usefulness of the form of the temperature distortion given in Eq. (2.38) is due to its simple analytic form. However, it must be emphasized that this is valid in the case of small optical depth of the scattering medium. As it stands from Eq. (2.38) we see that $f(x)$ gives the frequency dependence of the distortion and is characterized by three distinct frequencies: $x_0 = 3.83$, where thermal S-Z effect vanishes; $x_{min} = 2.26$ which gives minimum decrement of the microwave background intensity and $x_{max} = 6.51$ which gives maximum distortion due to this effect. In fig. (2.1) the cross over frequency is shown with a vertical dotted line. It is clearly seen from the thick line that at R-J limit ($\frac{\Delta T}{T} = -2y$) at frequency below the cross over frequency there is a dip in the temperature and the intensity for thermal Sunyaev-Zel'dovich effect.

At first approximation, none of these spectral features depend on the temperature of the scattering medium. However, for a very hot gas, one can no longer do a non-relativistic treatment and the final result would depend on the temperature of the gas. The relativistic treatment of the thermal S-Z effect will be discussed in the next section. Also here Compton y parameter depends only on the product $T_e \tau_e$ of the gas. This is essentially the integral of the gas pressure along the line of sight. For relativistic treatment, the expression for the amplitude would be proportional to τ_e for small τ_e and would depend on T_e in a complicated manner.

2.4 Relativistic Thermal S-Z Effect

The calculations of Sunyaev and Zel'dovich are based on a solution to the Kompaneets equation, a non-relativistic diffusion approximation to the fully kinetic equation for the change of photon distribution due to scattering. In fact, at high frequencies these expressions are insufficiently accurate for some of their intended uses. An accurate calculation of the thermal effect is particularly essential in determining the Hubble constant and peculiar velocity of clusters. The inaccuracy of the Kompaneets-based treatment is due to two reasons: First, because of the low optical thickness to Compton scattering in clusters, most photons are not scattered even once. A diffusion approximation would then hardly seem adequate. The second and more important reason is that with inter-cluster gas temperature spanning the range $3 - 15$keV, electron velocities in the inter-cluster gas are near relativistic. Consequently, the mean relative frequency change in the scattering, which is assumed to be small enough for its use as an expansion parameter in the derivation of the Kompaneets equation, is not sufficiently small. Even so, the Kompaneets based treatment of S-Z effect yields an adequate description of the spectral change at low frequencies on the R-J side. A more accurate description of the spectral change due to scattering requires calculation of the exact frequency redistribution, using full expression for the scattering probability and the correct relativistic form for the electron velocity distribution.

The inadequacy of the Kompaneets based treatment has been recognized early on, largely in the connection with the Comptonization at early epochs when the temperature might have been very high. An accurate relativistic treatment of the scattering process for any value of τ_e was given by Wright [52, 53, 54, 55]. Their treatment relax the assumption of the low optical depth for the scattering medium. Further they do not make the assumption $k_B T_e \ll m_e c^2$. This is a more exact treatment of the relativistic nature of the thermal
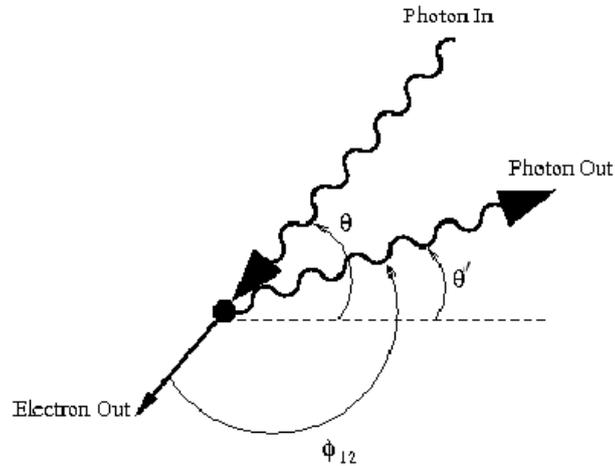
Figure 2.3: The geometry of scattering in the rest frame of the electron before the interaction. An incoming photon, at angle θ relative to the x_e axis, is deflected by angle ϕ_{12}, and emerges after the scattering at angle θ' with almost unchanged energy (Eq. 1.19). In the observer's frame, where the electron is moving with velocity βc along the x_e axis, the photon changes energy by an amount depending on β and the angles θ and θ' (Eq. 2.46).

S-Z Effect which would be applicable if the plasma is very hot ($T_e \geq 10\text{keV}$). Ignoring the Compton shift in the scattering $h\nu \ll m_e c^2$, and taking the electrons to have relativistic Maxwellian distribution, greatly simplifies the physics involved, though more careful calculations require relaxing this assumption [52]. So while these are generally called inverse Compton scattering, they could more accurately be called Thomson scattering.

If the geometry is similar to Fig. (2.3), then in the electron frame of reference (with transformation $\theta \to \pi - \theta$ and $\theta' \to \theta'$), the photon frequency is,

$$\widetilde{\nu} = \frac{\nu}{\gamma(1 - \beta\mu)}, \tag{2.44}$$

where $\mu = \cos\theta$, θ is the angle between photon direction and electron velocity in the electron rest frame. The probability of collision with an angel θ is given by [56]

$$p(\mu)d\mu = \left[2\gamma^4(1 - \beta\mu)^3\right]^{-1} d\mu. \tag{2.45}$$

The output frequency is

$$\nu' = \nu \left(\frac{1 + \beta\mu'}{1 - \beta\mu} \right), \tag{2.46}$$

where $\mu' = \cos\theta'$, θ' the outgoing photon angle with respect to electron velocity in the electron rest frame. The probability of scattering to angle θ' is,

$$\phi(\mu', \mu)d\mu' = \frac{3}{8} \left[1 + \mu^2\mu'^2 + \frac{1}{2}(1 - \mu^2)(1 - \mu'^2) \right] d\mu'. \tag{2.47}$$

Typically, the scattering is expressed in terms of the logarithmic frequency shift,

$$s = \ln\left(\frac{\nu'}{\nu}\right) = \ln\left(\frac{1 + \beta\mu'}{1 - \beta\mu}\right) \tag{2.48}$$

$$\Rightarrow d\mu' = \frac{1}{\beta}(1 - \beta\mu)e^s ds$$

$$d\mu' = \frac{1}{\beta}(1 + \beta\mu'). \tag{2.49}$$

Then the probability that a single scattering of the photon by an electron with speed βc causes shift s is given by,

$$
\begin{aligned}
P(s, \beta) &= \int p(\mu)d\mu\phi(\mu', \mu)\left(\frac{d\mu'}{ds}\right)ds \\
&= \frac{3}{16\gamma^4\beta} \int \frac{(1 + \beta\mu')\left[1 + \mu^2\mu'^2 + \frac{1}{2}(1 - \mu^2)(1 - \mu'^2)\right]}{(1 - \beta\mu)^3}d\mu.
\end{aligned} \tag{2.50}
$$

This integration can be easily done and Fig. (2.4) shows the resulting function for several values of β. To calculate the photon frequency spectrum on scattering by a population of electrons, one has to average over the electron velocity distribution $p_\beta(\beta)d\beta$. One assumes the electron velocities to follow a relativistic Maxwellian distribution [57], then the overall distribution in frequency shift in a single scattering, $P_1(s)$ is given by,

$$
\begin{aligned}
P_1(s) &= \int_{\beta_m}^1 p_\beta(\beta)P(s, \beta)d\beta \\
&= \frac{\int_{\beta_m}^1 \beta^2\gamma^5 e^{-(\gamma-1)/x'} P(s, \beta)d\beta}{\int_{\beta_m}^1 \beta^2\gamma^5 e^{-(\gamma-1)/x'}}.
\end{aligned} \tag{2.51}
$$
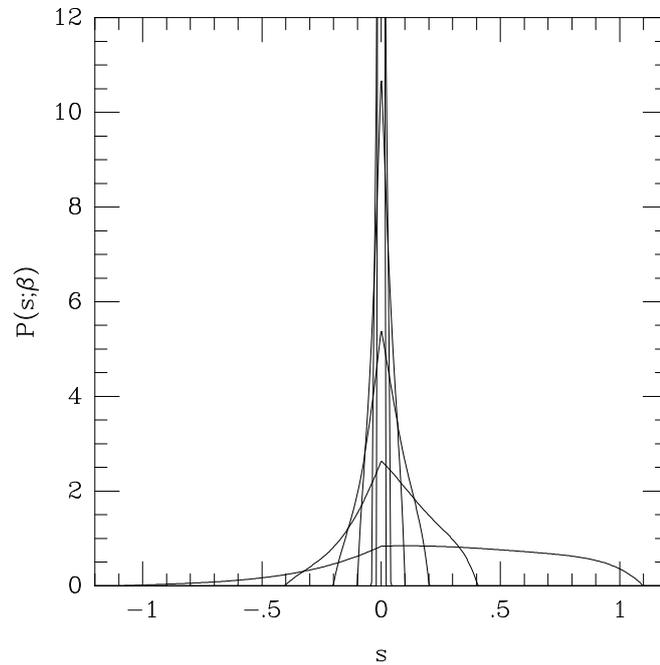
Figure 2.4: The function $P(s; \beta)$ for $\beta = 0.01, 0.02, 0.05, 0.10, 0.20,$ and 0.50. $P(s; \beta)$ becomes increasingly asymmetric and broader as β increases [8].

where

$$\beta_m = \frac{e^{|s|} - 1}{e^{|s|} + 1}, \tag{2.52}$$

is the minimum value of β capable of causing a frequency shift s and $x' = \frac{k_B T_e}{m_e c^2}$. Once $p_1(s)$ is known, it is possible to evaluate the probability that a frequency change s is produced by a n number of repeated scattering. This is given by repeated convolution

$$
\begin{aligned}
P_n(s) &= \int_{-\infty}^{+\infty} ds_1 \dots ds_{n-1} \dots P_1(s_1) \dots P(s_{n-1}) P_1(s - s_1 - \dots - s_{n-1}) \\
&= \underbrace{P_1(s) \otimes \dots \otimes P_1(s)}_{n\,times}.
\end{aligned}
\tag{2.53}
$$

The resulting total redistribution function $P(s)$ can be written as the sum of all the functions $P_n(s)$, each one weighted by the probability that a CMBR photon can suffer n scat-

tering, which is assumed to be Poissonian with the expectation value τ,

$$
\begin{aligned}
P(s) &= \sum_{n=0}^{+\infty} \frac{e^{-\tau_e} \tau_e^n}{n!} P_n(s) \\
&= e^{-\tau_e} \left[P_0(s) + \tau_e P_1(s) + \frac{1}{2} \tau_e^2 P_2(s) + ... \right] \\
&= e^{-\tau_e} \left[\delta(s) + \tau_e P_1(s) + \frac{1}{2} \tau_e^2 P_1(s) \otimes P_1(s) + ... \right].
\end{aligned}
\tag{2.54}
$$

The multiple scattering of the radiation changes its incident Plank intensity $I_0(s)$ to $I(s)$ which is obtained by convolving $I_0(s)$ with $P(s)$ as,

$$
I(s) = e^{-\tau_e} \left[I_0 + \tau_e I_0 \otimes P_1(s) + \frac{1}{2} \tau_e^2 I_0 \otimes P_1(s) \otimes P_1(s) + ... \right].
\tag{2.55}
$$

In Fourier space, the convolution takes a very easy form, since

$$
F[f \otimes g] = F[f].F[g].
$$

Then the exact calculation of Eq. (2.55) becomes simpler by going to the Fourier space $I(k)$ of $I(s)$ and we get,

$$
\begin{aligned}
I(k) &= e^{-\tau_e} I_0(k) \left[1 + \tau_e P_1(k) + \frac{1}{2} \tau_e^2 P_1(k)^2 + ... \right] \\
&= I_0(k) e^{\tau_e(P(k)-1)},
\end{aligned}
\tag{2.56}
$$

where

$$
P_1(k) = \int_{-\infty}^{+\infty} P_1(s) e^{-iks} ds,
\tag{2.57}
$$

and

$$
P_1(s) = \frac{1}{2\pi} \int_{-\infty}^{+\infty} P_1(k) e^{iks} dk.
\tag{2.58}
$$

Eq. (2.56) allows us to calculate the intensity change for any value of the temperature and optical depth of the scattering medium. However, for most cases of applications in astronomy, it deals with regions of the small optical depth τ_e which rarely assumes values higher than 0.01 and then one can approximate $P(s)$ by

$$
P(s) \simeq (1 - \tau_e) \delta(s) + \tau_e P_1(s).
\tag{2.59}
$$

To obtain the final expression for the intensity change at each value of the scattering photon frequency, $P(s)$ has to be convolved with the incident Planckian frequency distribution. Integrating the product $I_0(s)P(s)$ over s and transforming back to the non-dimensional frequency x, we have

$$\Delta I = I_0(x)\tau_e[\Phi(x,x') - 1]. \tag{2.60}$$

The relative temperature change is,

$$\frac{\Delta T}{T_0} = \frac{(e^x - 1)}{xe^x}\tau_e[\Phi(x,x') - 1]. \tag{2.61}$$

The function $\Phi(x,x')$ comes from the integration over μ, β, s. The limit on β has been given above and the angle integrals are between μ_1 and μ_2 given by

$$\left.\begin{array}{ll}
\mu_1 = \left\{\begin{array}{ll} -1 & s \leq 0 \\ \frac{1-e^{-s}(1+\beta)}{\beta} & s \geq 0 \end{array}\right. \\[3mm]
\mu_2 = \left\{\begin{array}{ll} -1 & s \leq 0 \\ \frac{1-e^{-s}(1-\beta)}{\beta} & s \geq 0 \end{array}\right.
\end{array}\right\}. \tag{2.62}$$

Using $w = \exp(-s)$, we obtain [10],

$$\Phi(x,x') = A(x')[\Phi_1(x,x') + \Phi_2(x,x')], \tag{2.63}$$

where

$$
\begin{aligned}
\Phi_1(x,x') &= \int_0^1 \frac{w(e^x - 1)dw}{e^{xw} - 1}\int_{\beta_m}^1 \gamma e^{-(\gamma-1)/x'}d\beta \int_{\mu_1}^1 q(w,\mu,\beta)d\mu \\
\Phi_2(x,x') &= \int_0^1 \frac{w(e^x - 1)dw}{w^3(e^{x/w} - 1)}\int_{\beta_m}^1 \gamma e^{-(\gamma-1)/x'}d\beta \int_{-1}^{\mu_2} q(w,\mu,\beta)d\mu \\
q(w,\mu,\beta) &= \frac{\frac{1}{\beta^2}(3\mu^2 - 1)\left(\frac{1-\beta\mu}{w} - 1\right)^2 + (3 - \mu^2)}{(1 - \beta\mu)^2} \\
A(x') &= \frac{3}{32\int_0^1 \beta^2\gamma^5 e^{-(\gamma-1)/x'}d\beta}.
\end{aligned} \tag{2.64}
$$

These equations summarize the calculation of the relativistically correct Comptonization spectrum of the CMBR in the limit of small τ_e, but with the use of the exact angular probability distribution in the scattering. Because the incident radiation field is isotropic and

the electrons are mildly relativistic, it may be assumed that the scattering is isotropic in the electron rest frame. Under this assumption, the scattering probability can be averaged over the direction of the incident photon. Doing so considerably simplifies the expression for $P(s, \beta)$ [39]

$$P_{iso}(s, \beta) = \frac{e^s}{(2\gamma\beta)^2} \begin{cases} (1 + \beta)e^s - 1 + \beta, & \frac{1-\beta}{1+\beta} \leq e^s \leq 1 \\ 1 + \beta - (1 - \beta)e^s, & 1 < e^s \leq \frac{1+\beta}{1-\beta} \end{cases}. \qquad (2.65)$$

In this approximation we then have

$$\Phi_{iso}(x, x') = B(x')\Phi(x, x'), \qquad (2.66)$$

where

$$\begin{aligned} \Phi(x, x') &= \int_0^1 (e^x - 1) \left[\frac{1}{e^{xw} - 1} + \frac{1}{w^3(e^{x/w} - 1)} \right] \zeta(x, x') dw \\ \zeta(x, x') &= \int_{\beta_m}^1 e^{-(\gamma-1)/x'} \left[(1 + \beta)w - 1 + \beta \right] d\beta. \\ B(x') &= \frac{8}{3} A(x'). \end{aligned} \qquad (2.67)$$

As expected, the dependence of the relativistically correct expression for the intensity change T_e is no longer linear; ΔI depends explicitly on x, τ_e, and x' whereas that of Eq. (2.35) depends only on x and $y = \tau_e x'$. Thus, in general both x' and τ_e have to be separately specified in the calculations of exact intensity change: At a given frequency the intensity change may assume different values for a given values of y. Moreover, due to the exponential nature of the Planckian spectrum, a slight shift in the scattering probability distribution to higher frequencies can cause distinguishable change between non-relativistic and relativistic results, near the cross-over frequency, where the intensity change vary steeply.

Raphaeli [10, 55] calculated ΔI for values of $k_B T_e$ in the interval $1 - 50$keV ($x' = 511.0 - 10.2$). To check the validity of the isotropic form for the scattering probability, the calculations was repeated with $P(s, \beta)$ replaced by $P_{iso}(s, \beta)$; although the results differ somewhat, the isotropic approximation is generally adequate. The results are compared with S-Z expression based on Kompaneets non-relativistic expression. The level of deviation starts becoming important from $k_B T_e > 5$keV. At this temperature, the relative intensity change ($\frac{\Delta I_R - \Delta_{NR}}{\Delta_{NR}}$) is greater 20% close to the cross-over frequency and
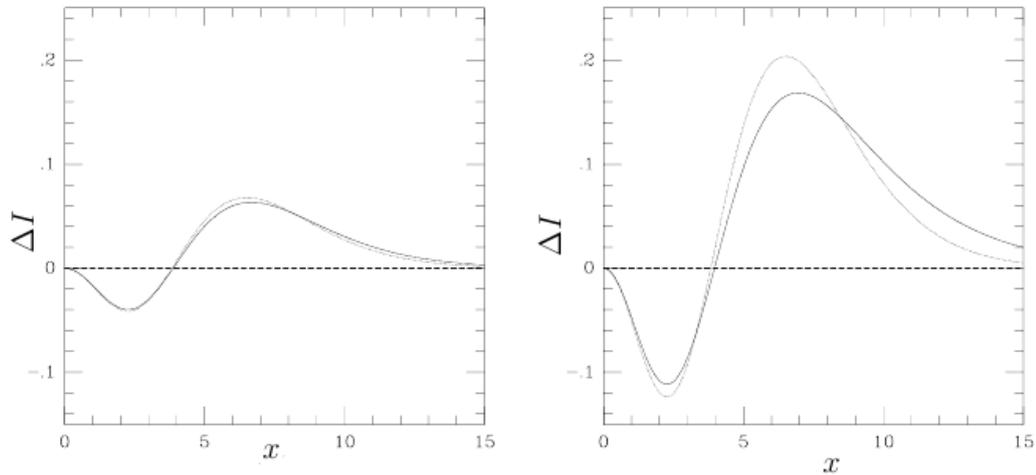
Figure 2.5: The spectral deformation caused by the S-Z effect in radiation in the units of I_0. The Kompaneets approximation is shown as a dotted line. The left is for electrons at $k_B T_e = 5.1$keV and the right is for electrons at $k_B T_e = 15.3$keV [8].

at $x \geq 11$. The deviations are higher and over a wider range in x for high temperatures and especially at higher frequencies. However, one must note that, we have neglected the higher order terms in τ_e, which means that the above results are only approximate. The main characteristic of the relativistic solution w.r.t non-relativistic case is the general decrease of the intensity change for values of $x \simeq 8 - 8.4$ for temperature range $k_B T_e = 1 - 15$keV and an increase at higher values of x. The higher the gas temperature, the higher is the Wien deviation deviation from that in Kompaneets case.

An important feature of the more accurate relativistic treatment is a shift in the value of the cross-over frequency to higher values with increasing T_e. In contrast, the non-relativistic value $x_0 = 3.85$ is temperature independent. Deviations from the latter value are simply linear in $\frac{k_B T_e}{mc^2}$ and indeed a good approximation, to within 0.2% in the interval $k_B T_e = 1 - 50$keV, is

$$x_0 \simeq 3.83 \left(1 + \frac{k_B T_e}{mc^2} \right). \tag{2.68}$$

An exact determination of x_0 necessitates the full calculation of the intensity change with the inclusion of higher-order terms in τ_e. A comparison of these two intensity functions, the full relativistic and the Kompaneets approximation is given in Fig. (2.5).

To conclude this section, let us point out once again that the degree of Comptoniza-

tion predicted by a solution of the Kompaneets equation is significantly different in the Wien side of the photon spectrum from a relativistic calculation taking into account near-relativistic electrons and low optical thickness. The difference between the two treatments is not significant for a gas temperature below 5keV. Also, in the relativistic case x_0 becomes temperature dependent in contrast to the constant value of $x_0 = 3.83$ predicted in the last section. A precise knowledge of this value becomes important if one needs to decouple the kinetic Sunyaev-Zel'dovich effect from thermal Sunyaev-Zel'dovich effect.

2.5   Non-Thermal S-Z Effect

Just as scattering from thermal electrons gives an S-Z effect, so does scattering from non-thermal electrons [58]. The spectrum of the scattered radiation in this case will differ from that shown in Fig. (2.5) and will depend on the shape of the electron spectrum. The calculations becomes quite involved, as the full relativistic treatment is necessary. Here, only qualitative properties will be discussed. Energetic non-thermal (NT) electrons whose pressure is not negligible compared to the thermal gas pressure constitute an aspect of inverse Compton (IC) phenomena with possibly appreciable ramifications for precision S-Z measurements. The presence of significant energetic electron populations in many clusters has been known from measurements of diffuse IC radio emission and recently also from NT X-ray emission in a few clusters. NT electrons produce an additional degree of Comptonization that amounts to a small intensity change (ΔI_{NT}) that must be accounted for, particularly in the measurement of H_0 from the thermal component, and peculiar cluster velocities from the kinematic component of the S-Z effect. Relativistic generalizations of the original non-relativistic calculations to a sufficiently high level of accuracy, provides the theoretical basis for calculation also ΔI_{NT}.

For the cluster possessing radio halos, a large amount of relativistic electrons should also affect the S-Z effect. This non-thermal S-Z effect has been investigated recently [59]. Fig. (2.6) shows the S-Z effect spectrum of A2163 obtained from a thermal population and from the combination of thermal and non-thermal populations. The thermal population in A2163 has a temperature of $k_B T_e = 12.4 \pm 0.5$keV and a central density of $n_{e,TH} = 6.862 \times 10^3$ cm^3 and a non-thermal population with $n_{e,NT} = 5 \times 10^{-5}$cm^3 for a pressure ratio $\frac{P_{NT}}{P_{TH}} = 0.29$. It is found [58] that the non-thermal effect is negligible when compared with the thermal S-Z effect and the main impact of this effect is a shift of the cross-over frequency, the null of the thermal S-Z effect, to higher values. The S-Z effect is also a
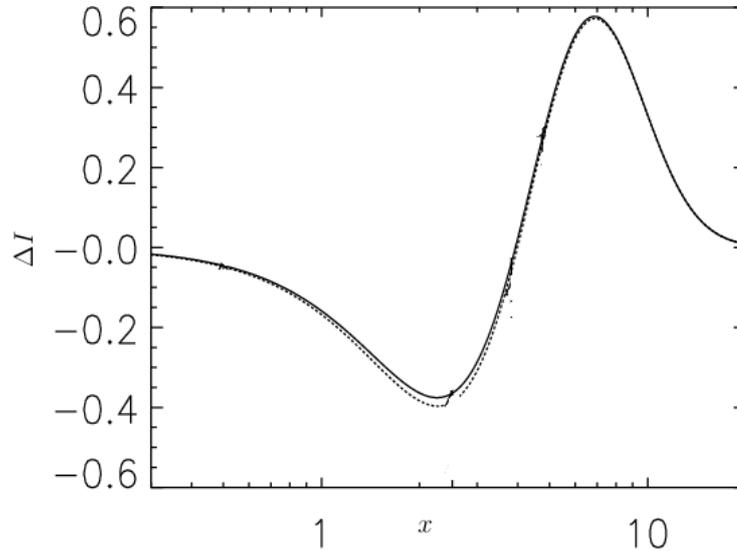
Figure 2.6: Theoretical expectations for the spectrum of the S-Z effect in A2163. We show the fit to the available data yielded by a thermal population (solid curve) and the expectations obtained from a combination of thermal and non-thermal populations with $n_{e,NT} = 5 \times 10^{-5} \text{cm}^3$ for a value of the pressure ratio $P_{NT}/P_{\text{TH}} = 0.29$ (dashed curve) [58].

potentially powerful tool for clarifying the original mechanism of the HXR (hard X-rays) excess. An interpretation of the HXR is non-thermal bremsstrahlung from supra-thermal electrons [60], the electron population has a modified Maxwellian distribution with a high-energy non-thermal tail.

Unfortunately, it is not easy to detect the S-Z from non-thermal electron populations as there is a great deal of synchrotron radio emission. At low frequencies the synchrotron emission will easily dominate over the non-thermal S-Z. At high radio frequencies, however, there is more chance that the S-Z effect could be detected, but there are still difficulties separating the S-Z from the flatter section of the synchrotron radiation. A further difficulty is that radio emitters are expected to be strongly in-homogeneous, so single dish measurements average over a variety of different radio source structures. This implies that the data taken might actually be produced by small variations in the electron energy distribution function. To get accurate results observations must be made with angular resolution comparable with the small-scale structures, which will prove difficult.

2.6   S-Z Effect with Superclusters

Missing mass is being sought in both non-baryonic and baryonic forms. Superclusters of galaxies, the largest known luminous structures in the universe, should hold correspondingly large masses of dark matter. Their study may lead us to the structure [61] and perhaps the constituents of dark matter [62], and their mass and kinematics probe [63, 64]. Most models of structure formation predict that superclusters contain residual intra-supercluster (ISC) matter in the form of diffuse, hot gas at the present epoch. This ISC gas could be either primordial [65], processed by an early generation of stars and subsequently ejected in winds from early massive star formation or active galactic nuclei [66, 67, 68] or stripped from merging clusters and proto-clusters. The expected temperature of the ISC gas is about $10^7 - 10^8$K [68, 69] and will remain hot, since the cooling time for gas at the expected low density $(< 10^{-3}$cm$^{-3})$ is longer than the Hubble time [70]. A measurement of the mass and extent of supercluster gas would be a useful indication of the processes involved in structure formation.

Most work on supercluster gas has been conducted through X-ray searches. Persic et al. [71, 72] searched for X-ray emission from superclusters in the HEAO-1 A2 data, finding no evidence for emission from the gas. Day et al. [73] searched for intra-supercluster gas in the Shapley supercluster using GINGA scans, and were able to set strong limits on the X-ray emission. More recently, Bardelli et al. [74] have used ROSAT PSPC data to claim that there is some diffuse X-ray emission in the Shapley supercluster between two of its component clusters.

The thermal Sunyaev-Zel'dovich effect provides another potential probe for intra-supercluster gas. Since this effect is proportional to the line of sight integral of n_e, it should be a more sensitive probe than the X-ray emission for studying the diffuse gas expected in superclusters. The angular scales of the well-known superclusters are large (degrees), so that the COBE DMR database is the best source of information on their Sunyaev-Zel'dovich effects: ground-based work is always on too small an angular scale, and the balloon searches do not cover such a large fraction of the sky at present.

Limits to the average Sunyaev-Zel'dovich effects from clusters of galaxies (and their associated superclusters) were derived by Banday et al. [75] through a cross-correlation analysis of the COBE DMR 4-year data with catalogues of clusters of galaxies. The result, that the average Sunyaev-Zel'dovich effect is less than 8μK (95 per cent confidence limit at 7 angular scale), suggests that these Sunyaev-Zel'dovich effects are not strong.
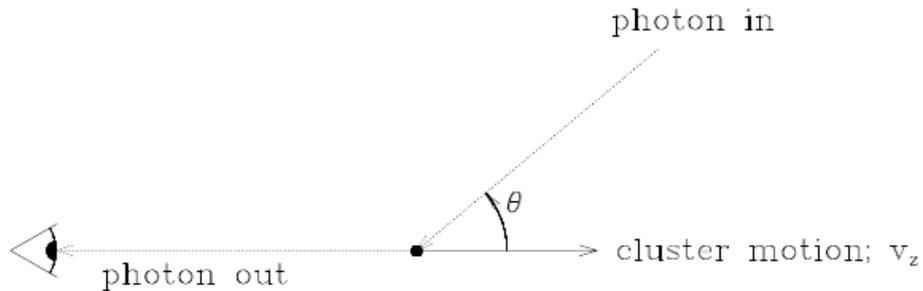
Figure 2.7: The geometry for the discussion of the kinematic Sunyaev-Zel'dovich effect, as seen in the frame of an observer at rest in the Hubble flow.

However, although population studies of this type show that average superclusters do not contain atmospheres with significant gas pressures, the COBE DMR database can also be searched for indications of a non-cosmological signal towards particular superclusters of galaxies.

2.7 Kinematic Sunyaev-Zel'dovich Effect

The kinematic S-Z effect is caused by the movement of the galaxy cluster responsible for thermal S-Z effect relative to Hubble flow. Thus, in the reference frame of the scattering gas the cosmic microwave background will appear anisotropic which inverse Compton scattering will cause to become isotropic again. In doing so, it causes the radiation field at the observer to become less isotropic, and thus there is a distortion towards the scatterer with amplitude proportional to $\frac{\tau_e v_z}{c}$, where v_z is the peculiar velocity of the scattering bulk [6, 76, 77, 78, 79, 80]. The kinematic S-Z Effect is found to have different spectral nature than thermal S-Z effect and hence the two can be separated. The kinematic S-Z effect is also shown in Fig. (2.1) and one can see that the optimum frequency band to observe the kinetic effect is near the thermal null at ~ 218GHz, thus reducing contamination from thermal signal. In addition to thermal contamination, the kinematic effect has an unfortunate feature of the intensity spectrum identical to the CMBR. This means that CMBR fluctuations cannot be distinguished from kinematic S-Z effect. To derive the

expression for CMBR temperature distortion due to the kinematic S-Z effect on can either start with the Boltzmann equation [81, 82] or use the radiative transfer equation [8]. As in the thermal Sunyaev-Zel'dovich effect, we will start with Boltzmann equation Eq. (2.1) in order to investigate the collision effect. Again, the correction terms for the Bose and Fermi statistics can be neglected. From Eq. (2.1), we have for Kinematic S-Z effect,

$$\dot{n}(\theta, \nu) = \int dp' \int \frac{d\sigma}{d\Omega} d\Omega \left[n(\theta', \nu') - n(\theta, \nu) \right] f_e(p'), \tag{2.69}$$

using the assumption that the energy transfer is small and hence $\nu' \sim \nu$, so that there is no recoil and $f_e(p) \approx f_e(p')$.

In the simple case of an electron gas moving with constant velocity, the electron density can be expressed as being proportional to a Dirac delta distribution $f_e(p) = n_e \delta(p_e - p)$ which implies,

$$\dot{n}(\theta, \nu) = n_e \int \frac{d\sigma}{d\Omega} d\Omega \left[n(\theta', \nu') - n(\theta, \nu) \right] f_e(p'). \tag{2.70}$$

Using the differential Thomson cross section and an ideal Planck distribution for the photon density, one obtains,

$$\dot{n}(\theta, x) = 2\pi n_e \int_{-1}^{+1} \frac{3\sigma_t}{16\pi} \left(1 + \cos^2 \theta' \right) d\cos\theta' \left[\frac{1}{e^{x'} - 1} - \frac{1}{e^x - 1} \right], \tag{2.71}$$

with $x = \frac{h\nu}{k_B T_\gamma}$. Dividing $n(\theta, x)$ and integrating along the line of sight yields,

$$\frac{\Delta n(\theta, x)}{n} = \frac{3}{8} \int dl \sigma_t n_e \int_{-1}^{+1} \left(1 + \cos^2 \theta' \right) d\cos\theta' \left[\frac{e^x - 1}{e^{x'} - 1} - 1 \right]. \tag{2.72}$$

Using relativistic transformation into the rest frame of the electron and the corresponding back transformation. Assuming that the change in frequency by Compton scattering is negligible, the frequency changes because of the change in direction of the photon is,

$$\nu' = \nu \gamma^2 (1 + \beta_z)(1 - \beta_z \cos\theta'), \tag{2.73}$$

where we have used the relativistic transformation from CMBR rest frame to electron rest frame as,

$$\widetilde{\nu} = \nu \gamma (1 + \beta_z). \tag{2.74}$$

Hence,

$$
\begin{aligned}
x' &= x\gamma^2(1+\beta_z)(1-\beta_z\cos\theta') \quad &(2.75)\\
&\approx x(1+\beta_z)(1-\beta_z\cos\theta'). \quad &(2.76)
\end{aligned}
$$

A Taylor expansion of $n(\theta,\omega')$ in v_z up to second order gives,

$$
\frac{1}{e^{x'}-1} = \frac{1}{e^x-1} - (1-\cos\theta')\frac{x\beta_z e^x}{(e^x-1)^2} + O(v_z^2), \quad (2.77)
$$

where v_z is the velocity of cluster in the line of sight. Eq. (2.77) can be inserted in Eq. (2.72) giving,

$$
\begin{aligned}
\frac{\Delta n(\theta,x)}{n} &\approx \frac{3}{8}\int dl\sigma_t n_e \int_{-1}^{+1}\left(1+\cos^2\theta'\right)d\cos\theta'\\
&\quad \left[(e^x-1)\left(\frac{1}{e^x-1}-(1-\cos\theta')\frac{x\beta_z e^x}{(e^x-1)^2}\right)-1\right]\\
&= -\frac{3}{8}\int dl\sigma_t n_e \int_{-1}^{+1}\left(1+\cos^2\theta'\right)d\cos\theta'(1-\cos\theta')\frac{x\beta_z e^x}{e^x-1}. \quad (2.78)
\end{aligned}
$$

Because $\cos\theta'$ is an odd and $1+\cos^2\theta'$ an even function, the part proportional to $\cos\theta'$ can be dropped, since its integral is 0. The integration for the remaining term can be carried out very easily and results in,

$$
\begin{aligned}
\frac{\Delta n(\theta,x)}{n} &= \frac{\Delta I(\theta,x)}{I}\\
&\approx -\frac{x\beta_z e^x}{(e^x-1)}\int dl\sigma_t n_e\\
&= -\frac{x\beta_z e^x}{(e^x-1)}\tau_e \quad &(2.79)\\
\Rightarrow \Delta I &\approx -I_0\beta_z\tau_e\frac{x^4 e^x}{(e^x-1)^2}. \quad &(2.80)
\end{aligned}
$$

The fractional change in temperature is given by,

$$
\frac{\Delta T}{T_\gamma} \approx -\frac{v_z}{c}\tau_e. \quad (2.81)
$$

This spectral form corresponds to a simple decrease in the radiation temperature as stated by Sunyaev & Zel'dovich [83].

It would be very difficult to locate the kinematic S-Z effect in the presence of the thermal S-Z effect at low frequency. The ratio of the brightness temperature caused by the effect is,

$$
\begin{aligned}
\frac{\Delta T_{kinematic}}{\Delta T_{thermal}} &= \frac{1}{2}\left(\frac{v_z}{m_e c^2}\right)^{-1} \\
&= 0.085\left(\frac{v_z}{1000\text{ km}^{-1}}\right)\left(\frac{k_B T_e}{10\text{ keV}}\right)^{-1},
\end{aligned} \tag{2.82}
$$

which is small for the expected velocities of a few hundred kms^{-1} or less, and the typical cluster temperatures of a few keV. However, the thermal and kinematic effects can be separated using different spectra: indeed, in the Kompaneets approximation it is easy to show that the kinematic effect produces its maximum intensity change at the frequency at which thermal effect is zero.

Thus observations near $x = 3.83$ (218GHz) are sensitive mostly to the kinematic effect, but in interpreting such observations it is necessary to take careful account of the temperature dependence of the shape of the thermal Sunyaev-Zel'dovich effect's spectrum, and of the frequency of the null of the thermal effect. The first strong limits on the peculiar velocities of clusters of galaxies derived using this technique are now becoming available as will be discussed in next section.

Clusters of galaxies produce further microwave background anisotropies through the same space-time effect, if they are expanding or contracting [84, 85]. A contaminating Sunyaev-Zel'dovich effect must also appear at the same time if an expanding or collapsing cluster contains associated gas because of the anisotropy of inverse-Compton scattering, but the sizes of these effects are too small to be detectable in the near future.

An interesting extension of this work would be to use the kinematic S-Z effect from a radio source to measure the speed of the radio-emitting plasma. Just as for a cluster of galaxies, the presence of a scattering medium which is moving relative to the CMBR will produce a kinematic Sunyaev-Zel'dovich effect which is proportional to $\tau_e(\frac{v_z}{c})$, but whereas v_z should be small for a cluster relative to the Hubble flow, the velocity of the radio-emitting plasma in a radio galaxy may be a substantial fraction of the speed of light, and a large kinematic Sunyaev-Zel'dovich effect will be seen if the optical depth of the radio-emitting plasma is sufficient, but the CMBR distortion will be complex and Eq. (2.81) will be no longer valid.

2.8   Cluster Peculiar Velocities

The kinematic S-Z effect, which is directly proportional to the radial peculiar velocity, provides an alternative way to measure the radial peculiar velocity field. The kinematic S-Z effect signal is independent of the redshift, so radial peculiar velocity derived from the measurement of the kinematic S-Z effect has a redshift-independent measurement error, unlike the distance measurements in the traditional redshift-based radial peculiar velocity surveys. However, kinematic S-Z effect is a small signal (typically a few μK) and spectrally indistinguishable from the primary CMBR anisotropy (around 100μK), which makes this measurement a challenging observational effect. The thermal S-Z component, which is 10 times bigger than the kinematic S-Z effect, also acts as a dominant source of error for kinematic S-Z effect detection. However, the thermal S-Z signal becomes zero at around 218GHz, which makes it possible to separate the thermal and the kinetic components. This makes the kinematic S-Z effect a unique and powerful cosmological tool. The peculiar velocity can directly be derived from the kinematic S-Z effect after separating it from the thermal S-Z effect. Only a few attempts to measure the kinematic S-Z effect have been made, because of contamination by the CMBR.

The first interesting attempts were made by Holzapfel et al. [86]. They observed Abell2163 ($z = 0.02$) and Abell1689 ($z = 0.183$) with SuZIE at 140GHz, 218GHz and 270GHz, which includes and brackets the null in the thermal S-Z effect. They found peculiar velocities of $v_z = +490^{+1370}_{-880}$kms^{-1} for Abell2163 and $v_z = +170^{+815}_{-630}$kms^{-1} for Abell1689. The uncertainties are at 68% confidence and include both statistical as systematic errors. A reanalization of all the available data for Abell2163, including new measurements by the OVRO and BIMA S-Z effect imaging systems at 30 GHz agrees perfectly with the values from Holzapfel et al. [87]. It is remarkable how striking the agreement between measurements using different techniques and instruments is. Benson et al. [88] were the first to set constraints on the bulk flow of the intermediate redshift ($z > 0.2$) universe towards the cosmic dipole. They did this by using a sample of six clusters and found a velocity limit of ≤ 1420kms^{-1} at a confidence level of 95%.

Transverse velocities of galaxy clusters will produce polarized signal in the scattered CMBR. This polarization will be perpendicular to the cluster velocity and the line of sight. Although, in frequency integrated light, the level of polarization might be difficult to detect with the techniques presently available, the polarization has a strong frequency dependence, increasing towards higher frequencies. For values of transverse velocity

of 1000kms^{-1}, and an optical depth of 0.02, the degree of polarization at 857GHz is around 2.10^{-6}. Since the polarization depends on the square of the transverse velocity, and linearly on the optical depth, certain clusters should show higher polarization. Other sources of polarization, in particular dust and synchrotron radiation, will contaminate the signal. However filtering techniques that take into account the characteristic frequency dependence of this polarization should allow one to extract the signal due to the kinematic effect. Measured polarization could then be used to infer transverse velocities of clusters. This question will be elaborated in future work.

Although the kinetic S-Z effect is hard to use because of its weakness in signal and the contamination by primary CMBR fluctuations, this last result shows that it may be possible to determine mean peculiar velocities on extremely large scales by averaging over clusters.

2.9   Quasars and Kinematic S-Z effect

The intergalactic medium near a quasar must be strongly ionized by the quasar's radiation. These hot gas bubbles are likely to be over-pressured, and to expand into their surrounding intergalactic medium. Thus both thermal and kinematic Sunyaev-Zel'dovich effects may arise near quasars, and we might expect a contribution from quasars in the spectrum of fluctuations in the CMBR [89]. It is found that the kinematic effect dominates, and can cause local changes of $\approx 300\mu K$ in the brightness temperature of the CMBR on scales up to ≈ 1 deg. Whether such structures are indeed present in the CMBR will be tested by the next generation of CMBR surveys.

Sunyaev-Zel'dovich effects may also be seen from the Lyman α absorption clouds seen in quasar spectra [90]. The expected effects are much smaller, typically only a few μK and with angular sizes of less than an arc-minute, from the varying numbers of Lyα systems on different lines of sight. Here again the dominant contribution to the signal is from the kinematic Sunyaev-Zel'dovich effect, and relies on large velocities acquired by the Lyα absorbing clouds as large-scale structure forms.

Either of these effects, or possibly a Sunyaev-Zel'dovich effect from a quasar-related cluster with a deficiency of bright galaxies, or a kinematic effect from colliding QSO winds [91], might explain the observations of CMBR anisotropies towards the quasars PHL 957 [92] and PC 1643+4631 [93]. However, the reality of these detections remains

in some dispute until they are independently confirmed.

2.10   Observational Techniques

In order to determine the feasibility of observing a particular cluster, some assessment of the expected S-Z signal is required. The richest clusters of galaxies typically have $y_{e0} \approx 10^4$ (Compton y parameter through cluster center). So for exploration of the thermal S-Z effect, sensitivity in $\frac{\Delta T}{T}$ units of around 10^5 is useful. In terms of brightness temperature, in the Rayleigh-Jeans region, a sensitivity $y_{e0} \approx 10^{-5}$ corresponds to,

$$\Delta T_{RJ} = 2y_{e0}T = 55\mu K. \tag{2.83}$$

The brightness temperature signal is smaller at higher frequencies, although work in the secondary peak at about 350GHz (see Fig. (2.5)) may be feasible. In practice, the sensitivities in Eq. (2.83) is barely adequate for observing the thermal S-Z effect. Extra sensitivity is always useful in the light of systematic problems with data, and also for probing quantities such as the cluster luminosity function. To detect the kinematic effect a factor of ten further improvement in sensitivity is required. Since spectral techniques must be used to separate the thermal and kinematic effects, this sensitivity must be available in several bands that cover a wide frequency range.

1) **Radiometers**

The first method used to detect the S-Z effect makes use of existing radio telescopes on which large periods of observing time are available. These telescopes tend to have beam-sizes of a few arcminutes at microwave frequencies, which is about the angular size of moderately distant clusters of galaxies. While relatively little customization is needed for this, making it relatively inexpensive, but to make accurate measurements long observation times are needed. For example, to make a measurement with an accuracy of 10μK (brightness temperature) would take in excess of five hours. Many reliable S-Z measurements have been obtained using single-dish systems, with random measurement errors $< 100\mu$K, and only low-level residual systematic errors (for example from radio source confusion).

The main problem encountered is emission from the Earth's atmosphere, which varies with both space and time. To account for this telescopes will tend to use difference

measurements by quickly switching from one location on the sky to another. Another problem encountered is the difficulty relating the measured signal from the radiometer to the brightness temperature of the S-Z effect. That is, there is a problem of calibration. Generally, the absolute calibration of the telescope will be tied to the observation of planets, which can lead to a source of error.

2) **Bolometers**

Bolometric systems are quite similar to the radiometer measurements described in the previous section, with greatly increased sensitivity. Furthermore, bolometric measurements are of interest as they are sensitive outside the Rayleigh-Jeans part of the spectrum, thus providing the possibility of separating the thermal and kinematic S-Z effects. Bolometers themselves are simply small absorbers connected to a heat sink through a thin insulating link. When incident radiation strikes the absorber it raises its temperature, which is then measured to extract the initial power. As each absorber is often on the order of millimeters, an array is needed to obtain useful data.

However, a problem with this technique is the high sky brightness over which the observations must be made. This implies that telescopes on high, dry sites or balloon experiments are necessary for efficient observation. Also, as in radiometric work, there is the problem of calibrating the data into absolute temperature. Again, the calibration is typically made through reference to the brightness of planets, which limits the accuracy of intensity measurements to about 6 per cent.

3) **Interferometers**

The two previous techniques are best suited for large-scale surveys searching for or examining galaxy clusters for only moderate angular resolutions. Radio interferometry, on the other hand, is a powerful method for making images of S-Z effects. These images can mostly be used in comparison with X-ray emission images. Also radio interferometry operates differently from the previous two, thus it suffers from other systematic difficulties and can provide an independent view.

Since radio interferometers are typically designed to maximize the angular resolution there is some maximum angular scale of structure that can be imaged by interferometers. The S-Z effect for clusters of galaxies has angular scales of several arcminutes, which will not be visible using an interferometer. As such a radio interferometer has difficulty detecting the S-Z effect, so a smaller interferometer is needed.

2.11   Summary

In this chapter, we presented the mathematical aspects of the Sunyaev-Zel'dovich effect and its cosmological significance in probing large scale structure of universe. We discussed the Comptonization of the CMBR by hot electrons and derived the amplitude and spectral dependence for both thermal and kinematic Sunyaev-Zel'dovich effect. We started with Boltzmann equation and developed expression of Kompaneets equation for non-relativistic case. It was found that, for Rayleigh-Jeans limit, the thermal S-Z expression is equal to $-2y$ and thus there would be decrease in brightness temperature of the CMBR sky towards any object containing hot gases like galaxy clusters, quasars etc. It was interesting to see that for non-relativistic case the spectral features of thermal S-Z effect did not dependent on the scattering medium and that too was the case in cross-over frequency where thermal S-Z effect vanishes. We then formulated relativistic expression of thermal S-Z effect which becomes necessary if the plasma is very hot ($T_e \geq 10$K). However with the relativistic treatment of the thermal S-Z effect it was found that the final result would depend on the temperature of the IC gas. Cross-over frequency was also found to have a weak dependence on electron temperature in contrast to constant value 3.83 predicted for non-relativistic case. The difference between non-relativistic and relativistic case is found to be insignificant for temperature below 5keV. We also discussed the non-thermal S-Z effect which becomes important while considering radio halos and radio-galaxies. The additional degree of Comptonization do to these non-thermal electrons is negligibly small when compared with thermal S-Z effect. Finally we ended discussion on thermal S-Z effect by considering it as possible probe of superclusters which in turn can give us information on the formation of large scale structure of the universe. Expression for kinematic S-Z effect was also obtained using Boltzmann equation, but this effect turned out to be very small and can be accurately determined at cross-over frequency where additional distortion due to thermal S-Z effect is absent. It was described as to how accurate measurement of it can probe the large scale velocity fields in the distant universe. For quasars kinematic S-Z effect dominates over thermal S-Z effect and can lead to possible probe for it. At the end of this chapter, we discussed methods of detection of S-Z effect, and their virtues and deficiencies.

Chapter 3

Cluster Cosmology with Sunyaev-Zel'dovich Effect and X-ray Observations

3.1 Introduction

Galaxy clusters can be studied in order to probe the growth and dynamics of universe. We study galaxy clusters by analyzing the electromagnetic radiation that they emit. S-Z effect and X-ray emission are the two mechanisms mostly used for studying galaxy clusters. The S-Z effect, which is a spectral distortion of the Cosmic Microwave Background radiation, is proportional to the integrated pressure along the line of sight, $\Delta T \propto \int n_e T_e dl$. The hot gas of the ICM, which make up most of the baryonic mass of the cluster, also emit radiation strongly in the X-ray range of the spectrum by the way of thermal bremsstrahlung. The X-ray surface brightness scales as $S \propto \int n_e^2 \Lambda_{eH} dl$, where Λ_{eH} is a cooling function. Fig. (3.1) illustrates the S-Z effect and X-ray bremsstrahlung emission from clusters. Taking the advantage of the different density dependences and with some assumptions about the geometry of the cluster the distance to the cluster may be determined [94, 95, 96, 97, 98, 99]. Using a sample of clusters at different redshifts, one can determine the curve for angular diameter distance as a function of redshift and from this curve determine the expansion rate of universe, H_0, known as Hubble constant.

These procedures assume cluster gas to be spherical, unclumped and isothermal. Almost all cluster, however, show departures from this simplistic model with some or
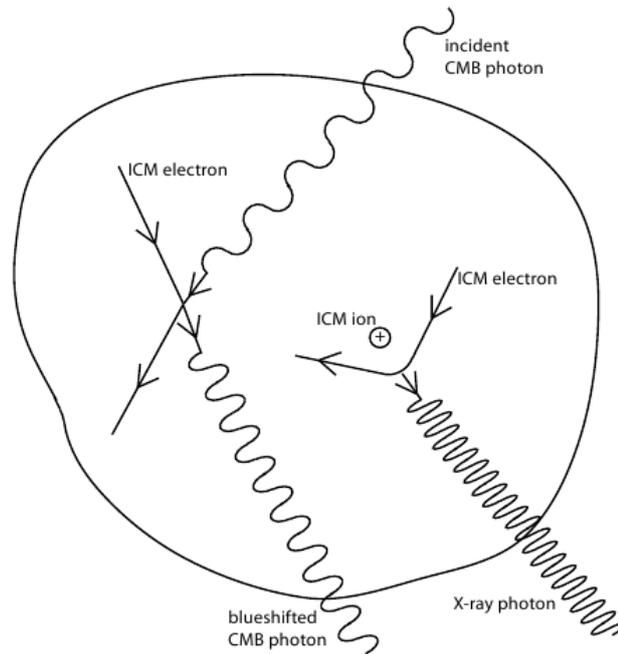
Figure 3.1: The Sunyaev-Zel'dovich effect is proportional to the internal pressure of the ICM integrated along the line of sight through the cluster, $\int n_e T_e dl$, where n_e is the electron number density and T_e is the electron gas temperature. X-ray bremsstrahlung emission from galaxy clusters is caused by the acceleration of free electrons by ions in the ICM. This effect is proportional to $\int n_e^2 \Lambda_{eH} dl$ where Λ_{eH} is the cluster's X-ray cooling function. Source-http://physics.princeton.edu/act/papers/sfrazierJP.pdf.

large extent. Departure from this model may lead to systematic errors in the determination of different cosmological parameters. In large, unbiased sample of clusters with random orientations, the statistical uncertainty should cancel to large degree. In this chapter, we will first discuss cluster morphology with X-rays. We then describe the method of measurement of angular diameter distances to galaxy clusters. This method employs measurements of S-Z effect and X-ray emission from clusters. Equipped with the angular diameter distance and redshift of a cluster a value of Hubble constant can be determined given an assumed cosmology. The beauty of this method is that it is completely independent of other techniques and that it can be used to measure distances at high redshifts directly.

3.2 Cosmology and Distance Measures

Modern cosmology has its origin in Edwin Hubble discovery of redshift-distance relationship. Using Cepheid variables as a standard candle together with spectroscopic observations of galaxies he found that the apparent recessional velocity, v of a galaxy was related to its distance as

$$v = H_0 d, \tag{3.1}$$

where H_0 is the Hubble constant, typically expressed in units $\mathrm{kmsec}^{-1}\mathrm{Mpc}^{-1}$. Such a relationship occurs naturally in the context of general relativity. The simplest cosmological solution to Einstein field equations are not static, but imply a space-time metric which changes as a function of time. Under the assumptions of isotropy and homogeneity, we find that the time independence of the metric is contained in a single factor $R(t)$ which corresponds to overall expansion or contraction of space. It can be then shown that for small value of d the constant H_0 is simply,

$$H(t_0) \equiv H_0 = \frac{\dot{a}(t_0)}{a(t_0)}. \tag{3.2}$$

In this work, we will denote the present time by t_0 and the current values of dynamic variables by H_0, a_0, etc. The Friedmann equation governs the dynamic evolution of a, which for flat universe has form,

$$\dot{a}(t)^2 = \frac{8\pi G}{3}\rho_m a(t)^2 + \frac{\Lambda}{3}a(t)^2, \tag{3.3}$$

where G is the gravitational constant, Λ is the cosmological constant, and ρ_m is the matter density of the universe. The matter density scales inversely as the volume of the universe so we write $\rho_m = \frac{\rho_0}{a(t)^3}$.

Now we define the critical density of the universe (the density at which the universe is flat) as,

$$\rho_c = \frac{3H(t)^2}{8\pi G}. \tag{3.4}$$

For convenience, we define the dimensionless density of the universe as,

$$\left. \begin{aligned} \Omega_m &= \frac{\rho_m}{\rho_c} = \frac{8\pi G \rho_m}{3H^2} \\ \Omega_\Lambda &= \frac{\Lambda}{3H^2} \end{aligned} \right\}. \tag{3.5}$$

For our flat universe, with these definitions we can rearrange the Friedmann equation into the form [100],

$$\left.\begin{array}{l} \Omega_m + \Omega_\Lambda = 1 \\[2mm] H(t) = H_0 \left(\dfrac{\Omega_{m,0}}{a(t)^3} + \Omega_{\Lambda,0} \right)^{\frac{1}{2}} \end{array}\right\}. \tag{3.6}$$

Because the universe is constantly expanding, there are multiple ways to define a distance measure. The redshift z of an object is defined as the fractional Doppler shift of the light emitted by the object as it moves away (or towards) us. Redshift is given by

$$z = \frac{\nu_e}{\nu_o} - 1 = \frac{\lambda_o}{\lambda_e} - 1, \tag{3.7}$$

where ν_e and λ_e are the emitted frequency and wavelength and ν_o and λ_o are the observed frequency and wavelength. Redshift serves as a distance measure because in our expanding universe more distant objects have higher redshifts. Redshifts can be related to the scale factor of the universe by nothing that the wavelengths of the radiation scales linearly with size of the universe, so that we have

$$\frac{\lambda_o}{\lambda_e} = \frac{1}{a(t)} = 1 + z, \tag{3.8}$$

where it is assumed that the observations is occurring now so that $a_0 = a(t_0) = 1$ and t is the time to which we are looking back, which is the time of emission of the radiation. Using Eq. (3.8) we can rewrite the Friedmann equation in terms of redshift as,

$$H(z) = H_0 \sqrt{\Omega_{m,0}(1+z)^3 + \Omega_{\Lambda,0}} = H_0 E(z), \tag{3.9}$$

where

$$E(z) = \sqrt{\Omega_{m,0}(1+z)^3 + \Omega_{\Lambda,0}}. \tag{3.10}$$

Let us define a set of co-moving coordinates that do not change as the universe expands. That is, the co-moving coordinates are constant with time for an object that moves solely with the expansion of the universe. In these Coordinates, the distance between any two objects at a time t is given by

$$d(t) = a(t)D_c = \frac{D_c}{1+z}, \tag{3.11}$$

where $d(t)$ is the proper distance, D_c is the constant co-moving distance, and $a(t)$ is the scale factor. Because $a_0 = 1$, the co-moving distance is the proper distance as measured today.

The line of sight co-moving distance can be calculated by considering a light ray traveling from an object to its observer as the universe expands. The light travels a distance cdt, but this distance is stretchered by the expansion of the universe. Therefore, we integrate over all the small distances along the trajectory of the light ray from the time of emission to the time of observation (now), obtaining the relation

$$D_c = \int_{t_e}^{t_o} \frac{cdt}{a(t)}. \tag{3.12}$$

From Eq. (3.8) we obtain the relation $\frac{dz}{da} = \frac{-1}{a(t)^2}$. Taking the function $E(z)$ and the definition of $H(z)$ in terms of scale factor, we obtain the relation $\frac{dt}{a(t)} = \frac{-dz}{H_0 E(z)}$. Therefore, the total line of sight distance is given by [101],

$$D_c = \frac{c}{H_0} \int_0^z \frac{dz'}{\sqrt{\Omega_{m,0}(1 + z')^3 + \Omega_{\Lambda,0}}}. \tag{3.13}$$

The Hubble flow is the uniform expansion of the universe. Any velocity due to motion other than the expansion of the universe is known as peculiar velocity. The comoving distance is constant over time between two objects locked in the Hubble flow with no peculiar velocities. It gives us the distance as of today to an object that we are viewing, even though we are viewing the object as it was in the past when it was closer to us.

For our study of galaxy clusters, we will be interested in transverse separation: separations between two objects at the same redshift $(dz = 0)$ which are observed at the same time but are separated on the sky by some angle $\delta\theta$. We denote D_s the co-moving distance perpendicular to the line-of-sight between two objects which are separated by an angle $\delta\theta$. For a flat space-time $D_s = D_c\delta\theta$, so D_c relates an observed angle co-moving separation on the sky. However, we want a distance measure that relates an observed angle on the sky to the proper distance between two objects at the time the light was emitted. To obtain this we simply multiply the co-moving distance D_c by the scale factor at the time of emission, $a(t)$, which is equivalent to dividing by $(1 + z)$. This gives the angular
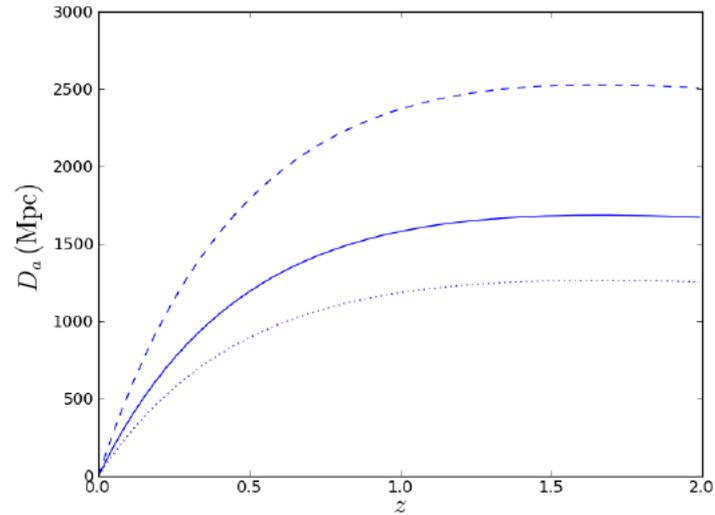
Figure 3.2: Angular diameter distance as a function of redshift. Hubble parameter: $H_0 = 50 \mathrm{kms}^{-1}\mathrm{Mpc}^{-1}$ (dashed line), $H_0 = 70 \mathrm{kms}^{-1}\mathrm{Mpc}^{-1}$ (solid line), and $H_0 = 100 \mathrm{kms}^{-1}\mathrm{Mpc}^{-1}$ (dotted line). Here $\Omega_m = 0.26$, $\Omega_\Lambda = 0.74$. Source-http://physics.princeton.edu/act/papers/sfrazierJP.pdf.

diameter distance, D_a [101],

$$D_a = \frac{c}{H_0(1+z)} \int_0^z \frac{dz'}{\sqrt{\Omega_{m,0}(1+z')^3 + \Omega_{\Lambda,0}}}. \tag{3.14}$$

The angular diameter distance is the ratio of an object's physical transverse size to its angular size (in radians). It is useful because it converts angular separations in telescope images into proper distance separations at the source. It will be the distance measure of interest for this study. It has the strange property that it does not increase indefinitely as the redshift of the object increases. Rather, at $z \approx 1.5$ it turns over and begins to decrease. This is because it is inversely proportional to the object's size on the sky. Due to the constant expansion of the universe, as an object's distance from us increases and there is a point ($z \approx 1.5$) where the object will appear larger on the sky the farther away it is because it is larger compared to the relative size of the entire universe at that time. At this point, the angular diameter distance will begin to decrease because the angular size will increase. Fig. (3.2) shows how angular diameter distance varies with z.

Very often it is necessary to relate a radiation flux S measured on earth to the objects

luminosity L. In Euclidean geometry these are related as,

$$S = \frac{L}{4\pi d^2}. \tag{3.15}$$

One may now define the luminosity distance D_l, so that Eq. (3.15) holds true with $d = D_l$ for any space-time. The luminosity distance is given by

$$D_l = (1 + z)D_c = (1 + z)^2 D_a, \tag{3.16}$$

such that [101],

$$D_l = \sqrt{\frac{L}{4\pi S}}, \tag{3.17}$$

where S is the flux from the source.

3.3   X-ray Emission from Galaxy Clusters

Clusters of galaxies are luminous X-ray sources, with X-ray luminosities ranging from 10^{43} to 10^{46} erg s^{-1} [36]. X-ray emission is expected in ICM which contain gas at temperatures in the order of million kelvins, in which the constituents particles have high energy. As the gas cools down it emits X-rays. The emission is a combination of bremsstrahlung and emission lines from highly ionized iron and other heavy elements [102]. Bremsstrahlung refers to the production of radiation by the acceleration of a charged particle when deflected by another charged particle. Therefore, the intensity of bremsstrahlung is proportional to the gas density squared. Spectral lines are the result of interaction between atoms and photons. Each element has its own characteristic emission and absorption line, therefore, the analysis of line emission from the gas allows the determination of its chemical characteristics [103]. For cluster temperatures $k_B T \geq 2$ keV, the emissivity of thermal bremsstrahlung dominates that from emission lines, but below 2 keV emission lines dominate. ICM typically have temperatures between $10^7 - 10^8$ (roughly $5 - 10$ keV), so it is expected that main contribution is from bremsstrahlung.

The bremsstrahlung emissivity integrated over frequencies, defined as the emitted luminosity L pet unit volume V, is given by [104],

$$\epsilon = \frac{dL}{dV} = n_e n_i \Lambda_{ei}. \tag{3.18}$$

where f_e and f_i are the number densities of electrons and ions respectively (we assume that the gas is mostly hydrogen so that $n_i = n_H$) where n_H is the number density of hydrogen gas), and $\Lambda_{ei} = \Lambda_{eH}$ is the X-ray cooling function of the ICM in the cluster rest frame, integrated over frequencies. The luminosity per unit area of the source can be then obtained by integrating the emissivity along the line of sight through the ICM gas. However, we want a luminosity per unit solid angle Ω, and changing from unit area to unit solid angle gives a factor of D_a^2 (area $= D_a^2 d\Omega$). This yields,

$$\frac{L}{d\Omega} = D_a^2 \int n_e n_H \Lambda_{eH} dl, \tag{3.19}$$

for luminosity per unit solid angle. Using Eqs. (3.16) and (3.17) we have,

$$(1+z)^4 D_a^2 F = D_a^2 \int n_e n_H \Lambda_{eH} dl. \tag{3.20}$$

The X-ray flux per unit solid angle, or X-ray surface brightness is then given by

$$S_x = \frac{1}{4\pi(1+z)^4} \int n_e n_H \Lambda_{eH} dl. \tag{3.21}$$

We define $\mu_j = \frac{\rho}{n_j m_p}$, as the mean molecular weight per species j, where ρ is the gas mass density and m_p is the mass of the proton. We can then write $n_H = \frac{n_e \mu_e}{\mu_H}$ in which μ_H is the mean molecular weight of the gas per hydrogen ion and μ_e is the mean molecular weight of the gas per free electron. Characteristic values for these mean molecular weights are $\mu_H = 1.40$ and $\mu_e = 1.17$. Our final expression for the X-ray surface brightness is then

$$S_x = \frac{1}{4\pi(1+z)^4} \frac{\mu_e}{\mu_H} \int n_e^2 \Lambda_{eH} dl. \tag{3.22}$$

3.4 Isothermal β-Model

The gas in a cluster is trapped by the cluster gravitational potential well. If the hot gas is supported by its own pressure against gravitational inward force, it must obey the equation of hydrostatic equilibrium. Assuming spherical symmetry, we have,

$$\nabla P_{gas}(r) = -\rho_{gas} \nabla \Phi(r), \tag{3.23}$$

where $P_{gas}(r)$ is the radial pressure profile of the gas, ρ_{gas} is the mass density of the gas and $\Phi(r)$ is the symmetric gravitational potential. Next we consider the galaxies having an isotropic velocity dispersion function,

$$f(\vec{v})d\vec{v} = 4\pi v^2 f(v)dv, \tag{3.24}$$

where we assume $f(v)$ is the Maxwellian velocity distribution. The observed line of sight velocity dispersion of the galaxies is given by,

$$\sigma_r^2 = \frac{1}{3}\int d\vec{v}\vec{v}^2 f(\vec{v}) = \frac{4\pi}{3}\int dv v^4 f(v). \tag{3.25}$$

The factor $\frac{1}{3}$ is present because we are only taking into account consideration the measurable line of sight velocity dispersion. Observationally, the line of sight velocity dispersion is defined as,

$$\sigma_r^2 = \frac{1}{N}\sum_{i=1}^{N} v_i^2, \tag{3.26}$$

where the v_i's are the individual galaxy velocities and N is the number of galaxies. Let ρ_{gal} be the mass density of the galaxies. Considering galaxy distribution to be isothermal, so that σ_r is constant throughout the cluster we then define galaxy pressure P_{gas} as,

$$P_{gal} = \rho_{gal}(r)\sigma_r^2. \tag{3.27}$$

We can treat the galaxies as a gas in hydrostatic equilibrium, which gives equation similar to Eq. (3.23),

$$\nabla P_{gal}(r) = -\rho_{gal}\nabla\Phi(r), \tag{3.28}$$

The galaxy and gas radial distribution, ρ_{gal} and ρ_{gas} can then be directly related via the equilibrium equations:

$$\frac{\nabla P_{gas}(r)}{\rho_{gas}} = -\nabla\Phi(r) = \frac{\nabla P_{gal}(r)}{\rho_{gal}}. \tag{3.29}$$

Using ideal gas equation $P_{gas}(r) = n_{gas}(r)k_B T(r)$, where n_{gas} is the number density profile of the gas molecules and $\rho_{gas}(r) = \mu m_p n_{gas}(r)$, we obtain for $T(r) = T$ (constant)

[105, 106, 107]

$$\frac{1}{n_{gas}} \frac{d((\frac{k_B T}{\mu m_p}) n_{gas})}{dr} = \frac{1}{\rho_{gal}} \frac{d(\rho_{gal} \sigma_r^2)}{dr}$$
$$\Rightarrow \frac{dn_{gas}(r)}{n_{gas}(r)} = \frac{\sigma_r^2 \mu m_p}{k_B T} \frac{d\rho_{gal}(r)}{\rho_{gal}(r)}. \tag{3.30}$$

Integrating

$$n_{gas} = n_0 \left[\frac{\rho_{gal}(r)}{\rho_{gal}(0)} \right]^{\beta}, \tag{3.31}$$

where

$$\beta = \frac{\sigma_r^2 \mu m_p}{k_B T}, \tag{3.32}$$

and $n_0 = n(0)$ is the central number density of gas particles. β simply is the ratio of the specific kinetic energy of the galaxies to that of the gas and is mostly less than unity. This clearly implies that the intra-cluster gas has more specific kinetic energy.

Typically, the X-ray surface brightness profile is well fitted by the function form known as the β-model [107],

$$S_x(\theta) = S_x(0) \left[1 + \frac{\theta^2}{\theta_c^2} \right]^{\frac{1}{2} - 3\beta}, \tag{3.33}$$

where $S_x(0)$ is the central surface brightness and $\theta_c = \frac{r_c}{D_a}$ is the angular core radius of the cluster, r_c is the core radius. This model has been widely used to fit the X-ray images of the clusters of galaxies[108]. If one assumes that the diffuse X-ray emitting gas in cluster is isothermal and spherical Eq. (3.22) can be easily changed to the form of Abel integration. Inverting the equation one can obtain the gas distribution from the X-ray surface brightness, for the above standard β-model, Eq. (3.33) [109, 110],

$$n_{gas}(r) = n_0 \left[1 + \left(\frac{r}{r_c} \right)^2 \right]^{-\frac{3\beta}{2}}. \tag{3.34}$$

If we assume that the electron number density $n_e(r)$ follows the total gas molecule number density $n_{gas}(r)$, then the electron distribution is given by,

$$n_e(r) = n_{e0} \left[1 + \left(\frac{r}{r_c} \right)^2 \right]^{-\frac{3\beta}{2}}. \tag{3.35}$$

This model for the electron number density as a function of radial distance from the cluster is the isothermal β model. The mass of the hot gas present in the ICM is determined by the integration of the gas density profile,

$$M_{gas} = 4\pi^2 \rho_0 \int r^2 \left[1 + \left(\frac{r}{r_c}\right)^2\right]^{-\frac{3\beta}{2}}. \tag{3.36}$$

We also have a more sophisticated cluster gas model that takes into account temperature profile. A motivation for considering this model is to assess the biases arising from the isothermal assumption. The assumption of isothermality of the intra-cluster medium is not always valid as some clusters can host cool cores. The non-isothermal double β model uses second β model component to describe the sharply peaked X-ray emission present in the cores of some clusters [111, 112]. The density profile of the double-β model is expressed by,

$$n_e(r) = n_{e0} \left[f \left[1 + \left(\frac{r}{r_c}\right)^2\right]^{-\frac{3\beta}{2}} + (1 - f) \left[1 + \left(\frac{r}{r_c'}\right)^2\right]^{-\frac{3\beta}{2}} \right], \tag{3.37}$$

where the two core radii, r_c and r_c' describe the narrow, peaked central density component and the broad, shallower density profile, respectively, and f represents the fractional contribution of the narrow, peaked component to the central density n_{e0} ($0 \leq f \geq 1$). This model have enough freedom to simultaneously fit the X-ray surface brightness in the outer region and the central emission excess seen in some clusters.

Recent high resolution N-body/hydrodynamical simulations of structure formation in standard cold dark matter (SCDM) cosmological models have strongly suggested that the dark matter halos of clusters scales could be generally described by universal density profile proposed by Navarro, Frenk, and white (NFW) [113, 114],

$$\rho(r) = \frac{\rho_s}{\frac{r}{r_s}(1 + \frac{r}{r_s})^2}, \tag{3.38}$$

where r_s and ρ_s are the characteristic scaling radius and density, respectively. This enables one to predict profile of the gas and X-ray surface brightness. If one assumes that the diffuse X-ray emitting gas in cluster is isothermal and traces the gravitational potential define by NFW profile Eq. (3.38) and neglecting the gas and galaxy contribution to the
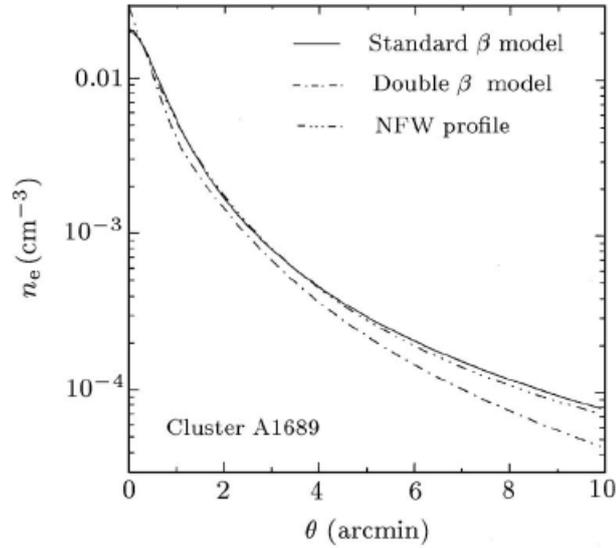
Figure 3.3: Electron number density of the cluster Abell 1689 given by the X-ray surface brightness fitting parameters plotted verses angular distance from the cluster center [105].
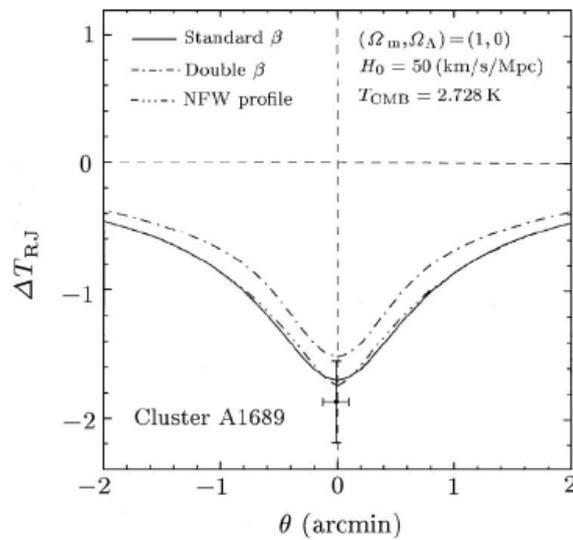

Figure 3.4: Resulting S-Z thermal temperature decrement profile (mK) of a cluster Abell 1689 from β-model, double β-mode and the universal density profile [105].

gravitational potential, the NFW profile predicts an analytic form of electron density

$$n_e(r) = n_e(0)e^{-\alpha} \left[1 + \frac{r}{r_s}\right]^{\frac{\alpha}{\left(\frac{r}{r_s}\right)}},$$ (3.39)

where $\alpha = \frac{4G\pi\mu_{gas}m_p\rho_s r_S^2}{k_B T_{gas}}$. We can adopt these three models i.e standard β model, double β model and the profile from NFW dark matter halo to fit the observed X-ray surface brightness profile S_x of the cluster, which yields the core radius $r_c(r_s)$ and $\beta(\alpha)$ parameters. After obtaining the model parameters through fitting the X-ray surface brightness, it is straight forward to calculate the resulting electron number density. Electron number density of the cluster Abell 1689 from the three different models is shown in Fig. (3.3). With the electron number density of the cluster it is easy to calculate S-Z effect. Fig. (3.4) shows the resulting S-Z temperature decrement (R-J region) profiles of the cluster Abell 1689 from the three models considered. The predicted effect profile from standard β model and NFW dark matter halo are similar except the value is little deeper at center for NFW profile.

The isothermal β-model is, however, a simple model. It provides a good fit to observed cluster profiles in the intermediate range $100\text{Kpc} \leq r \leq 1\text{Mpc}$ [115], and this range often contains enough information so that fitting the β model to the data still provide the useful information. Many recent studies of galaxy clusters still use the β-model. They often exclude the central 100Kpc of the X-ray data in order to avoid the complicated core physics in which the non-equilibrium physics dominates and they also do not fit the model to the data in the outskirts of the cluster because the density profiles drop off more faster in the outskirts of clusters ($r \geq 1\text{Mpc}$). They fit the model to the data in the intermediate region and then extend this fit into the other two regions, which turns out to be a reasonable approximation in many cases. Therefore the β model can still be used for ICM if it is applied correctly.

3.5 Determining Angular Diameter Distances and Hubble Constant

We now briefly describe the method used to determine Hubble constant on the basis of S-Z effect. As said earlier this method uses two observable quantities which are specified by the hot gas in cluster of galaxies; one is the temperature decrement $\frac{\Delta T}{T}$ of the

cosmic microwave background radiation due to S-Z effect; the other is the X-ray surface brightness S_x of the cluster of galaxies. Theoretically from Eqs. (3.22) & (2.40) [116, 117],

$$S_x = \frac{1}{4\pi(1+z)^4} \frac{\mu_e}{\mu_H} \int n_e^2 \Lambda_{eH} dl \qquad (3.40)$$

$$\Delta T_{RJ} = -2T \frac{k_B \sigma_t}{m_e c^2} \int n_e T_e dl. \qquad (3.41)$$

It is convenient to express the electron concentration and temperature in terms of a reference electron concentration (which will be taken to be central electron concentration and temperature here as done earlier , although the values at any fiducial point may be chosen) and the dimensionless form factor describing the angular structure of the atmosphere in density $f_n(\theta, \phi, \zeta)$ and temperature $f_t(\theta, \phi, \zeta)$,

$$\left. \begin{array}{l} n_e(r) = n_{e0} f_n(\theta, \phi, \zeta) \\ T_e(r) = T_{e0} f_t(\theta, \phi, \zeta) \end{array} \right\}, \qquad (3.42)$$

where a cylindrical angular coordinate system has been used. Here, θ is the angle from a reference line of sight, ζ is the angular measure of distance ($l = \zeta D_a$), and ϕ is an azimuthal angle about reference line. Then the Λ_{eH} may be written as

$$\Lambda_{eH} = \Lambda_{eH0} f_\Lambda(\theta, \phi, \zeta). \qquad (3.43)$$

If the intracluster medium is isothermal, then f_t and f_Λ will be equal to unity- temperature and X-ray spectral emission are constant over cluster.

The expressions for X-ray surface brightness and Sunyaev-Zel'dovich effect then becomes,

$$\begin{aligned} S_x(\theta, \phi) &= \frac{1}{4\pi(1+z)^4} n_{e0}^2 \Lambda_{eH0} D_a \frac{\mu_e}{\mu_H} \int f_n^2 f_\Lambda d\zeta \\ &\equiv N_x \Theta_1 \end{aligned} \qquad (3.44)$$

$$\begin{aligned} \Delta T_{RJ}(\theta, \phi) &= -2T \frac{k_B \sigma_t}{m_e c^2} T_{e0} n_{e0} D_a \int f_n f_t d\zeta \\ &\equiv -N_{RJ} \Theta_2, \end{aligned} \qquad (3.45)$$

where the structural information on the cluster is contained in angles,

$$\Theta_1(\theta, \phi) = \int f_n^2 f_\Lambda d\zeta \tag{3.46}$$

$$\Theta_2(\theta, \phi) = \int f_n f_t d\zeta. \tag{3.47}$$

and

$$N_x = \frac{1}{4\pi(1+z)^4} n_{e0}^2 \Lambda_{eH0} D_a \frac{\mu_e}{\mu_H} \tag{3.48}$$

$$N_{RJ} = 2T \frac{k_B \sigma_t}{m_e c^2} T_{e0} f_{e0} D_a. \tag{3.49}$$

If N_x and N_{RJ} can be measured from X-ray and Sunyaev-Zeldovich data, and the density and temperature structure function of the atmosphere are known, then the angular diameter distance of the cluster can be found as,

$$D_a = \frac{N_{RJ}^2}{N_x} \left(\frac{m_e c^2}{k_B T_{e0}}\right)^2 \frac{\mu_e}{\mu_H} \frac{\Lambda_{eH0}}{16\pi T^2 \sigma_t^2 (1+z)^3}. \tag{3.50}$$

Alternatively, the reference density n_{e0} may be deduced in a distance independent manner by eliminating D_a as,

$$n_{e0} = \frac{N_{RJ}}{N_x} \left(\frac{m_e c^2}{k_B T_{e0}}\right) \frac{\mu_e}{\mu_H} \frac{\Lambda_{eH0}}{8\pi T \sigma_t (1+z)^3}. \tag{3.51}$$

Once the angular diameter distance to a galaxy cluster is determined, one can estimate the Hubble parameter given the cluster redshift and assumed cosmology by rearranging Eq. (3.14),

$$H_0 = \frac{c}{D_a(1+z)} \int_0^z \frac{dz'}{\sqrt{\Omega_{m,0}(1+z')^3 + \Omega_{\Lambda,0}}}. \tag{3.52}$$

Sine the intrinsic (three dimensional) density and temperature structures of the clusters and hence f_n, f_t and f_Λ are unknown it is clear that a wide variety of such structures are likely to be capable of reproducing the noise measurements of the spectrum S_x and ΔT_{RJ} after allowing for convolution with the response of telescope used. For this reason, some assumptions about the forms of f_n, f_t and f_Λ are crucial to extracting the angular diameter distance and hence the value of H. We have briefly discussed these assumptions in the previous section and the three main assumptions are listed below

1) It will be assumed that the atmosphere is isothermal so that $T_e(r) = T_{e0} = T_{iso}$, the central gas temperature. This has a effect of factoring the temperature out of the problem: $\Lambda_{eH}(T_e)$ becomes constant $\Lambda_{eH0} \equiv \Lambda_e(T_{e0})$ and $f_\Lambda = f_t = 1$.

2) It will be assumed that the atmosphere is spherical so that $n_e(r)$ may be written as a function of r, the distance from the cluster center. Thus $f_n = f_n[(\theta^2 + \zeta^2)^{\frac{1}{2}}]$.

3) It will be assumed that the gas distribution follows β model i.e Eq. (3.35), so that

$$f_n = \left[1 + \left(\frac{\theta^2 + \zeta^2}{\theta_c}\right)\right]^{-\frac{3\beta}{2}}. \tag{3.53}$$

With these assumptions about the form factors, the angles Θ_1 and Θ_2 are independent of ϕ and may be expressed as simple functions of angular offset from the projected cluster center, θ, core radius, θ_c and the energy parameter, β.

It is clear that if completely general forms for f_n and f_t perhaps involving substantial small-scale density and temperature structures (clumping) are allowed, then it is unlikely that any X-ray and S-Z effect can provide sufficient constrain on the functions for H to be determined unambiguously. However, provided that the mean values of the density and temperature vary slowly over the cluster, and that the amplitude and type of the clumping are also not strong functions of position, strong conclusions in the value of Hubble constant can still be obtained.

Explicitly,

$$\begin{aligned}
\Theta_1 &= \int f_n^2 d\zeta \\
&= \theta_c \int \left[1 + \left(\frac{\theta^2 + \zeta^2}{\theta_c^2}\right)\right]^{-3\beta} d\left(\frac{\zeta}{\theta_c}\right) \\
&= \sqrt{\pi}\frac{\Gamma(3\beta - \frac{1}{2})}{\Gamma(3\beta)}\theta_c \left[1 + \frac{\theta^2}{\theta_c^2}\right]^{\frac{1}{2}-3\beta} \tag{3.54}
\end{aligned}$$

$$\begin{aligned}
\Theta_2 &= \int f_n d\zeta \\
&= \theta_c \int \left[1 + \left(\frac{\theta^2 + \zeta^2}{\theta_c^2}\right)\right]^{-\frac{3\beta}{2}} d\left(\frac{\zeta}{\theta_c}\right) \\
&= \sqrt{\pi}\frac{\Gamma(\frac{3\beta}{2} - \frac{1}{2})}{\Gamma(\frac{3\beta}{2})}\theta_c \left[1 + \frac{\theta^2}{\theta_c^2}\right]^{\frac{1}{2}-\frac{3\beta}{2}}. \tag{3.55}
\end{aligned}$$

where we have used the following identity in Eqs. (3.54) and (3.54),

$$\int (1 + A^2 + B^2)^{-C} dA = \sqrt{\pi} \frac{\Gamma(C - \frac{1}{2})}{\Gamma C} \left(1 + B^2\right)^{\frac{1}{2} - C},$$
(3.56)

where Γ is a gamma function.

From Eq. (3.44) and (3.45), we get,

$$
\begin{aligned}
S_x(\theta) &= \frac{1}{4\pi(1 + z)^4} n_{e0}^2 \Lambda_{eH0} r_c \frac{\mu_e}{\mu_H} \sqrt{\pi} \frac{\Gamma(3\beta - \frac{1}{2})}{\Gamma(3\beta)} \left[1 + \frac{\theta^2}{\theta_c^2}\right]^{\frac{1}{2} - 3\beta} \\
&= S_{x0} \left[1 + \frac{\theta^2}{\theta_c^2}\right]^{\frac{1}{2} - 3\beta}
\end{aligned}
$$
(3.57)

$$
\begin{aligned}
\Delta T_{RJ}(\theta, \phi) &= -2T \frac{k_B \sigma_t}{m_e c^2} T_{iso} n_{e0} r_c \sqrt{\pi} \frac{\Gamma(\frac{3\beta}{2} - \frac{1}{2})}{\Gamma(\frac{3\beta}{2})} \left[1 + \frac{\theta^2}{\theta_c^2}\right]^{\frac{1}{2} - \frac{3\beta}{2}} . \\
&= \Delta T_0 \left[1 + \frac{\theta^2}{\theta_c^2}\right]^{\frac{1}{2} - \frac{3\beta}{2}},
\end{aligned}
$$
(3.58)

where S_{x0} and ΔT_0 are the central values of X-ray surface brightness and S-Z temperature change ($r = 0$).

Since both central temperature decrement and X-ray surface brightness are observed, one can then combine Eqs.(3.57) and (3.58) to estimate the core radius [116] as,

$$
\begin{aligned}
r_{c,est} &= \frac{\left[\frac{\Delta T}{T}\right]_{obs}^2 \Gamma(3\beta - \frac{1}{2}\Gamma\left(\frac{3\beta}{2}\right)^2}{[S_x]_{obs} \Gamma\left(\frac{3\beta}{2} - \frac{1}{2}\right)^2 \Gamma(3\beta)} \frac{\mu_e}{\mu_H} \times \\
&\qquad \frac{m_e^2 c^4 \Lambda_{eH}}{16\pi^{\frac{3}{2}} (1 + z)^4 \sigma_t^2 k_B^2 T_{e,fit}^2} \left[1 + \left(\frac{\theta}{\theta_c}\right)^2\right]^{-\frac{1}{2}} .
\end{aligned}
$$
(3.59)

In the above equation $T_{e,fit}$ is the X-ray flux averaged temperature obtained from fitting the observed X-ray spectrum to the theoretical spectrum expected from isothermal case. This X-ray emission weighted temperature is given by

$$T_{e,iso} = \frac{\int_0^{r_{vir}} T_e(r) \Lambda_{eH} n_e^2 r^2 dr}{\int_0^{r_{vir}} \Lambda_{eH} n_e^2 r^2 dr},$$
(3.60)

where r_{vir} is the virial radius of the cluster and its choice depends on the observer. Here, we also can get the estimate of $D_a = \frac{r_c}{\theta_c}$ and hence the Hubble constant.

As can be seen from Eq. (3.60), the value of H depends crucially on the assumptions of isothermality and β-model density distribution of the cluster. Cooling flow changes both these and so it can significantly affect the value of the Hubble constant. This will be discussed in the last section of this chapter.

3.6   Aspherical Cluster Atmosphere

Simple limits to the effects of asphericity on the estimate of the Hubble constant can be deduced by supposing that the atmosphere is prolate or oblate, rather than spheroidal, with the unique axis oriented along the line of sight. This is, in a sense, the most extreme variation of the geometry of the original spherical model: if the unique axis is oriented in any direction, some changes in the shape of the X-ray isophotes should be measured. However, if the unique axis lies along the line of sight, then the apparent X-ray surface brightness (or Sunyaev- Zel'dovich effect; or galaxy distribution) will have a circular symmetry, and it will be difficult to determine that such a distortion of the cluster exists.

If the orientation of the unique axis is along the line of sight, with the core radius of the gas density distribution in the z-direction larger by a factor Z than the core radii in the other two directions, the density form factor will follow[117, 118],

$$
\begin{aligned}
f_n &= \left[1 + \frac{x^2 + y^2 + \frac{z^2}{Z^2}}{r_c^2} \right]^{-\frac{3\beta}{2}} \\
&= \left[1 + \frac{\theta^2 + \frac{\varsigma^2}{Z^2}}{\theta_c^2} \right]^{-\frac{3\beta}{2}} .
\end{aligned}
\tag{3.61}
$$

$Z > 1$ corresponds to a prolate gas distribution, while $Z < 1$ corresponds to an oblate distribution. With this modification, the expressions for Θ_1 and Θ_2 remain valid, while the N_x and N_{RJ} both increase by a factor of Z. Eq. (3.50) for the angular diameter distance is also modified, and becomes,

$$
D_a = \frac{N_{RJ}^2}{N_x} \left(\frac{m_e c^2}{k_B T_{e0}} \right)^2 \frac{\mu_e}{\mu_H} \frac{\Lambda_{eH0}}{16\pi T^2 \sigma_t^2 (1+z)^3} \frac{1}{Z} .
\tag{3.62}
$$

So that the value of D_a calculated assuming $Z = 1$ will differ from the true angular diameter distance of the cluster by a factor

$$\frac{D_a(\text{true})}{D_a(\text{estimated})} = \frac{1}{Z}.$$ (3.63)

If the cluster is highly prolate $Z \ll 1$, then the true angular diameter distance will be much smaller than distance deduced on the basis of Eq. (3.50) and hence the value of Hubble constant estimated will be an underestimate.

3.7 Recent Results on Hubble Constant

The following is a brief overview of some recent results given by the S-Z effect as given in a review by Rephaeli [10] and some more recently published values from Mason, Meyers, and Readhead [119], Reese et al [95], and an improved method carried out by Schmidt, Allen, and Fabian [98].

Before 1995, the practical complications were the main cause in the varied range in values for H_0. In a review of the literature that had been published from 1990 to 1995, Rephaeli [10] listed a table with the measured values of H_0 as determined from 7 separate clusters, with some duplication. There was a very wide range of values, from approximately 24 to 82 kms^{-1}Mpc^{-1}, with an average of $H_0 = 54$kms^{-1}Mpc^{-1}. Mason, Myers, and Readhead [119] studied Seven clusters with $z < 1$ using the same method as had been done in the previous review with a range from 36 to 102kms^{-1}Mpc^{-1} and an average of 64 kms^{-1}Mpc^{-1} for a standard cold dark matter (SCDM) cosmology and 66 kms^{-1}Mpc^{-1} for a flat Λ CDM cosmology. Reese et al. [95] determined distances to 18 galaxy clusters ($0.14 < z < 0.78$) and the final result was $H_0 = 60$kms^{-1}Mpc^{-1} for an $\Omega_M = 0.3$, $\Omega_\Lambda = 0.7$ cosmology. In one of the most recent papers Schmidt, Allen, and Fabian [98] published an improved method was presented for predicting the effect and carrying out the observations. The main advantage to their new method was extrapolating a pressure profile of the X-ray gas, allowing the Comptonization parameter to be predicted precisely. Applying their method to Chandra observations of three clusters, they found $H_0 = 69 \pm 8$ kms^{-1}Mpc^{-1} for an $\Omega_M = 0.3$, $\Omega_\Lambda = 0.7$ cosmology. This result is in excellent agreement with the recent value of $H_0 = 71.1 \pm 2.5$kms^{-1}Mpc^{-1} from seven year WMAP data [27].

3.8 Systematic Errors in the Hubble Constant

The values of Hubble constant based on measurements of the Sunyaev-Zel'dovich effect in the clusters of galaxies are systematically lower than those derived by other methods like Cepheid variable stars. In particular, it has been found that non-isothermality, non-spherical, clumpiness of the ICM and a host of other factors can give rise to either over or under estimation of the Hubble constant [120, 121]. At present, the observational uncertainties are, perhaps the biggest source of error in the determination of H_0. Here we briefly summarize a few of the uncertainties.

1) The first uncertainty in the determination of Hubble constant comes from Eq. (3.57) and (3.58). These equations were derived under the assumption of the cluster being infinite size. This is surely not the case, and the cluster can extend only up to some finite size given by R_{cl}, and $f_e = T = 0$ for $r > R_{cl}$. Integrating analytically, the Gamma function in these equations must be changed to a combination of Beta and incomplete-Beta functions. As a result, the observed values of $\frac{\Delta T}{T}$ and S_x would be lower than their estimates based on the assumption of an infinite cluster. Also, due to the the fact that the S-Z profile is more extended than X-ray profile, it is seen that the $\frac{\Delta T}{T}$ is lower by $5-10\%$. However, the X-ray surface brightness is almost unchanged.

2) Another systematic uncertainty comes from the assumption of isothermality for the cluster medium. This can lead to substantial change in S-Z effect and thus the value of H_0 [122, 123]. In obtaining Eq. (3.57) and (3.58) one assumed isothermal temperature and if there is a temperature gradient, then the estimation of isothermal temperature would depend on the maximum radius up to which the temperature profile is observed Eq. (3.60). As it is difficult to obtain spectroscopic temperatures up to large radial distances, the evaluation of Eq. (3.60) is handicapped. Another source of error is the complicated dependence of S_x on temperature. However, it is found that this dependence is weak. It is estimated that non-isothermality can lead to an underestimation of H_0 by $\sim 20\%$, if the temperature in outer parts of the cluster is lower than in the inner part [124].

3) An important source of statistical error is asphericity of the cluster atmosphere [117, 125, 126]. As discussed in the earlier section the value of H_0 will be underestimated if the cluster is prolate and overestimated if the cluster is oblate. Effect of asphericity of galaxy clusters on the determination of Hubble constant can lead to an error u to 30% for specific cases [126]. There remains the possibility that this effect can be averaged out in an ensemble of clusters selected on the basis of integrated X-ray flux.

4) Clumpiness of the intracluster medium can also be a source of error. The assumption that goes into interpreting the observations is that density variations on scales that are unresolved are small. However, strong clumping can affect the X-ray emissivity ($\propto n_e^2$) more than S-Z effect ($\propto n_e$). It can be shown that $\frac{D_a(true)}{D_a(estimate)}$ = clumping factor ($\frac{<f_e^2>}{<f_e>^2}$). Hence if the ICM is significantly clumped, then H_0 is overestimated. Unlike asphericity, clumping cannot be averaged out from the cluster to cluster, since all clusters do have some varying degree of clumpiness [127, 128, 129]. Clumpiness can lead to overestimation of the Hubble constant by about 10-15% in a SCDM universe [116].

5) Measurements of thermal S-Z effect is always contaminated by the presence of the kinematic S-Z effect. As long as they are not separated out using multi frequency observations, the kinematic S-Z effect act as an additional source of temperature distortion. There can be over or underestimation according to relative sign of cluster velocity. In CDM universes, cluster velocity can have a range of values between 300-400kms^{-1} and hence the error due to the kinematic S-Z effect is generally less than 5%

6) Another source of uncertainty comes from inaccurate knowledge of the X-ray Bremsstrahlung emissivity, where mostly non-relativistic expression are used. These relativistic corrections to the S-Z decrement can be important for cluster with $T > 5$ keV. Hence, corrections to both S_x and $\frac{\Delta T}{T}$ should be incorporated for more reliable evaluation of H_0. However, the inclusion of relativistic corrections lead to small change in the final value of H_0 of the order of $\sim 1 - 2\%$ [118].

7) The value of Hubble constant depends on our knowledge of the cosmological parameters Ω_m and Ω_Λ. As long as the redshift of the clusters is less than 0.2, D_a does not change significantly with small variation in the presently acceptable values of the cosmological parameters. For example, changing deceleration parameter from 0 to 0.5 for Clusters A665 or A2218 (having $z \sim 0.17 - 0.18$) would lead to a change in H_0 by $\sim 3\%$. For a high redshift clusters lie CL $0016 + 16$, the changes in H_0 due to the different cosmology can be higher by $\sim 5 - 10\%$ [130, 131]

8) Loeb-Refregier effect [132] can lead to underestimation of the Hubble constant inferred from S-Z effect. Measurement of S-Z effect takes into account the subtraction of the background radio sources from the cluster field. The gravitational lensing by the cluster can, however, lead to a systematic deficit in the residual intensity of the unresolved sources behind the cluster relative to a field far from the cluster center, resulting in the over estimation of the R-J temperature of the microwave background radiation. This gives rise

to a systematic bias and can lead to underestimation of H_0 by $\sim 5 - 10\%$.

9) Another possible source of error comes from the possible presence of a non-thermal component of electron population. Large scale hydrodynamics simulations of clusters show that it may be possible to have a non-thermal pressure, close to the cluster center, to a significant fraction of the thermal gas pressure. If this is the case, then it would affect the determination of the dynamical mass and the cluster gas β profile and would also add a non-thermal S-Z component to the already present thermal distortion.

10) We have studied many possible sources of errors in the determination of the Hubble constant using S-Z effect. We now turn to another important phenomenon that will be briefly discussed in the next section which can substantially change the temperature structure in the innermost of a cluster, $viz.$ a cooling flow and thus be another source of uncertainty. Cooling flows in the cluster of galaxies is claimed to be well established fact by now. The idealized picture of a cooling flow is as follows: initially when the cluster forms the in falling gas is heated due to the gravitational collapse. With time this gas cools slowly and a quasi hydrostatic state emerges. However, in the central region, where energy is lost due to the radiation transfer faster than elsewhere, an inward 'cooling flow' initially arises due to the pressure gradient. This can modify the S-Z decrement and act as a systematic source of error in the determination of the cosmological parameter.

3.9   Clusters with Cooling Flows

The cooling-flow model was first proposed by Cowie & Binney[133]. Extensive reviews can be found in Sarazin [108] and Fabian [135]. From the X-ray spectra of clusters, it is known that the continuum emission is the Thermal Bremsstrahlung in nature and originates from diffuse intra-cluster gas with densities $10^{-2}\mathrm{cm}^{-3} - 10^{-4}\mathrm{cm}^{-3}$ and the temperature around $10^7\mathrm{K} - 10^8\mathrm{K}$ which is usually believed to be in hydrostatic equilibrium. If, however, the density in the inner region is large enough that the cooling time (t_{cool}) is less than the age of the cluster ($t_a = H_0^{-1}$), then there is a cooling flow. Of course, there will be flow only when the cooling time scale is larger than the gravitational free-fall time scale, t_{dyn} Thus, for the innermost regions,

$$t_a > t_{cool} > t_{dyn}. \tag{3.64}$$

Due to the cooling of the gas, the pressure in the innermost parts drops, and to support the weight of the overlaying material above some radius, r_{cool}, an inflow takes place to increase the density and pressure of the innermost region, giving rise to the cooling flow. A cooling flow is thus essentially pressure driven. The gas continues to cool as it flows inwards until the adiabatic compression of the inflowing gas counterbalances the radiative loss. This scenario describes a gas which has an unique temperature and density profile at each radial distances from the cluster center. But it has been seen that the gas is inhomogeneous. However, homogeneous flows are still a good approximation and we will follow homogeneous cooling flow models. This implies

1) There is a single temperature and density at each r, and

2) The gas density rises inwards and gas temperature drops so that approximate pressure equilibrium exists.

However, this simplistic picture cannot explain all the observations of the cooling flows and one has to consider an inhomogeneous multi phase models[135, 136]. The mass deposition rate, $\dot{M}$, due to cooling (i.e. the accretion rate, although this is a poor term since most of the gas does not flow in far from r_{cool}) can be estimated from the X-ray images by using the luminosity associated with the cooling region (i.e. L_{cool} within r_{cool}) and assuming that it is all due to the radiation of the thermal energy of the gas, plus the PdV work done on the gas as it enters r_{cool},

$$L_{cool} = \frac{5}{2}\frac{\dot{M}}{\mu m}k_B T \tag{3.65}$$

where T is the temperature of the gas at r_{cool}. L_{cool} is similar to the central excess luminosity and ranges from $\sim 10^{42}$ to $> 10^{44}\text{ergs}^{-1}$ and generally represents $\sim 10\%$ of the total cluster luminosity. Values of $\dot{M} = 50 - 100\text{M}_\odot\text{yr}^{-1}$ are fairly typical for cluster cooling flows. Some clusters show $\dot{M} \sim 500\text{M}_\odot\text{yr}^{-1}$ (e.g PKS0745, A1795, A2597 and Hydra A). The main uncertainties in the determination of $\dot{M}$ lie in the gravitational contribution to L_{cool} and the appropriate choice for t_a. Assuming $t_a \sim 10^{10}\text{yr}$, the estimates of $\dot{M}$ are probably accurate to within a factor of 2. Empirically, we find that $\dot{M}$ is roughly proportional to $t_a^{\frac{1}{3}}$.

In chapter 2, we investigated the prospects to detect gas bulk velocities in clusters of galaxies through kinematic S-Z effect, which depends linearly on the velocity component along the line of sight. Bulk motion along a line of sight will contribute to the kinematic

S-Z term as long as their averaged velocity, in the observer frame, does not vanish. In the case of cooling flow bulk motion the averaged velocity, in the cluster frame, along a give line of sight vanishes in good approximation, since we assume spherical symmetric infall. Thus, the cooling flow bulk motion will not contribute as such to the kinematic S-Z effect. Indeed, the effect we consider depends quadratically on the velocity and clearly, the averaged quadratic velocity does not vanish along a line of sight in the cluster frame. The considered effect usually turns out to be small, since the cooling flow bulk velocities are rather small, unless in the very central regions of cooling flow clusters, where the cooling flow approaches a sonic radius and changes from subsonic to the supersonic regime. Nonetheless, in some favorable cases it might be of the order of some percent of the thermal S-Z effect. In the next section we will outline the dynamics of a homogeneous steady state cooling flow model in order to get the velocity profile of the bulk motion and in the last section we derive the modifications to the Kompaneets equation due to the inclusion of bulk motion of the scatters inside the cluster frame. This will then enable us either to obtain better determinations of the Hubble constant or more details on the state of the cluster.

3.10 Velocity Profiles for a Homogeneous Cooling Flow Model

We describe the bulk motion by considering a homogeneous steady state cooling flow where the mass deposition rate $\dot{M}$ is constant, negative. No mass drops out of the flow. We neglect the possible influence of magnetic fields, rotation, and viscosity. In this context, the cluster is expected to be in a relaxed state, so that hydrostatic equilibrium allows us to use as isothermal β-model. For spherically symmetry, the cooling flows can thus be described by a set of Euler equations [137, 138, 139, 140]:

$$\left. \begin{array}{l} 4\pi r^2 \rho_{CF} v = \dot{M} \\ v\frac{dv}{dr} + \frac{1}{\rho_{CF}}\frac{dP}{dr} + \frac{G\mathcal{M}(r)}{r^2} = 0 \\ v\frac{dE}{dr} - \frac{Pv}{\rho_{CF}^2}\frac{d\rho_{CF}}{dr} = -\Lambda\rho_{CF} \end{array} \right\}, \tag{3.66}$$

Where ρ_{CF} and $P(r)$ are the gas density and pressure, respectively, in the cooling flow and $v(r) < 0$ is the velocity of the inward directed cooling flow. $\mathcal{M}(r)$ is the gravitational cluster mass inside the radius r and is the sum of baryons and dark matter (Eq. 3.38).

However, we assume baryonic contribution to the total mass negligible as compared to dark matter contribution. The internal energy is $E(r) = \frac{3}{2}\theta(r)$, with the temperature parameter θ which defines the square of the isothermal sound speed c_s:

$$\theta(r) = c_S^2(r) = \frac{k_B T_{e,CF}(r)}{\mu m_p}, \tag{3.67}$$

where $\mu \approx 0.63$ is the mean molecular weight, m_p the mass of proton and $T_{e,CF}$ the electron temperature in the cooling flow and $\Lambda(\theta)$ is a cooling function, which is defined so that $\Lambda \rho_{CF}^2$ is the cooling rate per unite volume. We will use an analytical fit to the optically thin cooling function as given by [141, 142]:

$$\frac{\Lambda(\theta)}{10^{-22}\text{erg cm}^3\ \text{s}^{-1}} = 4.7 \times \left[-\left(\frac{T}{3.5 \times 10^5\text{K}}\right)^{4.5}\right]$$
$$+0.313 \times T^{0.08} \times \exp\left[\left(-\frac{T}{3.0 \times 10^6\text{K}}\right)^{4.4}\right]$$
$$+6.42 \times T^{-0.2}\exp\left[\left(-\frac{T}{2.1 \times 10^7\text{K}}\right)^{4.0}\right]$$
$$+0.000439 \times T^{0.35}. \tag{3.68}$$

This fit is accurate to within 4% for a plasma with solar metallicity $10^5\text{K} \leq T \leq 10^8\text{K}$. For $10^8\text{K} \leq T \leq 10^9\text{K}$, it underestimate cooling by a factor of the order of unity and therefore is a conservative fit as far as the effect of cooling is concerned.

Upon Eliminating the density ρ_{CF} in Eq. (3.66) the two differential equations can be put in a form suitable for numerical integration [137]:

$$\left.\begin{array}{l} \frac{dv}{dr} = v\frac{\left[3G\mathcal{M}-10r\theta+\frac{\dot{M}}{2\pi}\frac{\Lambda(\theta)}{\mathcal{M}^2 v^2}\right]}{[r^2(5\theta-3v^2)]} \\[2mm] \frac{d\theta}{dr} = 2\frac{\left[\theta(2v^2r-G\mathcal{M})-(v^2-\theta)\frac{\dot{M}}{4\pi}\frac{\Lambda(\theta)}{\mathcal{M}^2 v^2}\right]}{[r^2(5\theta-3v^2)]} \end{array}\right\} \tag{3.69}$$

These equations have singularities at the sonic radius r_s, where $5\theta_s = 3v_s$. A necessary condition of singularity is that the numerators of Eq. (3.69) vanish at the sonic radius. Therefore

$$r_s = \frac{3}{10\theta_s}\left[G\mathcal{M}(r) + \frac{\dot{M}\Lambda(\theta_s)}{10\pi\theta_s\mathcal{M}^2}\right]. \tag{3.70}$$

To integrate Eq. (3.69) we have to take into account that both equations have singularities
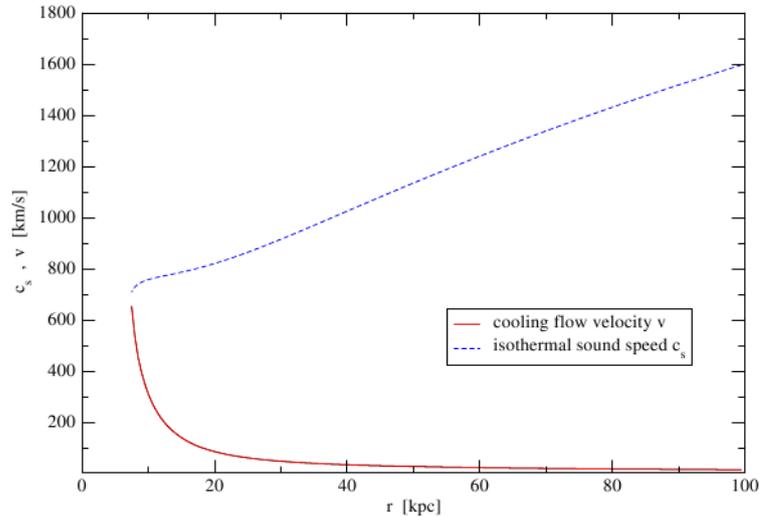
and

Figure 3.5: Cooling flow velocity $|v(r)|$ and isothermal sound speed $c_s(r)$ as a function of radius. The mass deposition rate is $\dot{M} = 300\text{M}_\odot\text{yr}^{-1}$, $r_{cool} = 100\text{Kpc}$. The initial values for the integration are $v(r_{cool}) = 15\text{km/s}$ and $c_s(r_{cool}) = 1600\text{km/s}$ [142] .

at the sonic radius r_s and where the cooling flow undergoes a trans-sonic transition. The cooling flow region is limited by cooling radius $r_{cool} \approx 100\text{Kpc}-150\text{Kpc}$.

We stress that our goal is not to develop a sophisticated cooling flow model, but to get an idea of how the cooling flow bulk motion contributes to S-Z effect. We therefore, do not attempt to find solutions of Eq. (3.69) for the innermost supersonic region, $r < r_s$, where we expect shocks to be important. We then avoid the search of critical values at r_s which would have to be matched by hydrostatic equilibrium at r_{cool}. We thus start our integration from r_{cool} towards r_s we stop when Mach number, $m = \frac{v}{c_s}$ is close to unity, $m \approx 0.9$. Reasonable initial values at r_{cool} are: $v(r_{cool}) \approx v_T \approx 10\text{kms}^{-1} - 20\text{kms}^{-1}$, where v_T is the turbulent velocity and $\theta(r_{cool})$ such that $t_{cool} = \frac{5}{2}\frac{\theta}{\rho_{CF}\Lambda} \leq t_H$. In Fig. (3.5) we have plotted the velocity $|v(r)|$ and the isothermal sound speed $c_s(r)$ as a function of of the radius r. This figure illustrates clearly that the electrons are strongly accelerated in the cluster center. Fig. (3.6) shows the corresponding electron density profile $f_{e,CF}$ in the cooling flow region.
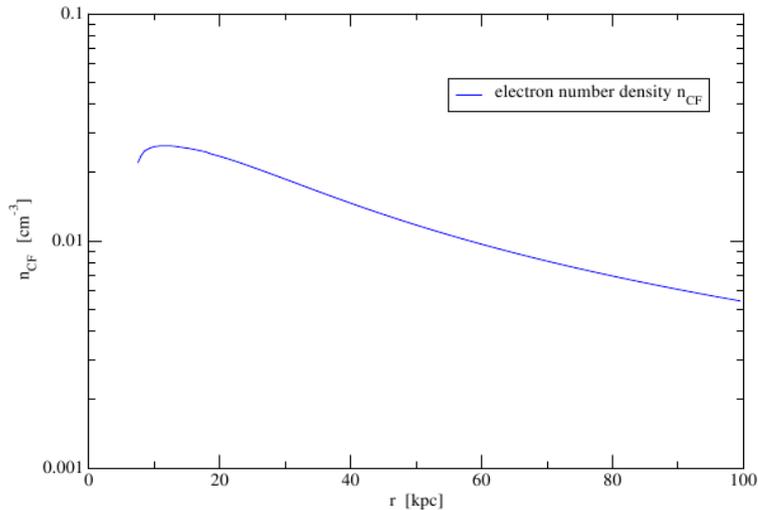
Figure 3.6: Cooling flow electron number density $n_{CF}(r)$ as a function of radius. Cooling flow parameters as adopted in Fig. (3.5) [142].

3.11 S-Z Effect with Cooling Flow Bulk Motion

The frequency dependent intensity change of the CMBR photon field $\Delta I_K(x)$ after integration along the line of sight over the cluster (cl) dimension is expressed as (see Eq. (2.35)):

$$\Delta I_K(x) = I_0 g(x) \int_{cl} \frac{k_B T_{e,cl}}{m_e c^2} \sigma_t f_{cl} dl_{cl}, \tag{3.71}$$

where the symbols have their usual meanings.

The Kompaneets equation used describes a static scatterer, assuming that in the average the electrons are macroscopically at rest. This is no longer true for the electrons in an accelerated cooling flow, as is described by the system of Eqs. (3.69). The Kompaneets equation has thus to be modified in such a way, that the (macroscopic) bulk velocity of the moving electron media is explicitly taken into account.

Psaltis & Lamb [143] gave a very detailed analysis of the Compton scattering by static and moving media. They made a careful distinction between the electron rest frame, the fluid frame (comoving with the fluid) and the system frame. Starting from the Boltzmann equation in the system frame, introducing the proper Lorentz transformation expanding to the appropriate orders and assuming that the velocity distribution in the fluid frame is a relativistic Maxwellian, They end up with the Zeroth moment of the radiative

transfer equation, with the emission and absorption included.

Under the condition that the radiation filed (CMBR) is isotropic in the system frame, and introducing the macroscopic electron bulk velocity $v(r)$, the extended Kompaneets equation becomes:

$$\frac{1}{n_e\sigma_t c}\frac{\partial I}{\partial t} = \frac{\epsilon}{m_e c^2}\frac{\partial}{\partial \epsilon}(\epsilon I) + \left(\frac{k_B T_{e,cl}}{m_e c^2} + \frac{v^2}{3c^2}\right)\left[-4\epsilon\frac{\partial I}{\partial \epsilon} + \epsilon\frac{\partial^2}{\partial \epsilon^2}(\epsilon I)\right], \qquad (3.72)$$

where we neglected absorption, emission and induced scattering. ϵ is the photon energy.

For CMBR photons we have $\epsilon \ll k_B T_{e,cl} + \frac{1}{3}m_e v^2$. Thus, the above equation becomes:

$$\frac{1}{n_e\sigma_t c}\frac{\partial I}{\partial t} = \left(\frac{k_B T_{e,cl}}{m_e c^2} + \frac{v^2}{3c^2}\right)\left[-2\epsilon\frac{\partial I}{\partial \epsilon} + \epsilon^2\frac{\partial^2 I}{\partial \epsilon^2}\right] \qquad (3.73)$$

Eq. (3.73) shows that if the radiation field is isotropic in the system frame, Comptonization of the bulk motion of the electrons inside the cluster is described entirely by second order terms in v, since all first order terms in v vanish identically. The effect is clearly different from the kinematic S-Z effect, where the cluster as a whole moves through the CMBR radiation. This equation of course reduces to the standard Kompaneets equation for $v = 0$. Thus the important point is that the effect of a non-zero velocity field gives an additive contribution to the standard thermal S-Z effect.

This way we can express the bulk motion contribution due to the cooling flow (CF) to the S-Z effect as follows:

$$\frac{\partial I}{\partial t} = \left(\frac{\partial I}{\partial t}\right)_K + \left(\frac{\partial I}{\partial t}\right)_{CF}, \qquad (3.74)$$

where the first term on the right hand side is given by the standard Kompaneets equation and the second term is due to the moving electron media in the cooling flow.

Relating the CMBR photon intensity field I to the occupation number n through $I = I_0 x^3 n$, we have,

$$\left(\frac{\partial I}{\partial t}\right)_{CF} = \left[-4x\frac{\partial}{\partial x}(x^3 n) + x\frac{\partial^2}{\partial x^2}(x^4 n)\right] I_0 \frac{\sigma_t n_{CF} v^2}{3c}, \qquad (3.75)$$

where n_{CF} is the electron number density in the cooling flows region. Integrating over

the cluster cooling flow region and assuming a Planckian photon field for n, we find:

$$\Delta I_{CF}(x) = I_0 g(x)\frac{1}{c^2}\int_{CF} n_{CF}(r)\sigma_t \frac{v^2(r)}{3}dl_{CF}, \qquad (3.76)$$

which is the contribution due to the cooling flow bulk motion inside the cluster frame to the S-Z effect. we see that the spectral shape $g(x)$ of this additional term is the same as for the usual thermal S-Z effect. This clearly makes it more difficult to distinguish this contribution from usual S-Z effect.

The cooling flow bulk motion contribution to the S-Z effect can reach for some clusters the percent level and become relevant for a correct analysis of the S-Z observations. Especially in view of the rapid progress in the observational techniques - which will provide in the near future much more accurate measurements - one might then be capable of observing also small deviations from the standard thermal S-Z-effect. This will then enable observers either to obtain better determinations of the Hubble constant or more details on the state of the cluster.

3.12 Summary

In this chapter, we discussed a joint analysis of Sunyaev-Zel'dovich effect and X-ray emission from clusters. Taking the advantage of the different dependence on n_e, S-Z effect and X-ray observations can be combined to determine the clusters cosmology. This analysis generally assumed the cluster gas to be spherical, unclumped and isothermal. With the X-ray emission, we modeled different structures of the intracluster medium. We used isothermal β-model for our analysis. It provides a good fit to observed cluster profiles in the intermediate range $100\text{Kpc} \leq r \leq 1\text{Mpc}$, and this range often contains enough information so that fitting the β-model to the data still provide the useful information. We then looked at the novel method of estimating the angular diameter distance and core radius of the galaxy clusters using radio observations of S-Z effect coupled with X-ray observations. These cluster distances can be combined with redshift measurements to determine the value of Hubble constant. The effects of asphericity on the estimate of the Hubble constant was also deduced by assuming that the atmosphere is prolate or oblate. We briefly reviewed some recent results obtained from the joint analysis. We also discussed number of sources of uncertainties in the estimated value of the Hubble constant and its effect on the determination of it. In particular, it was found that isothermality,

clumpiness and host of other effects can give rise to either over or under estimation of the Hubble constant. However accuracy in both systematic or statistical uncertainties will improve drastically in the near future leading to more exact measurements. Finally, we outlined the dynamics of homogeneous steady state cooling flow model in order to get the velocity profile of the bulk motion. It is found that the cooling flow bulk motion contribution to the S-Z effect can reach for some clusters to a appreciable level and can give correct analysis of the S-Z observations with cooling flows which will enable us to obtain better determination of cluster morphology.

Chapter 4

Constraining Cosmological Parameters from Sunyaev-Zel'dovich Effect

4.1 Introduction

With the rapid development of observing techniques, the Sunyaev-Zel'dovich effect has become one of the most powerful tools for the detections of high redshift clusters and cosmic microwave background anisotropy on small scales. Indeed, the redshift-independence is the major advantage of non-targeted S-Z surveys over traditional optical and X-ray observations. This arises from the fact that the S-Z effect depends uniquely on the intrinsic properties of the warm-hot gas associated with cosmic structures, while the photons interacting with the gas come from CMBR at very high redshift z $\approx$ 1000. Because robust constraints on cosmological models are provided by the most massive and distant clusters, growing interest over the past years has been focused upon how well the fundamental cosmological parameters can be constrained with non-targeted S-Z cluster surveys [144] and S-Z power spectrum [145]. The sensitivity of the expected S-Z cluster counts and S-Z power spectrum to the underlying cosmological model is quite impressive.

When the electron temperature T_e is much higher than the temperature T_γ of the CMBR photons, the CMBR flux change due to the presence of a cluster can be written as

$$
\begin{aligned}
S_\nu(x) &= S_\nu^\gamma Q(x) Y \\
&\propto M_e < T_e >,
\end{aligned}
\tag{4.1}
$$

where $S_\nu^\gamma = \frac{2h\nu^3}{c^2} \frac{1}{(e^x-1)}$ is the unperturbed CMBR flux,

$$Q(x) = \frac{xe^x}{e^x - 1} \left[\frac{x}{\tanh(\frac{x}{2})} - 4 \right] \tag{4.2}$$

and integrated Compton y parameter,

$$
\begin{aligned}
Y &= \int y d\Omega \\
&= D_a^{-2} \int y dA,
\end{aligned}
\tag{4.3}
$$

where D_a is the angular diameter distance and integration is over the projected area. It is clear from Eq. (4.1) that the net S-Z effect depends only on the total mass of a cluster gas and a density-weighted mean temperature. This means that for unresolved clusters the S-Z flux is insensitive to the spatial distribution of the ICM or its temperature structure. The S-Z flux density from a cluster diminishes as a square of its angular diameter distance. Since angular diameter distance of objects at cosmological distances, $z > 1$, saturates to a limiting value or even decreases with increasing redshift, the S-Z flux from the clusters does not rapidly diminish with increase in cosmological distance (see Fig. (3.2)). Therefore, one expects an S-Z survey to detect all clusters above some mass threshold with little dependence on redshift through angular diameter distance. Together with the Press- Schechter [146, 147] formalism for the abundance of dark halos at different cosmic epoch, we can eventually compare the theoritical S-Z counts and power spectra with the observed one and demonstrate the constraints in the determination of the cosmological parameters. The inability of cosmological models to provide the same amplitudes and scales of the observed functions can therefore be a strong argument against the model itself.

Apart from S-Z number counts, the power spectrum of the S-Z effect can also be used as a probe of cosmology analogous to that from primary anisotropies. The thermal S-Z power spectrum is fairly flat, with a broad peak at $l \approx 2000$, were it begins to dominate over the primary CMBR. The shape of the kinetic S-Z power spectrum is similar to the thermal one but the amplitude is about 30 times smaller. Because S-Z effect has a generic non-Gaussian temperature distribution, it could be detected in the sky by estimators sensitive to skewed variance [148]. Many other secondary contributors to the temperature anisotropy have a Gaussian distribution in amplitudes. Therefore, the negative-skewed nature of S-Z effect may be useful in distinguished it from other sources, foregrounds and

instrument noise. This chapter describes as to how S-Z cluster surveys and S-Z power spectrum can be used to constrain cosmological parameters like Ω_m, Ω_Λ [20, 149, 150].

4.2 Power Spectrum

Let us consider spheres of radius $R = (\frac{3M}{4\pi\rho_b})^{\frac{1}{3}}$, where ρ_b is the mean density of the Universe and M is some mass scale of interest. We also define the over density as,

$$\delta(\mathbf{x}) = \frac{\rho(\mathbf{x}) - \rho_\mathbf{b}}{\rho(\mathbf{x})}. \tag{4.4}$$

The fractional rms mass fluctuation is,

$$\sigma = \frac{\sqrt{<\delta M^2>}}{M}. \tag{4.5}$$

While studying the temperature fluctuations of the CMBR, it was useful to expand $\frac{\delta T}{T}$ in spherical harmonics. A similar decomposition of δ is also useful. Since δ is defined in three-dimensional space (rather than on the surface of sphere), a useful expansion of δ is in terms of Fourier components. Within a large comoving box, of volume V, the density fluctuation field $\delta(\mathbf{x})$ can be written as

$$\begin{aligned}
\delta(\mathbf{x}) &= \frac{1}{V} \sum_k \delta(\mathbf{k}) \exp(i\mathbf{k}.\mathbf{x}) \\
&= \frac{1}{(2\pi)^3} \int_V \delta(\mathbf{k}) \exp(i\mathbf{k}.\mathbf{x}) d^3k.
\end{aligned} \tag{4.6}$$

The Fourier coefficients $\delta(\mathbf{k})$ are complex quantities given, as it is straightforward to see, by

$$\delta(\mathbf{k}) = \int_V \delta(\mathbf{x}) \exp(-i\mathbf{k}.\mathbf{x}) d^3x. \tag{4.7}$$

Each Fourier component is a complex number, which can be written in the form,

$$\delta(\mathbf{k}) = |\delta(\mathbf{k})| \exp(i\phi_k). \tag{4.8}$$

The mean square amplitude of the Fourier components define the power spectrum:

$$P(k) = <|\delta(\mathbf{k})|^2>, \tag{4.9}$$

where the average is taken over all possible orientations of $\mathbf{k}$. Simple inflationary models predict that the initial power spectrum is a power-law, $P(k) \propto k^n$, and furthermore that $n \approx 1$ (Harrison-Zeldovich spectrum). These models do not predict the constant of proportionality, which has to be fixed by observation. The primordial power spectrum is believed to change during the evolution of the early Universe until the end of the epoch of recombination by various processes, such as growth under self-gravitation, effects of pressure and dissipative processes. The overall effect can be encapsulated in the transfer function, $T(k)$, which gives the ratio of the later-time amplitude of a mode to its initial value,

$$P(k, z) = P_0(k) \frac{D_g^2(z)}{D_g^2(z_0)},$$ (4.10)

where D_g is a linear growth of perturbations. The evolution of linear perturbations back to the surface of last scattering obeys the simple growth laws given in above equation.

If the field is Gaussian then from Eq. (4.6)

$$< \delta(\mathbf{x}) > \quad = \quad 0$$ (4.11)

$$< \delta^2(\mathbf{x}) > \quad = \quad \sigma^2 = \text{constant}.$$ (4.12)

The real and Fourier-space fluctuations may be related using Parseval's theorem,

$$\frac{1}{V} \int |\delta(\mathbf{x})|^2 d^3 x = \frac{1}{(2\pi)^3} \int |\delta(\mathbf{k})|^2 d^3 k.$$ (4.13)

Averaging both sides and using the fact σ^2 is constant, we obtain,

$$\sigma^2 = \frac{1}{(2\pi)^3} \int P(k) d^3 k.$$ (4.14)

Fourier k-space is assumed to be isotropic, so we can further simplify Eq. (4.14). For a given $|\mathbf{k}|$ the volume element of k-space is $d^3 k = 4\pi k^2 dk$ and

$$\sigma^2 = \frac{1}{2\pi^2} \int k^2 P(k) dk.$$ (4.15)

The mass function $n(M)$, also called the multiplicity function, of cosmic structures such as galaxies is defined by the relation,

$$dN = n(M) dM,$$ (4.16)

which gives the number of the structures in question per unit volume with mass contained in the interval between M and $M + dM$. Mass functions given by numerical simulations are good approximations. Yet they cover a limited volume, given by the size of the simulation box. There is an excellent analytic description, the Press-Schechter formalism [146]. It provides a simple but powerful way to calculate the number density of objects of a given mass and at any redshift. The Press-Schechter (PS) formalism and its extensions has been extensively studied and compared to numerical simulations [151, 152]. It considers the emergence of collapsed objects from a primordial Gaussian random density field.

Since the primordial density perturbations are assumed to be Gaussian fluctuations, the phases of the waves that make up the density distribution are random, and the distribution of the over-densities ρ in spheres of radius r can be described by a Gaussian function:

$$p(\delta) = \frac{1}{\sqrt{2\pi}\sigma(M)}\exp\left[\frac{-\delta^2}{2\sigma^2(M)}\right].$$ (4.17)

At a given time, the fraction of points which are surrounded by a sphere of radius r within which the mean over-density exceeds some density threshold δ_c is given by,

$$F(\delta_c, M) = \int_{\delta_c}^{\infty} \frac{1}{\sqrt{2\pi}\sigma(M)}\exp\left[\frac{-\delta^2}{2\sigma^2(M)}\right] d\delta_c.$$ (4.18)

Press and Schechter suggested that this fraction be identified with the fraction of particles which are part of a nonlinear lump with mass exceeding M. Changing variables, $u = \frac{\delta}{\sqrt{2}\sigma}$, we can express the latter equation in the form,

$$F(\delta_c, M) = \frac{1}{\sqrt{\pi}} \int_{\frac{\delta_c}{\sqrt{2}\sigma(M)}}^{\infty} e^{-u^2} du = \frac{1}{2}\text{erfc}\left(\frac{\delta_c}{\sqrt{2}\sigma(M)}\right),$$ (4.19)

where erfc is complementary error function. From above equation, we can obtain the comoving number density of halos of mass M, the Press-Schechter mass function: The fraction of the volume collapsed into objects with mass between M and $M + dM$ is given by $|\frac{dF}{dM}|dM$. Multiply this by the average number density of such objects $\frac{\rho_b}{M}$ to get the

comoving number density of collapsed objects between M and $M + dM$,

$$
\begin{aligned}
n(M, z)dM &= 2\frac{\rho_b}{M}\left|\frac{dF}{dM}\right|dM \\
&= \sqrt{\frac{2}{\pi}}\frac{\rho_b}{M^2}\nu_c\left|\frac{d\ln\sigma(M, z)}{d\ln M}\right|e^{-\frac{\nu_c^2}{2}}dM,
\end{aligned}
\tag{4.20}
$$

where

$$
\nu_c(M, z) = \frac{\delta_c}{\sigma(M, z)}.
\tag{4.21}
$$

The factor 2 was inserted in order to account for the matter in under-dense regions, which also eventually falls into over-dense ones. In order to estimate the mass function from the Press-Schechter formalism, we need to specify $\sigma(M, z)$ and δ_c. We can express the variance of the density fluctuations when smoothed with the spherically symmetric window function $W(k, R)$ of characteristic co-moving R in terms of the power spectrum $P(k, z)$ of the linear density field:

$$
\sigma^2 = \frac{1}{2\pi^2}\int k^2 P(k)|\widetilde{W}(k, R)|^2 dk,
\tag{4.22}
$$

where $\widetilde{W}(k, R)$ is a Fourier transform of the corresponding real space window function. A spherical top-hat form with radius R is usually adopted for the window function and this corresponds to a Fourier-space window function,

$$
\widetilde{W}(k, R) = \frac{3}{(kR)^3}\left[\sin(kR) - (kR)\cos(kR)\right].
\tag{4.23}
$$

The value of δ_c has a weak dependence on Ω_m. In a universe with $\Omega_m = 1$, $\delta_c = 1.68$. It has been seen that δ_c varies at most $\sim 4\%$ for a range of Ω_m from 0.1 to 1 [152]. Therefore, we can adopt a constant value 1.68 for δ_c. The Press-Schechter formalism along with the COBE normalized $P(k)$ have been used to calculate the number densities of collapsed objects. We choose to identify the condensates as cluster of galaxies and try to compute their abundances as a function of cluster mass and redshift for different set of cosmological parameters.

4.3 Cosmological Parameters from Future S-Z Cluster Surveys

Tapping the cosmological potential of galaxy cluster requires large, homogeneous cluster catalogs extending to redshifts greater than unity. The strongest constrain on dark energy, for example, will come from the observed around $z = 1$ and beyond. Today there are only of the order of 10 clusters with spectroscopically conformed redshift $z > 1$. The need for a deeper and larger catalogs motivates a number of substantial observational efforts in different wavebands.

We may search for clusters in variety of ways:

1) By their gravitational lensing of background galaxy images. With a large imaging survey, we could search for clusters through their lensing signal.

2) By X-ray emission from their intra-cluster medium. Cluster surveys and observations in the X-ray band with satellites like ROSAT, Chandra and XMM have significantly advanced our understanding of clusters and their evolution and have played an important role in establishing cosmological models.

3) By the S-Z effect via Inverse Compton scattering.

Each of these techniques has its own advantages and disadvantages. To appreciate them we should situate clusters in the standard theoretical framework that describes them as a single, massive dark matter halos containing hot gas and galaxies with their sub halos. Dominated by dark matter and its gravitational evolution, clusters are fundamentally described by their halo mass and redshift. When building a cluster catalogs, therefore, one should quantify its properties in terms of these basic parameters in order for proper comparison to theory. Specifically, we must accurately calculate the survey selection function and determine the observable-mass relation, or for short, survey calibration.

Our focus here is on the method based on the S-Z effect, which possesses a number of advantageous properties for a cluster surveying. As for X-ray observational surveys, S-Z surveys selects clusters based on their ICM and like lensing surveys, S-Z surveys tend to suffer from projection effects, since S-Z signal is proportional to the projected mass density. A number of planned S-Z surveys have heightened anticipations as they prepare to observe large areas of sky over next few years. We assume that the co-moving number density $(\frac{dn}{dM})dM$ of clusters at redshift z with mass $M\frac{dM}{2}$ is given by the Eq. (4.20). The
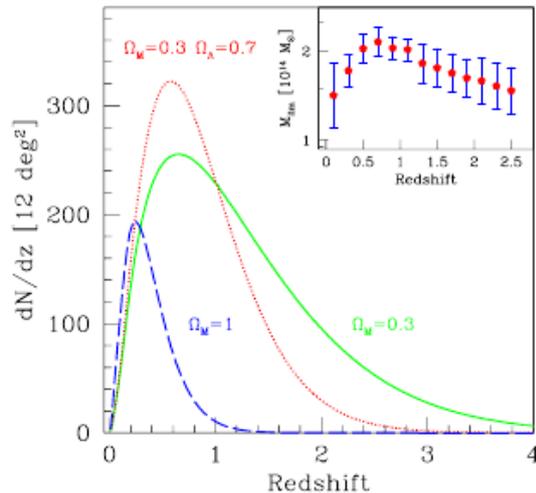
Figure 4.1: The cluster redshift distribution of S-Z effect. All curves are normalized to produce the observed local abundance of massive clusters. The redshift distribution is sensitive to cosmological parameters. Note the inset, which shows the limiting mass of clusters [153].

directly observable quantity, i.e. the average number of clusters with mass above M_{min} at redshift $z\frac{dz}{2}$ observed in a solid angle $d\Omega$ is then simply given by,

$$\frac{dN(z)}{dzd\Omega} = \left[\frac{dV(z)}{dzd\Omega}\int_{M_{min}(z)}^{\infty}\left(\frac{dn}{dM}\right)dM\right]. \tag{4.24}$$

In Fig. (4.1) we have shown the expected cluster counts for different cosmology. To calculate the expected number of clusters per square degree as a function of redshift one must consider several elements: the co-moving volume per unit redshift and unit solid angle, $\frac{dV}{dzd\Omega}$, cluster abundance (co-moving number density of halos) and the minimum observable mass as a function of redshift and cosmology, $n(>M_{lim},z)$. The cosmological sensitivity thus comes from three elements [153].

1) **Volume**: The volume per unit solid angle and redshift depends sensitively on cosmological parameters (i.e. higher Ω_Λ, or lower Ω_m increases the volume per solid angle). Left panel of Fig. (4.2) is a plot of the comoving volume element ($\frac{dV(z)}{dzd\Omega}$) versus redshift for three cosmological models. Note the rapid increase in the volume element at modest redshift, which is responsible for the rapid rise in the cluster redshift distribution in Fig. (4.1). At higher redshift, the comoving volume element flattens out and eventually turns

over. The cosmological sensitivity of the distance-redshift and volume-redshift relation derives essentially from the expansion history of the universe $E(z)$.

2) **Number density**: The number density of clusters at a given redshift depends sensitively on the growth rate of density perturbations. This growth rate is highly sensitive to cosmology (i.e. higher Ω_m speeds the growth of density perturbations so that clusters disappear more quickly as we probe to higher redshift). Right panel of Fig. (4.2) is a plot of the comoving abundance of clusters above a fixed mass, where the abundance is normalized to reproduce the observed local abundance of massive clusters. Note that abundance differences increase dramatically with redshift and are responsible for the high redshift ($z > 1$) behavior of the cluster redshift distribution (see Fig. (4.1)). Within the linear regime, the differential equation that describes growth depends, again, on the expansion history of the universe $E(z)$.

3) **Mass limit**: The mass of a cluster, which is just luminous enough to appear above the detection threshold, typically depends on the luminosity or angular diameter distance as well as the evolution of cluster structure both are sensitive to cosmological parameters. The survey yield and redshift distributions are both sensitive to the limiting mass, as indicated in Fig. (4.3). Fig. (4.3) shows the cluster redshift distribution in a fiducial cosmology for a limiting mass of $M = 2 \times 10^{14} \mathrm{M_\odot}$, and for limiting masses 10% above and below this value.

The total S-Z flux equation given in Eq. (4.1) tells us that a flux limited survey will have a cluster selection function that is proportional to $T_e N_e / D_a^2(z)$. The angular diameter distance relation is quite flat with redshift. Both T_e and N_e are determined by the cluster mass; in virial equilibrium the cluster mass sets the velocity dispersion, and hence the temperature, of the cluster gas. Taken together this implies that the selection function for a flux limited S-Z survey should be almost independent of redshift with cluster mass being the limiting factor and the limiting mass for an upcoming interferometric S-Z survey is expected to vary with redshift by less than a factor of $2 - 3$ for $z > 0.5$ [154] (if there is no cluster evolution); independent of the underlying cosmology.

The number and redshifts distribution of galaxy clusters in future deep cluster surveys can thus place strong constraints on the matter density, Ω_m, the vacuum energy density, Ω_Λ, and the normalization of the matter power spectrum, $\sigma(M)$ [154, 155, 156, 157, 158]. The important being that the degeneracies between these parameters are different from those in studies of either highredshift type Ia Supernovae (SNe), or cosmic
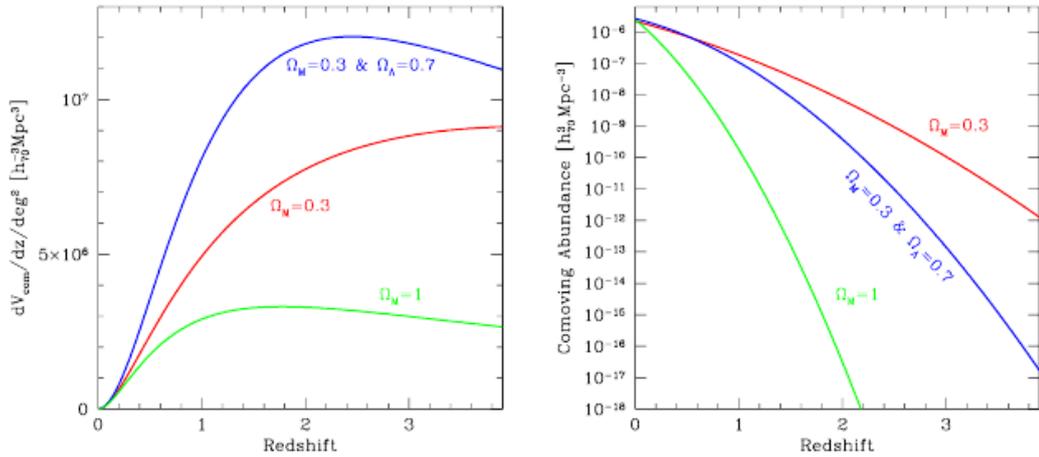
Figure 4.2: The comoving volume element (left) and cluster abundance above a fixed mass (right) in three different cosmological models. The abundances are normalized to produce the observed local abundance of massive clusters. Differences in the cluster redshift distribution are dominated by volume at low redshift and by abundance at high redshift [153].
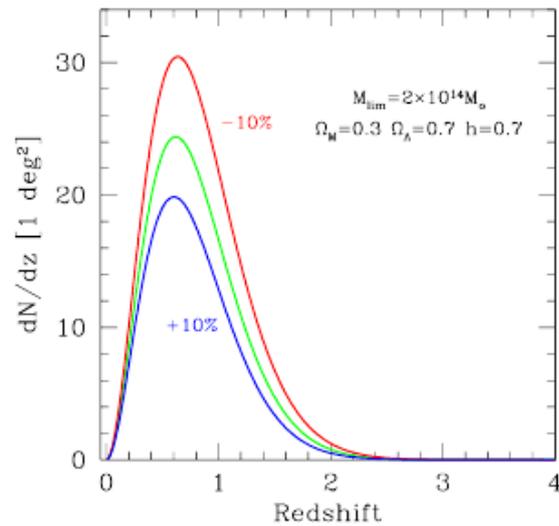

Figure 4.3: The cluster redshift distribution within a fiducial cosmological model for a mass limit of $M = 2 \times 10^{14} M_\odot$ and for mass limits 10% above and below this value. The mass sensitivity of the survey yields and redshift distributions means that accurate cosmological constraints require un- biased estimators of cluster halo mass [153].

microwave background (CMBR) anisotropies. Using a mass threshold for cluster detection expected to be typical for upcoming Sunyaev-Zel'dovich effect (S-Z) surveys, we can find that constraints on Ω_m and $\sigma(M)$ at the level of roughly 5% or better can be expected, assuming redshift information is known at least to $z \sim 0.5$ and in the absence of significant systematic errors. Without information past this redshift, Ω_Λ, is constrained to 25%. With complete redshift information, deep $(M_{lim} \sim 10^{14} h^1 M_\odot)$, relatively small solid angle $(\sim 12 \text{deg}^2)$ surveys, can further constrain Ω_Λ, to an accuracy of $\sim 15\%$, while large solid angle surveys with ground- based, large-format bolometer arrays could measure Ω_Λ, to a precision of $\sim 4\%$ or better [150]. Cluster surveys conducted in X-ray and optical are usually limited in depth to $z \sim 1$. However, the forthcoming Surveys should detect many X-ray clusters out to $z \sim 2$. As daunting of a task as extracting cosmological parameters from X-ray and optical surveys may appear to be, it is important to stress that unlike future large-scale S-Z surveys, optical and X-ray surveys have actually been conducted e.g. ROSAT All-Sky Survey (RASS), Einstein Extended Medium Sensitivity Survey (EMSS), and Sloan Digital Sky Survey (SDSS) and have been used to place strong constraints on $\sigma(M)$ and Ω_m [159, 160, 161, 162, 163].

4.4 Cluster Mass and Thermal Energy Constraints from S-Z Observations

The Compton y-parameter defined for thermal S-Z effect is given by

$$y = \frac{k_B T_e}{m_e c^2} \int \sigma_t n_e(r) dl, \tag{4.25}$$

if we assume that ideal gas law $P_e = n_e k_B T_e$ in the above equation to relate electron pressure P_e to electron number density n_e and temperature T_e, then

$$y = \frac{\sigma_t}{m_e c^2} \int P_e dl. \tag{4.26}$$

From Eq. (4.26), one can see that resolved observations of the thermal S-Z effect from a cluster can be used to constrain its electron pressure profile $P_e(r)$. This can be related to the total pressure as $P_{gas} = (1 + \frac{1}{\mu_e})P_e$, where $\mu_e = \frac{2}{(1+X)}$ is the mean particle weight per electron and X is the mass fraction of hydrogen. While deep X-ray observations have shown that the distribution of heavy elements in the ICM varies with radius [164, 165]

and theoretical studies indicate that helium sedimentation into the cluster core will also impact μ_e [166, 167] we make the simplifying assumption that $\mu_e = 1.17$.

For spherically symmetric electron pressure profile $P_e(r)$, the integrated version of y is [168]

$$
\begin{aligned}
Y_{sph} &= \frac{\sigma_t}{m_e c^2} \int_0^r P_e(r') 4\pi r'^2 dr' \\
&= \frac{\sigma_t}{\left(1 + \frac{1}{\mu_e}\right) m_e c^2} \int_0^r P_{gas}(r') 4\pi r'^2 dr' \\
&= \frac{\sigma_t E_{th}(r)}{\left(1 + \frac{1}{\mu_e}\right) m_e c^2}.
\end{aligned}
\tag{4.27}
$$

We have used the fact the in above equation that the thermal energy with in r is

$$
E_{th} = \frac{3}{2} \int_0^r P_{gas}(r') 4\pi r'^2 dr',
\tag{4.28}
$$

for a mono-atomic ideal gas.

Through Eq. (4.27), one can see that the S-Z observable Y_{sph} relates directly to the thermal energy content of the cluster. To the extent that a cluster is virialized and supported by thermal pressure, this quantity will closely track the gravitational energy $U_g(r)$ via the virial relation,

$$
2E_{th}(r) - 3P(r)V = -U_g(r).
\tag{4.29}
$$

The $-3PV$ term, where $V = \frac{4\pi r^3}{3}$ is the volume at r, accounts for the non-vanishing surface pressure and must be taken into account when solving for the mass. This term works to reduce the amount of gravitating mass required to hold the gas within r. Using Eq. (4.28), which derives from statistical mechanics, to relate pressure to thermal energy, we note that the virial relation (Eq. (4.29)) is derived from the equation of hydrostatic equilibrium [169, 170],

$$
\frac{dP_{gas}}{dr} = -\rho_{gas}(r) \frac{GM_{tot}}{r^2}.
\tag{4.30}
$$

Adopting the NFW profile to describe the total mass distribution (i.e baryonic + dark matter distribution)

$$
\rho_{tot}(r) = \frac{\rho_0}{\left(\frac{r}{r_s}\right)\left(1 + \frac{r}{r_s}\right)^2},
\tag{4.31}
$$

the total mass within the radius r is

$$
\begin{aligned}
M_{tot}(r) &= \int_o^r \rho_{tot}(r')4\pi r'^2 dr \\
&= 4\pi\rho_0 r_s^3 \left[\ln(1+\frac{r}{r_s}) - \left(1+\frac{r_s}{r}\right)^{-1}\right],
\end{aligned} \tag{4.32}
$$

here ρ_0 and r_s are respectively the normalization and scale radius of the NFW profile. The use of an NFW profile is empirically motivated by simulations of dark matter halos, and we note that other mass profile could be assumed and may in fact provide better alternatives. More recent theoretical studies, for instance, have indicated that the presence of baryons can significantly modify the mass distribution of dark matter [171, 172].

The gas mass M_{gas} and total mass M_{tot} can be related by defining the gas fraction $f_{gas} = \frac{M_{gas}(r)}{M_{tot}(r)}$, which could be a function of M_{tot}, r, z, and cluster merger history. While recently shown to be poor approximation, we make the simplifying assumption that $f_{gas}(r)$ is a constant. Detailed measurements of $f_{gas}(r)$ typically require high significance X-ray data, which are often insufficient or entirely lacking for clusters discovered via the S-Z effect. The assumption of constant $f_{gas}(r)$ implies that

$$
\rho_{gas}(r) = f_{gas}\rho_{tot}(r). \tag{4.33}
$$

Using Eqs. (4.31), (4.32) & (4.33) to solve for the gravitational potential energy, we find [173],

$$
U_g = (4\pi\rho_0 r_s^2)^2 G f_{gas} \left[\frac{r_s}{2(1+\frac{r_s}{r})^2} - \int_0^r \frac{\ln(1+\frac{r}{r_s})}{(1+\frac{r}{r_s})}\right], \tag{4.34}
$$

where we have used the fact that the differential element of gravitational energy for a spherical shell of gas with density $\rho_{gas}(r)$ is $dU_g(r) = -\frac{GM_{tot}dm}{r}$, where the mass of gas shell is $dm = 4\pi\rho_{gas}(r)r^2 dr$.

Combining Eqs. (4.27) & (4.24) through Eq. (4.29), we have,

$$
\frac{3(1+\frac{1}{\mu_e})m_e c^2 Y_{sph}(r)}{16\pi^2 G f_{gas}\sigma_t} = (\rho_0 r_s^2)^2 \left[-\frac{r_s}{2(1+\frac{r_s}{r})^2} + \int_0^r \frac{\ln(1+\frac{r}{r_s})}{(1+\frac{r}{r_s})}\right] \tag{4.35}
$$

Through this method one can find the best fit for NFW profile parameters ρ_0 and r_s, for any observationally constrained $Y_{sph}(r)$.

Here, we showed a method of mass determination from S-Z effect observations, ap-

plicable in the absence of X-ray or lensing data. This method relies on the virial relation and a minimal set of assumptions, following an approach analogous to that used for stellar structure. By exploiting the virial relation, we implicitly incorporate an additional constraint from thermodynamics that is not used in deriving the equation of hydrostatic equilibrium. This allows us to relate cluster total mass directly to the robustly-determined quantity, the integrated S-Z flux.

4.5   S-Z power spectrum

The anisotropy in the CMBR induced by clusters has been extensively explored since it was first modeled by Rephaeli [174] in the context of a simple model for IC gas evolution, reflecting increased realization of its significance on arc-minute scales. Since this anisotropy arises from the scattering of the CMBR in the evolving population of clusters, its power spectrum and cluster (S-Z) number counts can potentially yield important information on the properties of IC gas, the cluster mass function, cosmological evolution of clusters and their gaseous contents, as well as some of the global cosmological and large scale parameters. Clearly, therefore, a quantitative description of this anisotropy entails the added need (when compared with a calculation of the primary CMBR anisotropy) of modeling gas properties across the evolving population of clusters.

The usual approach to the calculation of the S-Z anisotropy is based on the Press-Schechter model for the cluster mass function, $n(M, z)$, the comoving density of clusters of mass M at redshift z. Following collapse and virialization, IC gas is presumed to have reached hydrostatic equilibrium at the virial temperature, with a density distribution that is commonly assumed to have an isothermal $\beta-$profile. The mass function is normalized by specifying the mass variance on a scale of 8 Mpch^{-1}, σ_8, a parameter that is determined from the observed X-ray temperature function by using a mass-temperature calibration. The calibration of course is limited to clusters at small redshifts. The cluster induced anisotropy has been studied at an increasingly greater degree of sophistication and detail and in wide range of cosmological and dark matter models beginning about two decade ago [175, 176]. In particular, Colafrancesco et al. [177] calculated the temperature anisotropy in a flat CDM model including gas evolution (based on results from the Einstein Medium Sensitivity Survey (EMSS)). They later extended the work to other cosmological models and estimated also that many thousands of clusters are expected to be detected during the planned Planck survey [178]. S-Z maps and power spectra can also

be generated directly from hydrodynamical simulation [179]. The range of cosmological models was extended to include currently viable ΛCDM models [180, 181, 182].

The fluctuations in the temperature background due to the S-Z effect [183] from clusters of galaxies can be quantified in terms of correlations between the fluctuations along the line of sight separated by an angle: this gives us the angular power spectrum of S-Z effect distortions. The fluctuations of CMBR temperature produced by S-Z effect can be expressed simply by expanding the two point angular correlation function into Legendre polynomials:

$$\left\langle \frac{\Delta T}{T_{cmbr}}(n) \frac{\Delta T}{T_{cmbr}}(n+\theta) \right\rangle = \frac{1}{4\pi} \sum_l C_l P_l(\cos\theta). \tag{4.36}$$

The angular temperature power spectrum C_l can be written as the sum of two terms:

$$C_l = C_l^{(P)} + C_l^{(C)}, \tag{4.37}$$

where $C_l^{(P)}$ is the Poisson contribution and $C_l^{(C)}$ is the clustering contribution.

The power spectrum for the Poisson distribution of objects can then be written as [184],

$$C_l^{(P)} = \int_0^{z_{max}} dz \frac{dV(z)}{dz} \int_{M_{Min}}^{M_{Max}} dM \frac{dn(M,z)}{dM} |y_l(M,z)|^2, \tag{4.38}$$

where $\frac{dV(z)}{dz}$ is the differential comoving volume and $\frac{dn}{dM}$ is the number density of objects. For the number density we use the Press-Schechter formalism (Eq. (4.20)) and the volume element is given by,

$$\frac{dV(z)}{dz} = r(z)^2 \frac{4\pi c}{H_0} \left[\Omega_m (1+z)^3 (1-\Omega_m-\Lambda)(1+z)^2 + \Lambda \right]^{-\frac{1}{2}}, \tag{4.39}$$

where the comoving distance $r(z)$ is [181],

$$r_z = \begin{cases} \frac{2c}{H_0} \left[\frac{\Omega_m z + (\Omega_m-2)(\sqrt{1+\Omega_m z}-1)}{\Omega_m^2(1+z)} \right] & \Lambda = 0 \\ \frac{c}{H_0} \int_0^z dz [\Omega_m(1+z)^3 + 1 - \Omega_m]^{-\frac{1}{2}} & \Lambda = 1-\Omega_m, \end{cases} \tag{4.40}$$

and y_l is the Fourier transform of the projected Compton y parameter.

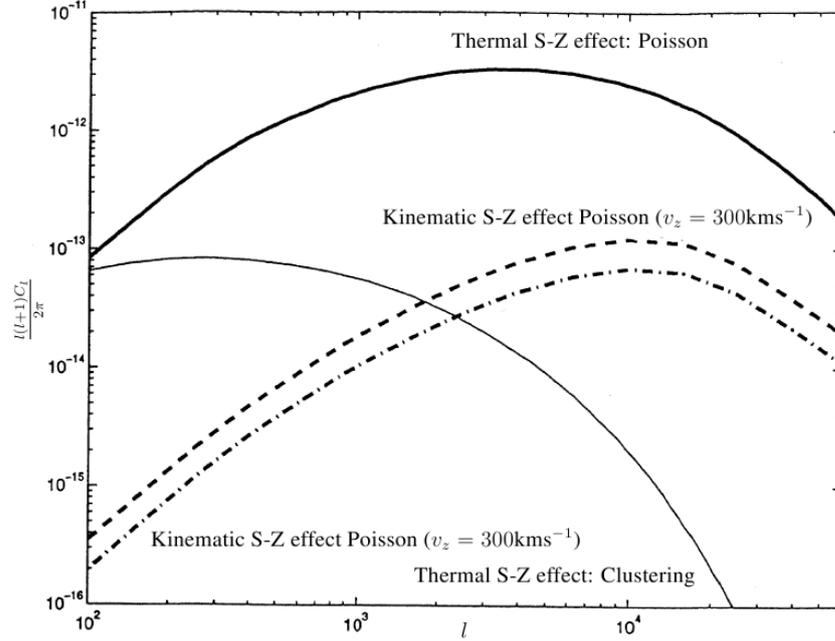The clustering power spectra depends on the line of sight passing through an ensem-

Figure 4.4: The S-Z effect Poisson power spectra (thick lines) and the clustering power spectra for galaxy clusters are shown for ΛCDM cosmology. The solid lines are for thermal S-Z effect, the dashed line is for kinematic S-Z effect with $v_z = 400 \text{kms}^{-1}$ and the dotted dashed line is for the same with $v_z = 400 \text{kms}^{-1}$. Here we have assumed $f_g = $constant [186].

ble of correlated clusters. it can be estimated as [180, 185],

$$C_l^{(C)} = \int_0^z dz \frac{dV(z)}{dz} P(k,z) \left[\int_{M_{Min}}^{M_{Max}} dM \frac{dn(M,z}{dM} b(M,z) y_l(M,z) \right]^2 , \qquad (4.41)$$

where $b(M, z)$ is the time dependent linear bias factor. The matter power spectrum $P(k, z)$, is related to the power spectrum of cluster correlation function $P_c(k, M_1, M_2, z)$ via $P_c(k, M_1, M_2, z) = b(M_2, z) b(M_2, z) D_g^2(z) P(k, z = 0)$.

In Fig. (4.4) we have plotted the Poisson as well as clustering power spectra for ΛCDM model. It is easily seen that the clustering power spectrum is much less than the Poisson case and also falls off faster as one goes to smaller angles (small beam sizes). The Poisson power spectra dominates at all l values greater than 100. So one can assume that for beams comparable to the size of the richest clusters, the Poissonian approximation is valid. The main features to be noted from this figure are:
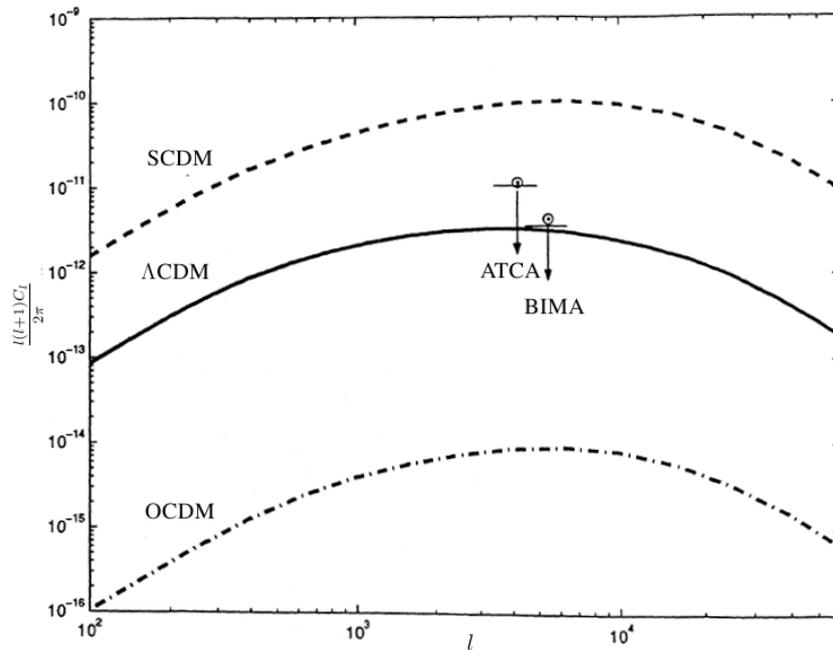
Figure 4.5: The S-Z Poisson spectra for different cosmological models are shown: ΛCDM (solid), SCDM (dashed), and OCDM (dot dashed). The observational upper limits on arc minute temperature fluctuations seen by ATCA (Australia Telescope Compact Array) and BIMA (Berkeley Illinois Maryland Array) are also shown with filled circles [50, 186].

1) The power spectrum rises and falls with l producing a peak l_{peak}, which is around 4000 for the model shown (ΛCDM with $f_g = \frac{\Omega_b}{\Omega_m}$).

2) The main contribution of S-Z effect to CMBR anisotropy occurs at $1000 \leq l \leq 20000$ after the CMBR primary anisotropy becomes negligible.

3) The amplitude of the kinematic S-Z effect is more than an order of magnitude smaller than that of the thermal S-Z spectrum.

We thus have a basic idea of the shape and size of the power spectrum of S-Z effect from galaxy clusters. In the next section we took at the nature of the power spectrum. in more details.

4.6   Nature of the Power Spectrum

As is clear from Eqs. (4.38) & (4.41), both the volume element and the abundance of clusters depend on the cosmological models. As a consequence the power spectrum will also vary with the varying cosmological parameters. This can be easily seen in Fig. (4.5). In this figure, we plot the power spectra for three different cosmological models i.e SCDM, ΛCDM and OCDM. Since the gas physics of individual clusters are not yet known with precision, so one cannot use S-Z effect to precisely determine the cosmological parameters. One can, however, use the S-Z effect to constrain cosmological parameters. The way to do this is also straight-forward and is illustrated in Fig. (4.5). In this figure, we have also marked the observational upper limits given by ATCA and BIMA [186]. The ATCA and BIMA observations put upper limit of 23μk and 14.1μK respectively at effective l of 4200 and 5470. One can immediately see that the SCDM model is ruled out and the ΛCDM is barely consistent with BIMA limits. Thus, it is difficult to have Ω_m much greater than 0.35 in a flat universe without violating observations. One has, thus, been able to constrain the cosmological matter density parameter with a power spectrum analysis of S-Z effect. Another point to be noted from Fig. (4.5) is that the peak positions are different for different cosmologies, with the peak being at the highest l for an OCDM (Open Cold Dark Matter) universe. This is easy to understand since an object would subtend a smaller angel in an open universe than in a flat one. The reason for the small differences in the peak position between SCDM (Standard Cold Dark Matter) and ΛCDM models is more subtle and depends on the exact nature of the angular-diameter relation and the distribution of objects. To understand the power spectrum in more detailed manner, let us concentrate on a particular model say ΛCDM model and see the effects of mass and redshift cutoff on the power spectrum. In Fig. (4.6) we have shown the effect of having different z_{max}, the maximum redshift up to which we assume there are clusters capable of distorting the CMBR. It is easily seen that the contribution to the distortion fro redshift beyond 3 is negligible. As one comes down in redshift, the power spectrum at high l decreases. However, the power at $l \approx 1000$ starts differing as a function of z only for $z \leq 1$. This is because lower masses are present at high redshifts and thus their contribution gets cut off when one forces $z_{max} \leq 2$, whereas the more massive clusters are present mainly below $z \approx 1$.
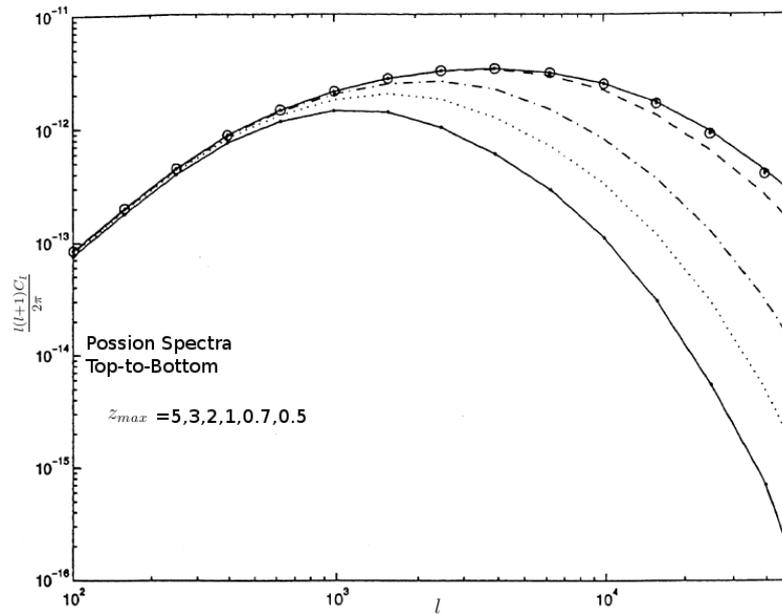
Figure 4.6: The S-Z power spectra is plotted for different maximum redshifts: from top to bottom the z_{max} are 5 (circle), 3 (thick solid line with dots), 2 (dashed line, 1 (dash dot line), 0.7 (dotted line), and 0.5 (solid line) [50, 186].

To see the effect of z_{max} more clearly, let us define the quantity C_l^* as

$$C_l^* = \frac{l(l+1)C_l/2\pi}{<y>^2} \tag{4.42}$$

We have plotted C_l^* vs l for different z_{max} in Fig. (4.7). we have seen that there is a crossover of different curves at $l \approx 7000$ above which the behavior of the different spectra are similar to that in Fig. (4.6). However, below this crossover point, the trend is reversed and C_l^* is large for lower value of z_{max}. There is also a trend in the peak positions of the individual clusters, which moves to lower l values as one lowers the values of z_{max}

In Fig. (4.8), we have shown the effect of different values of z_{max} on the clustering spectrum. compared to the Poisson case, the peak position remains almost same. this is because the clustering spectrum depends mainly on the inter-cluster distance and the major contributions to the clustering power spectrum comes from small redshifts.

At any epoch, one expects the temperature fluctuations to be dominated by very rare massive clusters (see Fig. (4.9)) [186]. It is clear from the Fig. (4.9) that the main contribution to the Poisson power spectrum comes from the clusters in the mass range of
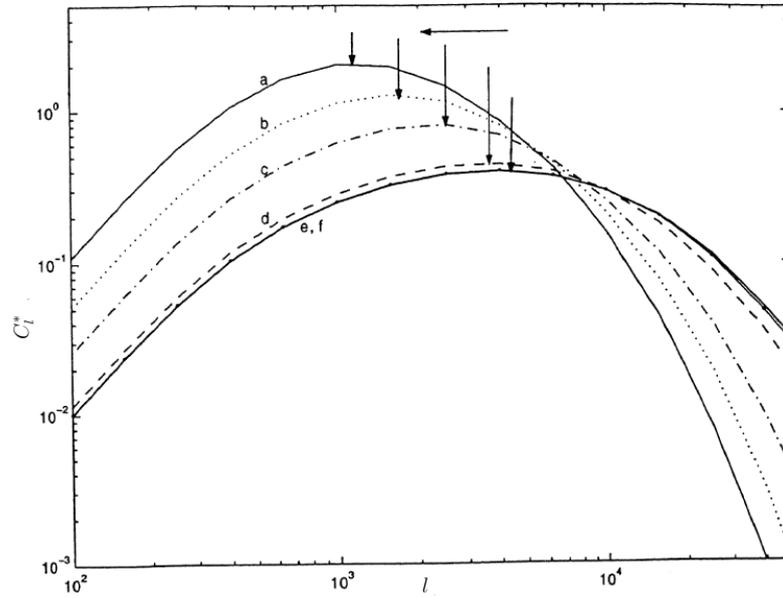
Figure 4.7: C_l^* is plotted for different maximum redshifts, z_{max} =0.5 (a), 0.7 (b), 1 (c), 2 (d), 3 (e), 5 (f) [50, 186].
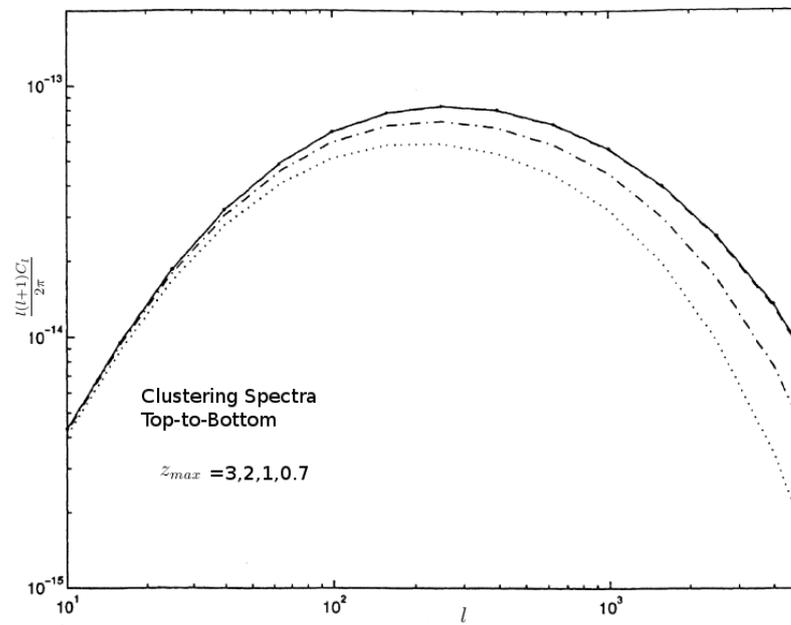

Figure 4.8: The S-Z clustering power spectra is plotted for different maximum redshifts: from top to bottom the z_{max} are 3 (thick solid line with dots), 2 (dashed line), 1 (dashed dot line), 0.7 (dotted line) [50, 186].
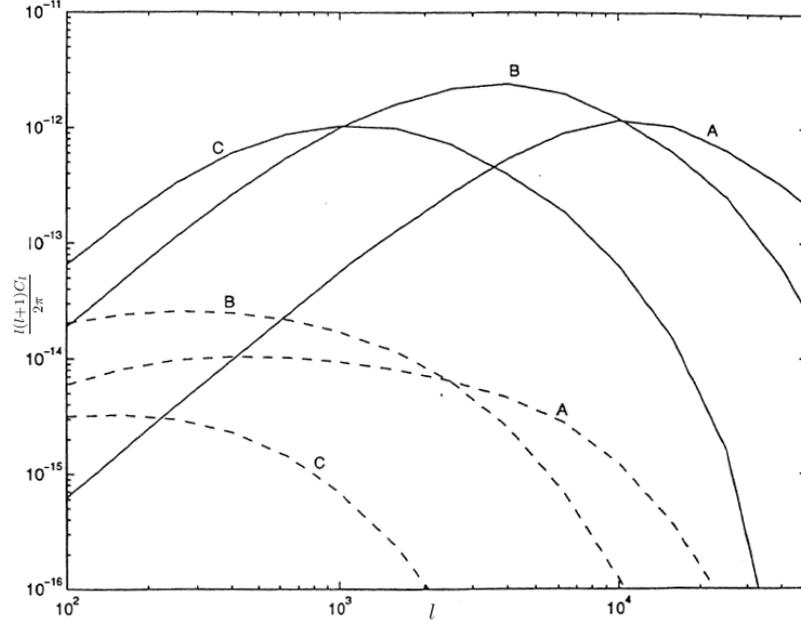
Figure 4.9: The S-Z power spectra is plotted for different mass ranges: A) $10^{13-14}M_\odot$, B)$10^{14-15}M_\odot$ and C)$10^{14-15}M_\odot$. The solid lines are for Poisson and dashed lines are for clustering power spectrum [50, 186].

$10^{14-15}M_\odot$. The higher mass clusters $M > 10^{15}M_\odot$ contribute less due to their dwindling number densities and lower mass one $M < 10^{14}M_\odot$ contribute less because their individual S-Z distortions is less due to lower T_e and smaller sizes. Similar trends are seen in the clustering power spectrum as well. Another feature that is immediately noticeable is that higher mass contribute at lower l values and vice versa.

4.7 Cluster Gas-Mass Fraction

Galaxy Clusters being perhaps the largest gravitationally bond structures in the universe, are expected to contain a significant amount of baryons of the universe. Moreover, due to their large angular sizes, it is easier to observationally estimate their total mass M_t, the gas mass M_g and hence the gas mass fraction ($f_g = \frac{M_g}{M_t}$). These estimates can be used as a probes of large scale structure of universe and underlying cosmological models.

The ICM contains most of the baryons confined to the cluster potential with is roughly an order of magnitude more baryonic mass than that observed in the galaxies

themselves [186]. The gas mass fraction (f_g) is therefore reasonable estimate of the baryonic mass fraction of the cluster. It should be also a reasonable estimate approximation of the universal baryon mass fraction, $f_b = \frac{\Omega_b}{\Omega_m}$, because it is not believed that mass segregation occurs on the large scales from which mass clusters condense $\sim 1000 \mathrm{Mpc}^3$. The cluster gas mass fraction is actually a lower limit $f_g \leq f_b$, because a small fraction of baryons ($\sim 10\%$) are likely lost during the cluster formation process [187, 188] and we cannot rule out the possibility of additional reservoirs of baryons in galaxy clusters that have yet to be detected.

A measurement of f_b leads directly to an estimate of Ω_m, given a determination of Ω_b. Recent reanalysis of big bang nucleosynthesis (BBN) predictions with careful uncertainty propagation [189, 190] along with deuterium to hydrogen ratio measurements in Lyman α clouds [191, 192] constrain the baryon density to be $\Omega_b h^2 = 0.019 \pm 0.0012$ at 68% confidence. Recent CMBR primary anisotropy experiments provide an additional independent determination of $\Omega_b h^2$ consistent with the Layman α cloud results [193, 194].

The gas mass is measured directly by observations of the S-Z effect, provided the electron temperature is known. The total gravitational mass can be measured by assuming the hydrostatic equilibrium and using the distribution of gas and, again the electron temperature. The S-Z effect derived gas mass fraction will therefore be proportional to $\frac{\Delta T}{T_e^2}$. Alternatively, the total gravitational mass can be determined by strong lensing (on small scales) or weak lensing (on large scales) [195]. Recently there has been considerable work on gas mass fractions using the total mass determinations derived under the assumption of hydrostatic equilibrium.

The S-Z effect derived gas mass fractions have been determined for two samples of clusters, and the results were used to place constrains on Ω_m: a sample of 4 nearby clusters [196] and a sample of 18 distant clusters [197]. Both the analyses used a spherical isothermal β-model for the ICM. The nearby sample was observed with the Owens valley 5.5-m telescope (OVRO) at 32 GHz as a part of an S-Z effect study of an X-ray flux-limited sample [196]. In this study the integrated S-Z effect was used to normalize a model for the gas density from published X-ray analyses and then compared to the published total mases to determine the total gas mass fraction. For three nearby clusters A2142, A2256 and the Coma cluster, a gas mass fraction of $f_g h = 0.061 \pm 0.011$ is found; for the cluster Abell 478 a gas mass fraction of $f_g h = 0.16 \pm 0.014$ is reported. The high redshift sample of 18 clusters ($0.14 < z < 0.83$) was observed interferometrically at 30 GHz using OVRO and BIMA S-Z effect imaging system. In this study, the model for the gas density

was determined directly by using the S-Z effect data, X-ray emission weighted electron temperatures were used, but no X-ray imaging data was used. Numerical simulations suggest, however, that the gas mass fraction at r_{500} (the radius inside of which the mean density of the cluster is 500 times the critical density) should reflect the universal baryon fraction. The derived gas mass fraction were therefore extrapolated to r_{500}. The resulting mean gas mass fraction are $f_g h = 0.081^{+0.009}_{-0.011}$ for $\Omega_m = 0.3$, $\Omega = 0.7$, $f_g h = 0.074^{+0.008}_{-0.009}$ for $\Omega_m = 0.3$, $\Omega = 0$ and $f_g h = 0.068^{+0.009}_{-0.008}$ for $\Omega_m = 0$, $\Omega = 0$. The uncertainties in the electron temperatures contribute the largest component to the error budget.

The angular diameter distance relation, $D_a(z)$, enters the gas fraction calculation and introduces a cosmology dependence on the results of the high z sample. In addition, the simulation scaling relations used to extrapolate the gas fractions to r_{500} have a mild dependence on cosmology. To estimate Ω_m, we need to account for the baryons contained in the galaxies and those lost during cluster formation. The galaxy contribution is assumed to be a fixed fraction of the cluster gas, with the fraction fixed at the value observed in the Coma cluster, $M_g^{true} = M_g^{obs}(1 + 0.20h^{\frac{3}{2}})$ [187]. Simulations suggest that the baryon fraction at r_{500} will be a modest underestimate of the true baryon fraction $f_g(r_{500}) = 0.9 \times f_b$(universal) [188]). These assumptions lead to $f_b = [f_g(1+0.2h^{\frac{3}{2}})/0.9]$. Using this to scale the gas fractions derived from the high z S-Z effect cluster sample and assuming $h = 0.7$ and a flat cosmology, leads to estimate $\Omega_m \sim 0.25$ [197].

Cluster gas mass fractions can also be determined from cluster X-ray emission in a similar manner as from S-Z effect measurements. However, there are important differences between X-ray and S-Z effect determined gas fractions. For example, the X-ray emission is more susceptible to clumping of the gas, C, since it is proportional to the ICM density squared. On the other hand, the X-ray derived gas mass is essentially independent of temperature for the ROSAT 0.1-2.4 keV band used in the analyses [198], while the S-Z effect derived gas mass is proportional to T_e^2.

Cluster gas mass fractions can also be measured by comparing S-Z effect derived gas masses and weak lensing derived total masses. The comparison is particularly interesting as both are measures of projected mass distributions. In addition, gas mass fractions can be derived without assuming a model for the cluster structure and without assuming hydrostatic equilibrium. Comparisons of S-Z effect and lensing data has only been done for a few clusters to date [199]. However, as for the S-Z effect, the quality and quantity of weak lensing observations toward galaxy clusters is rapidly increasing and several weak lensing surveys are underway. Holder et al. [199] demonstrated that gas mass fractions

can be determined from the analysis of S-Z effect and weak lensing measurements without need to parameterize the ICM distribution. Furthermore, by comparing this mass fraction with one derived by assuming hydrostatic equilibrium, it is possible to solve for the ICM electron temperature and the angular diameter distance.

S-Z effect surveys will provide a large catalog of galaxy clusters at redshifts $z > 1$. The increased sensitivity and larger angular dynamic range of the next generation of S-Z effect instruments will allow measurements of cluster gas fractions to r_{500} directly, greatly increasing the precision of the gas mass fractions. Moreover, extending the gas fraction analyses to high redshift will enable studies of the evolution of cluster structure. It should, for example, be straight forward to test speculative theories of dark matter decay [200].

4.8   Probing Evolution of f_g with S-Z Effect

The question as to whether there is any evolution (or constancy) of gas mass fraction, however, is still debatable, with claims made either way. For example, Schindler [201] has investigated a sample of distant clusters with redshifts between 0.3 to 1 and conclude that there is no evolution of the gas mass fraction. Similar conclusion has been drawn by Grego et al. [202]. On the contrary, Ettori & Fabian [203] have looked at 36 high-luminosity clusters, and find evolution in their gas mass fraction (in both SCDM and ΛCDM universes). Observations suggest that, though f_g of massive clusters ($T_e \geq 5\text{keV}$) appears to be constant, low mass clusters with shallower potential wells may have lost gas due to preheating and/or post-collapse energy input. It is also well known that ICM is not entirely primordial and there is probably continuous in-fall of gas, thereby, increasing f_g with time. Thus, there is considerable debate regarding the evolution of gas mass fraction. This section draws heavily upon the excellent work by Majumdar, S. [204].

Analytical studies and numerical simulations show that the gas density profile scales with the total density, and that the gas central electron density may be expressed as,

$$n_{e0} = f_g \frac{2\rho_0}{m_p(1 + \text{X})}, \tag{4.43}$$

where X= 0.69 is the average Hydrogen (proton) mass fraction and ρ_0 , the central mass density, is determined from the total mass by integrating a truncated King profile for the

total mass distribution,

$$\rho(r) \begin{cases} \rho_0 \left(1 + \frac{r^2}{r_c^2}\right)^{-\frac{3}{2}} & r \leq pr_c \\ 0 & r \geq pr_c \end{cases}, \tag{4.44}$$

with $p = 10$. Little is known about the total mass and redshift dependence of the intra-cluster gas from observations. Here, we adopt Colafrancesco & Vittorios model [205] which assumes that changes in the intra-cluster gas are driven by entropy variation and/or shock compression and heating. According to their model, the gas mass fraction may be expressed as,

$$f_g = f_{g0}(1 + z)^{-s} \left[\frac{M}{10^{15}h^{-1}M_\odot}\right]^k, \tag{4.45}$$

where the normalization, $f_{g0} = 0.1$, is based on local rich clusters. We look at combinations of both mass and redshift dependence for a range of evolutionary models. In particular, we look at a case of strong evolution given by $k = 0.5, s = 1$ (Colafrancesco & Vittorio) [205]; $k = 0.1, s = 0.5$ (Ettori & Fabian) [203]; $k = 0.1, s = 0.1$ (weak evolution); $k = 0$ (no mass dependence) and $s = 0$ (no redshift dependence).

Study of the primary anisotropies of the Cosmic Microwave Background can be used to determine the cosmological parameters to a very high precision. The power spectrum of the secondary CMBR anisotropies due to the thermal Sunyaev-Zeldovich Effect by clusters of galaxies, can then be studied, to constrain more cluster specific properties (like gas mass). We show the S-Z power spectrum from clusters to be a sensitive probe of any possible evolution (or constancy) of the gas mass fraction. The position of the peak of the S-Z power spectrum is a strong discriminatory signature of different gas mass fraction evolution models. For example, for a flat universe, there can be a difference in the l values (of the peak) of as much as 3000 between a constant gas mass fraction model and an evolutionary one. Moreover, observational determination of power spectrum, from blank sky surveys, is devoid of any selection effects that can possibly affect targeted X-ray or radio studies of gas mass fractions in galaxy clusters.

We have plotted the Poisson S-Z power spectrum in Fig. (4.10). Clearly, the primary feature distinguishing a non-evolutionary constant f_g model from an evolutionary one is the position of the peak. The model with a constant f_g peaks at a higher l value and also has greater power. The constant f_g model peaks at $l \sim 4000$. This result is in agreement with that of Komatsu & Kitayama [180]. If one assumes that there is no evolution of f_g
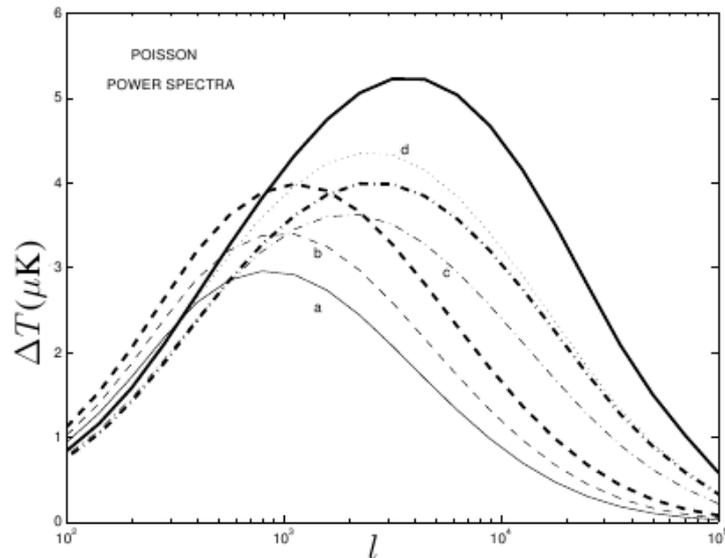
Figure 4.10: The Poisson power spectra due to S-Z effect from galaxy clusters for different f_g models. The thick solid line corresponds to constant f_g model, the thick dashed line has no evolution with redshift and the thick dash-dotted line has no evolution with total mass. The thin lines are for the cases: a) $k = 0.5, s = 1$; b) $k = 0.5, s = 0.5$; c) $k = 0.1, s = 0.5$ and d) $k = 0.1, s = 0.1$ [204].

with redshift (i.e $s = 0$), the peak is at $l \sim 1100$, whereas in the case of no dependence on mass ($k = 0$), the peak is at $l \sim 2500$. Based on EMSS data (David et al. [206]), Colafrancesco & Vittorio [205] model f_g with $k = 0.5, s = 1$. For this case, we see that the turnover is at a very low $l \sim 900$. Assuming a mild evolution ($k = 0.1, s = 0.1$), we get the peak at $l \sim 2100$. We also plotted results for ($k = 0.5, s = 0.5$) and ($k = 0.1, s = 0.5$). It is evident that the difference, in the l value of the peak of the constant f_g scenario from an evolutionary one, can range between $l \sim 1500 - 3200$. The position of the peak thus is a strong discriminatory signature of any evolution of f_g.

It is easy to understand the shift in the peak of the S-Z power spectrum. Let us consider the case $s = 0$, i.e. f_g depends only on total mass. From Eq. (4.44), this means an enhanced reduction of f_g of smaller mass clusters relative to the larger masses and so a reduction of power at larger l's, (since smaller masses contribute at larger l or smaller θ). Hence, the peak shifts to a lower l. For the case $k = 0$, (i.e only redshift dependence), we now have structures at high z contributing less to the power (than without a redshift dependence). Since from PS formalism, less massive structures are more abundant at high z, this negative dependence of f_g on redshift cuts off their contribution more than
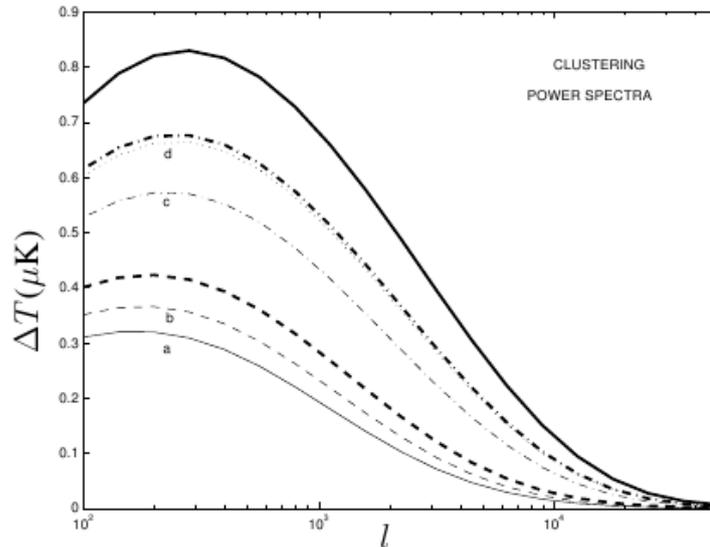
Figure 4.11: The Clustering power spectra due to S-Z effect from galaxy clusters for different f_g models. The thick solid line corresponds to constant f_g model, the thick dashed line has no evolution with redshift and the thick dash-dotted line has no evolution with total mass. The thin lines are for the cases: a) $k = 0.5$, $s = 1$; b) $k = 0.5$, $s = 0.5$; c) $k = 0.1$, $s = 0.5$ and d) $k = 0.1$, $s = 0.1$ [204].

the more massive clusters. Hence, once again there is less power at high l and the peak shifts to lower $l$value. The parametrization of Eq. (4.44) affects the larger masses less, as evident from almost equal power seen at $l \leq 600$, for all models. The net effect is a reduction of power at smaller angular scales, and hence a shift in the position of the peak to a smaller multipole value.

In Fig (4.11), we show the S-Z clustering power spectrum. For all models, it falls of at a smaller l w.r.t Poisson power spectrum. Since for clustering, the peak depends on the average inter-cluster separation, which is fixed once the cosmology is fixed, there is no appreciable spread of the peaks in l space. The only difference is in their relative power w.r.t each other which depends on the total gas mass available to distort the CMBR. Addition of the clustering power spectrum to the Poisson case results in slight shift of the peaks to lower l's.

In Fig. (4.12), we show results for an open universe ($\Omega_m = 0.35$, $\Omega_\Lambda = 0$, $h = 0.65$). It is clearly seen that the difference in the peak position of constant f_g and evolutionary models remain far apart (In-fact, for same parameters of $k = 0.5$, $s = 1$, the difference increases to ≈ 4500 from that of ≈ 3000 in a flat universe). It is seen that the turnover of
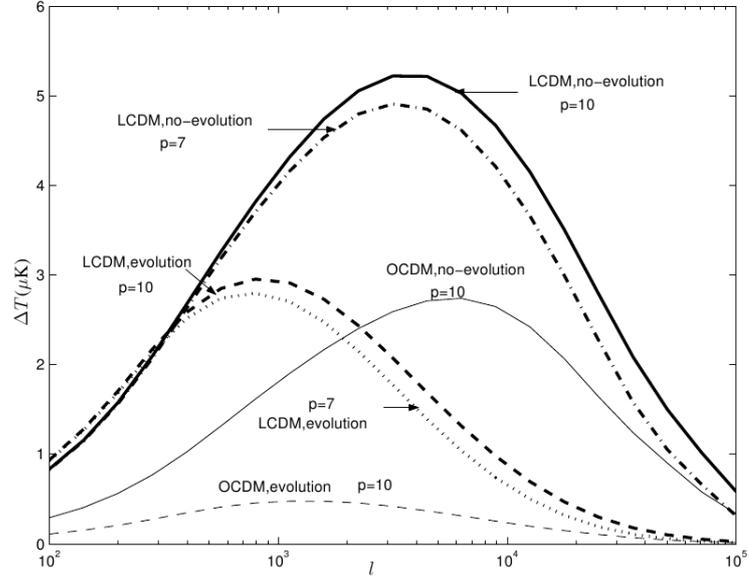
Figure 4.12: The Poisson S-Z power spectra are plotted for different cosmologies and with different extension of the gas mass. The solid lines are for a ΛCDM, with $\Omega_m = 0.35$, $\Omega_\Lambda = 0.65$, $h = 0.65$, and the thin lines are for OCDM with $\Omega_m = 0.35$, $\Omega_\Lambda = 0$, $h = 0.65$. The OCDM lines have been multiplied by a factor of 10 in the plot. The solid and dashed lines are for gas mass extending up to $10r_c$, whereas the dash-dotted and the dotted lines are for extension up to $7r_c$ [204].

the S-Z power spectrum is insensitive to the mass cutoff, since main contribution to the anisotropy comes from clusters with $10^{14}M_\odot < M < 10^{15}M_\odot$. In Fig. (4.12), we also indicate the effect of having a more compact gas distribution with $p = 7$. We see that shift in the peaks are negligible (though the height is reduced a little) and an uncertainty as to how far the gas extends is not major. The use of a single β to model the full gas distribution introduces little error, though a β-model fits the inner cluster regions better. This is because the major contribution to the anisotropy comes from around the core region, and increasing β slightly decreases the overall distortion, without touching the peak. In conclusion, we have computed the angular power spectrum of S-Z effect from clusters of galaxies. We have shown the position of the peak of the power spectrum to bear a strong discriminatory signature of different f_g models.

4.9 Summary

The shape of the CMBR anisotropy (primary and secondary) spectrum is directly linked to back ground cosmology. Thus understanding of physical mechanisms responsible for the anisotropy spectrum and the influence of the background cosmology in the generation of these anisotropies have led to attempts at deriving constraints on the cosmological parameters from the shape of CMBR anisotropy spectrum. In this chapter, we discussed methods of using Sunyaev-Zel'dovich effect in constraining cosmological parameters. One of the methods was based on measuring the evolution of the number density of galaxy cluster with redshift. We showed the cosmological dependence of Press-Schechter formalism and how it can be exploited in future S-Z surveys to constrain cosmological parameters. It was briefly discussed that measuring the evolution of the Press-Schechter number density of galaxy clusters would be a powerful probe of some cosmological parameters; in particular, matter density Ω_m, power spectrum normalization $\sigma(M)$, and the density (and possibly equation of state) of dark energy Ω_Λ. The significance being that the degeneracies between these parameters are different from those in primary anisotropies in the CMBR. Indeed, the redshift independence is the measure of such non-targeted S-Z surveys over traditional optical and X-ray observations. We also discussed a method of computing mass of galaxy clusters by determining best fit for NFW profile parameters. Secondly, we discussed nature of S-Z power spectrum in different cosmological models. We discussed a method of using power spectrum for different cosmologies to place constrains on the cosmological parameters in complimentary ways. To see this in details we concentrated on the ΛCDM and observed the effect of mass and redshift cutoff on the S-Z power spectrum. After discussing S-Z power spectrum in relation to cosmological parameters, we then discussed use of power spectrum as a probe of gas evolution in galaxy clusters. It is seen that the S-Z power spectrum from clusters is a sensitive probe of any possible evolution (or constancy) of the gas mass fraction and that the position of the peak of the S-Z power spectrum is a strong discriminatory signature of different gas mass fraction evolution models.

Chapter 5

Conclusions and Future Plan

5.1 Conclusions

The aim of the present work is to achieve a more profound understanding of the role of the Sunyaev-Zel'dovich effect as a probe of the large scale structure of the universe. We have presented an overview of the motivation for studying the S-Z effect, followed by an explanation of the physics. With Sunyaev-Zel'dovich effect, we have constrained angular diameter distance, Hubble constant, ICM, cosmological parameters and so on. The importance of the S-Z effect as a cosmological probe stands out since both kinds of intensity changes do not depend on redshift at all, thus the successful measurement of these changes can assist in studying cluster evolution, properties, and cosmological context in which the cluster is observed. We may summarize our main conclusions as follows:

• Sunyaev-Zel'dovich (S-Z) effect is based on the inverse Compton scattering, which is sensitive to the ICM. The interaction between CMBR photons and electrons guarantees the S-Z to be an important probe of large scale structure of universe. Compton scattering is completely understood physics, so the S-Z effect can be cleanly computed from first principles and the importance of S-Z effects stands out because unlike other astrophysical probes, it does not depend on the redshift. It turned out that comptonization parameter holds all the dependence on the large scale structures.

• Detailed analysis of the Kompaneets equation, suggests that the spectral features of the no-relativistic thermal S-Z effect do not depend on the temperature of the scattering medium. But in the relativistic limit, there is dependence on the temperature of ICM. However, these two formalisms are in excellent agreement with each other for electron

temperatures $T_e \leq 5$keV. Non-thermal S-Z effect in radio halos, quasars etc is found to be negligibly small as compared with the thermal S-Z effect, but must be accounted for precise measurements of cosmological parameters.

• The thermal S-Z effect can also prove to be a potential probe for intra-supercluster gas. Comparing such results from S-Z effect with the work already carried on superclusters from X-ray emission can be helpful in examining ISC.

• Kinematic S-Z effect appears to be small, except for the quasars where it dominates over thermal S-Z effect. Measurements of it placed constrains on cluster peculiar velocities, v_z. With next generation instruments, it may be possible, to measure polarization in S-Z signals. This measurement along with kinematic S-Z effect, would then give us vectorial velocity of clusters.

• Analysis of CMBR distortion due to S-Z effect in conjunction with cluster X-ray properties derived cluster morphology, cluster angular diameter distance and thus the estimate of Hubble constant. This method provides a distance determination for the cluster that is independent of cosmic distance ladder of Cephed variables or supernovae and is potentially effective at high redshifts.

• We discussed possible sources of both statistical and systematic uncertainty in our measurements and estimated their effect on the S-Z effect and X-ray derived cluster morphology. Some are found to have negligible effect on the measurements and it turns out non-isothermality, non-spherical, clumpiness of ICM can give rise to uncertainty in the measurements to a large extend.

• It is found that the cooling flow bulk motion contribution to the S-Z effect can reach for some clusters upto the percent level and thus can give correct analysis of the S-Z observations with cooling flows. Especially, in view of rapid progress in observational techniques, it may be possible to observe such deviations from standard thermal S-Z effect which will facilitate more exact measurements.

• Galaxy cluster catalogs are useful for cosmological studies for a number of reasons: cluster abundance, distribution and evolution reflect the structure formation process, which depends sensitively on certain cosmological parameters, such as the matter density Ω_m, Ω_Λ and $\sigma(M)$. S-Z effect will soon open the way to a new method of surveying for clusters. Several ground based instruments optimized for S-Z surveying are currently under construction and the Planck satellite will supply an almost fullsky catalog of several (104) clusters in next few years. We examined in detail this new kind of survey based on P-S formalism and the possible constrains in cosmological parameters.

• In the context of the upcoming surveys, we also showed that one could constrain cosmo-

logical parameters (or cosmological models) using S-Z angular power spectrum based on the theoretical P-S mass-redshift selection. Additionally, we estimated the contribution from the thermal S-Z effect and kinetic S-Z effect separately to the CMBR anisotropies and found that the kinematic S-Z signal is negligible compared to thermal S-Z effect.

• Lastly, we studied the impact of gas evolution on the expected yields from deep Sunyaev-Zeldovich effect surveys, as well as on the expected S-Z effect contribution on anisotropy in the cosmic microwave background in different cosmological models. We also showed that the position of the peak of the power spectrum is a strong discriminator between different f_g models.

5.2   Future of S-Z Effect

The Sunyaev-Zel'dovich effect has already been imaged in some ≈ 60 clusters, yielding important information on such quantities as the gas mass fraction in clusters, and the Hubble constant. Multi-frequency measurements of the effect in many more clusters are expected in the near future when new S-Z projects - both ground based and stratospheric become operational. In addition to the detection of the effect in a large number of clusters, planned sky surveys, particularly by the Planck satellite, will likely map the CMBR anisotropy induced by the effect. The much larger S-Z database and the measurement of this anisotropy will greatly expand the scope of the effect as a cosmological probe due to its strong dependence on the cosmological and large scale parameters, and the morphology and evolution of clusters.

Since the S-Z effect survey sensitivity is such a flat function of redshift, S-Z effect techniques should prove more effective at finding high-redshift clusters, and at locating clusters over a wider range of gas mass, than X-ray surveys. Plausible S-Z effect surveys are more effective at $z > 1$, if the clusters at such redshifts resemble those at low redshift. However, since we know that clusters assembled relatively recently, we might expect that S-Z-selected samples of clusters will be limited by the changing cluster sizes, gas contents, and coherence, and that there will be some maximum detectable redshift at which the gas in clusters first gains a high enough pressure to become the source of a significant S-Z effect. The distribution of clusters by redshift can also provide useful measures of cosmological parameters and tests of our models of cluster heating and evolution. Follow-up studies of a subsample of the clusters, with long X-ray observations and high-sensitivity,

high angular-resolution, S-Z-effect mapping, should provide excellent information on the physics of cluster formation, for example on the evolution of the cluster baryon fraction, or the changing distribution of cluster velocities . It would also provide an ideal set of clusters for the measurement of cluster distances and the determination of cosmological parameters, provided that enough structure information is available to allow good models of the gas distribution to be deduced for each cluster. It has even been shown that a comparison of a map of the S-Z effect with a gravitational lensing map can provide a rich set of information on cluster properties without conducting a redshift survey.

Along with the intensity signals, the S-Z effects also contain polarization signals. The simplest to understand is the polarization caused by multiple scatterings within the cluster, where one expects a radial pattern of polarization with intensity $\propto \tau_e \Delta I$. Other polarization signals are associated with motion of the cluster across the line of sight (with intensity $\propto I \frac{v_\perp}{c}$). This effect is extremely small, inaccessible to the current generation of instruments, and generally badly confused by background structures in the CMBR. However, this channel of the S-Z effect may become amenable to study with the next generation of instruments.

Thus, it is amply clear that a lot about the mystery and beauty of our universe is expected to be learnt in future with S-Z effect measurements.

Prospective Problems for Ph. D.

1) From the recent observations, the study of the temperature distribution in galaxy clusters has progressed significantly. Combining with the newly revealed temperature profiles, we can use the method shown in chapter 3 to study the real effects of the temperature distribution on the S-Z effect and then improve the accuracy of the estimated Hubble constant.

2) In addition to radio halos, there are many radio galaxies in clusters and it is found that there exist large fraction of relativistic non-thermal electrons in them. We plan to study the S-Z effect from these non-thermal electrons present in these cosmological structures and try to find its cosmological significance.

3) Accretion disks contain rotating hot gases. The CMBR photons may be scattered to higher energies by the electrons in this gas, resulting in the Sunyaev-Zel'dovich effect. This is an area in which little work has been done but warrants a thorough investigation.

4) With the current and up coming data on the blank sky surveys we aim to place a constrain on the Cosmological parameters by comparing observed cluster abundance and spatial distributions with specific model calculations.

Bibliography

[1] Gawiser, E.; Silk, J. (2000), *Physics Reports*, **333**, 245-267

[2] Durrer, R. (2008), *The Cosmic Microwave Background*, (Cambridge University Press, Cambridge, UK)

[3] Smoot, G. F. et al. (1992) , *APJ*, **396**, L1-L5

[4] Efstathiou, G.; Bond, J. R.; White, S. D. M. (1992), *MNRAS*, **33**, 1P-6P

[5] Sunyaev, R. A.; Zeldovich, Ya. B. (1980), *Annual Review of Astronomy and Astrophysics*, **18**, 537-560

[6] Sunyaev, R. A.; Zeldovich, Ya. B. (1980), *MNRAS*, **190**, 413-420

[7] Sunyaev, R. A.; Zeldovich, Ya. B. (1981), *Astrophysics and Space Physics Review*, **1**, 1-60

[8] Birkinshaw, M. (1999) *Physics Reports*, **310**, 97-195

[9] Holder, G. P.; McCarthy, I. G.; Babul, A. (2007), *MNRAS*, **382**, 1697-1706

[10] Cavaliere, A.; Fusco-Femiano, R. (1976), *A&A*, **49**, 137-144.

[11] Rephaeli, Y. (1995), *Annual Review of Astronomy and Astrophysics*, **33**, 541-580

[12] Shimon, M.; Rephaeli, Y. (2004), *New Astronomy*, **9**, 69-82

[13] Carlstrom, J. E.; Holder, G. P.; Reese, E. D. (2002), *Annual Review of Astronomy and Astrophysics*, **40**, 643-680

[14] Satoshi, N.; Yasuharu, K. (2009), *Physical Review D*, **79**, 083005

[15] Birkinshaw, M.; Lancaster, K. (2008), *A Pan-Chromatic View of Clusters of Galaxies and the Large-Scale Structure; Lecture Notes in Physics*, **740** (Springer, Dordrecht, The Netherlands), 255-286

[16] Haiman, Z.; Mohr, J.; Holder, P. (2001), *APJ*, **553**, 545-561

[17] Sealfon, C.; Verde, L.; Jimenez, R. (2006), *APJ*, **649**, 118-128

[18] Mauskopf, P. D. et al. (2000), *APJ*, **538**, 505-516

[19] Majumdar, S. (2001), *APJ*, **555**, L7-L10

[20] Weller, J.; Battye, R. A.; Kneissl, R. (2002), *Physical Review Letters*, **88**, id. 231301

[21] Colafrancesco, S. (2004), *JCAP*, **422** L23-L27

[22] Aghanim, N.; Gorski, K. M.; Puget, J. L. (2001), *A&A*, **374**, 1-12

[23] Plagge, T. et al. (2010), *APJ*, **716**, 1118-1135

[24] Reichardt, C. L. et al. (2009), *APJ*, **701**, 1958-1964

[25] Sharp, M. K. et al. (2010), *ApJ*, **713,**, 82-89

[26] Hincks, A. D. et al. (2010), *APJS*, **191**, 423-438

[27] Jarosik, N. et al. (2011), *APJS*, **192**, id.14

[28] Scott, D.; Smoot, G. (2006), *eprint arXiv:astro-ph/0601307*

[29] Nolta, M. R. et al. (2004), *APJ*, **608**, 10-15

[30] Sachs, R. K.; Wolfe, A. M. (1967), *APJ*, **147**, 73

[31] Peebles, P. J. E.; Yu, J. T. (1970), *APJ*, **162**, 185

[32] Scott, D.; Silk, J.; White, M. (1995), *Science*, **268**, 829-835

[33] Silk, J. (1968), *APJ* , **151**, 459

[34] Rephaeli, Y; Sadeh, S. (2009), *Modern Physics Letters A*, **23**, 1498-1505

[35] Refregier, A.; Komatsu, E.; Spergel, D. N.; Pen, Ue-Li. (2000), *Physical Review D*, **61**, id.123001

[36] Cohn, J. D.; Kadota, K. (2005), *APJ* , **632**, 1-14.

[37] Blumenthal, G. R.; Gould, R. J. (1970), *Reviews of Modern Physics*, **42**, 237-271

[38] Padmanabhan, T. (2000), *Theoretical Astrophysics. Vol.1: Astrophysical processes*, (Cambridge University Press, 2000)

[39] Rybicki, G. B.; Lightman, A. P. (1979), *Radiative processes in astrophysics*, (New York, Wiley-Interscience, 1979), p393

[40] McQuinn, M. et al. (2005), *APJ*, **630**, 643-656

[41] Majumdar, S.; Nath, B. B.; Chiba, M. (2001), *MNRAS*, **324**, 537-546

[42] Babich, D.; Loeb, A.(2007), *MNRS*, **374**, L24-L28

[43] de Zotti, G (2004), *AIP Conference Proceedings*, **703**, 375-384

[44] Oh, S. P.; Cooray, A.; Kamionkowski, M. (2003), *MNRAS*, **342**, L20-L24

[45] Kompaneets, A. S. (1957), *Soviet Physics JETP*, **4**, 730

[46] Jonathan, I. k. (1986), *High Energy Astrophysics*, (Benjamin/Cumming Publishing Co., Inc.)

[47] Zeldovich, Ya. B.; Sunyaev, R. A. (1969), *Astrophysics and Space Science*, **4**, 301-316

[48] Shao, j.; Zhang, P.; Lin W. (2011), *APJ*, **730**, 127

[49] Staniszewski, Z. et al. (2009), *APJ*, **701**, 32-41

[50] Majumdar, S. (1999), *Indian Journal Physics*, **73B** 835 - 842

[51] Zemcov, M.; Borys, C.; Halpern, M.; Mauskopf, P.; Scott, D. (2007), *MNRAS*, **376**, 1073-1098

[52] Bernstein, J.; Dodelson, S. (1990), *Physical Review D*, **41**, 354373

[53] Wright, E. L. (1979), *APJ*, **232**, 348-351

[54] Taylor, G. B.; Wright, E. L. (1989), *APJ*, **339**, 619-628.

[55] Rephaeli, Y. (1995), *APJ*, **445**, 33-36

[56] Chandrasekhar, S. (1950), *Radiative transfer*, (Oxford, Clarendon Press)

[57] Loeb, A.; McKee, C. F.; Lahav, O. (1991), *APJ*, **374**, 44-56

[58] Colafrancesco, S.; Marchegiani, P.; Palladino, E. (2003), *A&A*, **397**, 27-52

[59] Shimon, M.; Rephaeli, Y. (2002), *APJ*, **575**, 12-17

[60] Blasi, P.; Olinto, A. V.; Stebbins, A. (2000), *APJ*, **535**, L71-L74

[61] Bahcall, N. A.; Lubin, L. M.; Dorman, V. (1995), *APJ*, **447**, L81

[62] David, L. P.; Jones, C.; Forman, W. (1991), *APJ*, **445**, 578-590

[63] Gramann, M.; Bahcall, N. A.; Cen, R; Gott, J. R. (1995), *APJ*, **441**, 449-457

[64] Bahcall, N. A.; Gramann, M.; Cen, R. (1994), *APJ*, **436**, 23-32

[65] Cen, R.; Ostriker, J. P. (1993), *APJ*, **417**, 404

[66] Elbaz, D.; Arnaud, M.; Vangioni-Flam, E. (1995), *APJ*, **303**, 345

[67] Matteucci, F.; Gibson, B. K. (1995), *A&A*, **304**, 11

[68] Metzler, C. A.; Evrard, A. E. (1994), *American Astronomical Society*, **26**, 1402

[69] Anninos, P; Norman, M. L. (1996), *APJ*, **459**, 12

[70] Rephaeli, Y.; Persic, M. (1992), *MNRS*, **259**, 613-616

[71] Persic, M.; Rephaeli, Y.; Boldt, E. (1988), *APJ*, **327**, L1-L3

[72] Persic, M.; Jahoda, K.; Rephaeli, Y.; Boldt, E.; Marshall, F. E.; Mushotzky, R. F.; Rawley, G. (1990), *APJ*, **364**, 1-6

[73] Day, C. S. R.; Fabian, A. C.; Edge, A. C.; Raychaudhury, S. (1991), *MNRAS*, **252**, 394-402

[74] Bardelli, S.; Zucca, E.; Malizia, A.; Zamorani, G.; Scaramella, R.; Vettolani, G. (1996), *A&A*, , 435

[75] Banday, A. J.; Gorski, K. M.; Bennett, C. L.; Hinshaw, G.; Kogut, A.; Smoot, G. F. (1996), *APJ*, **468**, L85

[76] Rephaeli, Y.; Lahav, O. (1991), *APJ*, **372**, 21-24

[77] Peiris, H. V.; Smith, T. L. (2010), *Physical Review D*, **81**, id 123517

[78] Cunnama, D.; Faltenbacher, A.; Cress, C.; Passmoor, S. (2009), *MNRAS*, **397**, L41-L45

[79] Martin G.; Haehnelt, M. T. (1996), *MNRAS*, **279**, 545-556

[80] Kashlinsky, A.; Atrio-Barandela, F.; Kocevski, D.; Ebeling, H. (2009), *APJ* , **691**, 1479-1493

[81] Phillips, P. R. (1995), *APJ*, **55**, 419

[82] Nozawa, S.; Itoh, N.; Kohyama, Y. (1998), *APJ*, **508**, 17-24

[83] Sunyaev, R. A.; Zeldovich, Ya. B. (1972), *Comments on Astrophysics and Space Physics*, **4**, 173

[84] Nottale, L. (1984), *MNRAS*, **206**, 713-727

[85] Pyne, T.; Birkinshaw, M. (1993), *APJ*, **415**,459

[86] Holzapfel, W. L.; Ade, P. A. R.; Church, S. E.; Mauskopf, P. D.; Rephaeli, Y.; Wilbanks, T. M.; Lange, A. E. (1997), *APJ*, **481**, 35

[87] LaRoque, S. J.; Carlstrom, J. E.; Reese, E. D.; Holder, G. P.; Holzapfel, W. L.; Joy, M.; Grego, L. (2002), *eprint arXiv:astro-ph/0204134*

[88] Benson, B. A. et al. (2003), *APJ*, **592**, 674-691

[89] Aghanim, N.; Desert, F. X.; Puget, J. L.; Gispert, R. (1996), *A&A*, **311**, 1-11

[90] Loeb, A. (1996), *APJ*, **471**, L1

[91] Natarajan, P.; Sigurdsson, S. (1997), *eprint arXiv:astro-ph/9704237*

[92] Andernach, H.; Wielebinski, R.; Schlickeiser, R.; Sholomitski, G. B. (1986), *A&A* , **169**, 78-84

[93] Jones, M. E. et al. (1997), *APJL*, **479**, L1

[94] Rephaeli, Y.; Yankovitch, D. (1997), *APJL*, **481**, L55

[95] Reese, E. D. et al. (2002), *APJ*, **581**, 53-85

[96] Mason, B. S.; Myers, S. T.; Readhead, A. C. S. (2001), *APJ*, **555**, L11-L15.

[97] Cen, R. (1998), *APJL*, **498**, L99

[98] Schmidt, R. W.; Allen, S. W.; Fabian, A. C. (2004), *MNSRS*, **352**, 1413-1420

[99] Lin, W.; Norman, M. L.; Bryan, G. L. (2003), *eprint arXiv:astro-ph/0303355*

[100] Peebles, P. J. E. (2003), *Principles of Physical Cosmology*, (Princeton Series in Physics)

[101] Hogg,D. W. (1999), *eprint arXiv:astro-ph/9905116*

[102] Carrol, B. W.; Ostlie, D.A. (1996), *An Introduction to Modern Astrophysics*, (Pearson, Addison-Wesley)

[103] Bransden, B. H.; Joachaim, C. J (1992), *Physics of Atoms and Molecules*, (Wiley, New York)

[104] Longair, M. S. (1992), *High Energy Astrophysics*, (Cambridge University Press)

[105] Cao, L.; Zhang Y. Z.; Zhu Z. H. (2001), *Chinese Physics Letters*, **18**, 622

[106] Arnaud, M. (2009), *A&A*, **500**, 103-104

[107] Cavaliere, A.; Fusco-Femiano, R. (1976), *A&A*, **49**, 137-144

[108] Sarazin, C. L. (1988), *X-ray emission from clusters of galaxies*, (Cambridge Astrophysics Series, Cambridge: Cambridge University Press)

[109] King, I. R. (1966), *APJ*, **71**, 64

[110] King, I. R. (1962), *APJ*, **67**, 471

[111] Ikebe, Y. et al. (1996), *Nature*, **379**, 427-429

[112] Haiguang X. et al. (1998), *APJ*, **500**, 738

[113] Navarro, J. F.; Frenk, C. S.; White, S. D. M. (1995), *MNRAS*, **275**, 720-740

[114] Navarro, J. F.; Frenk, C. S.; White, S. D. M. (1997), *APJ*, **490**, 493

[115] Arnaud, M.; Pratt, G.W.; Piffaretti, R.; Boehringer, H.; Croston, H.; Pointecouteau, E. (2010) *A&A* **517**, id A92

[116] Inagaki, Y.; Suginohara, T.; Suto, Y. (1995), *Publications of the Astronomical Society of Japan*, **47**, 411-423

[117] Birkinshaw, M.; Hughes, J. P.; Arnaud, K. A. (1991), *APJ*, **379**, 466-481

[118] Hughes, J. P.; Birkinshaw, M. (1998), *APJ*, **501**, 1

[119] Mason, B. S.; Myers, S. T.; Readhead, A. C. S. (2001), *APJ*, **555**, L11-L15

[120] Kawahara, H.; Kitayama, T.; Sasaki, S.; Suto, Y. (2008), *APJ*, **674**, 11-21

[121] Roettiger K.; Stone1, J. M.; Mushotzky R. F. (1997), *APJ*, **482**, 588

[122] Yoshikawa, K.; Itoh, M.; Suto, Y.(1998), *Publications of the Astronomical Society of Japan*, **50**, 203-211

[123] Reese, E. D.; Kawahara, H.; Kitayama, T.; Ota, N.; Sasaki, S.; Suto, Y. (2010), *APJ*, **721**, 653-669

[124] Hughes, J. P.; Gorenstein, P.; Fabricant, D. (1988), *APJ*, **329**, 82-96

[125] Wang, Y.; Fan, Z.(2006), *APJ*, **643**, 630-640

[126] Puy, D.; Grenacher, L.; Jetzer, Ph.; Signore, M. (2000), *A&A*, **363**, 415-424

[127] Mathiesen, B.; Evrard, A. E.; Mohr, J. J. (1999), *APJ*, **520**, L21-L24

[128] Nagai, D.; Lau, E. T. (2011), *APJ*, **731**, L10

[129] Mohr, J. J.; Mathiesen, B.; Evrard, A. E. (1999), *APJ*, **517**, 627-649

[130] Kobayashi, S.; Sasaki, S.; Suto, Y. (1996), *Publications of the Astronomical Society of Japan*, **48**, L107-L111

[131] Holanda, R. F. L.; Cunha, J. V.; Marassi, L.; Lima, J. A. S. (2010), *eprint arXiv:1006.4200*

[132] Loeb, A.; Refregier, A. (1996), *eprints arXiv:astro-ph/9610048v1*

[133] Cowie, L. L.; Binney, J. (1977), *APJ*, **215**, 723-732

[134] Fabian, A. C. (1994), *Annual Review of Astronomy and Astrophysics*, **32**, 277-318

[135] Nulsen, P. E. J. (1986), *MNRAS*, **221**, 377-392

[136] Fabian, A. C.; Arnaud, K. A.; Nulsen, P. E. J.; Mushotzky, R. F. (1986), *APJ*, **305**, 9-13

[137] Mathews, W. G.; Bregman, J. N. (1978), *APJ*, **224**, 308-319

[138] Fabian, A. C.; Nulsen, P. E. J.; Canizares, C. R. (1984), *Nature*, **310**, 733-740

[139] White, Raymond E., III; Sarazin, Craig L. (1987), *APJ*, **318**, 612-620

[140] White, Raymond E., III; Sarazin, Craig L. (1987), *APJ*, **318**, 629-644

[141] Sarazin, Craig L.; White, Raymond E., III (1987), *APJ*, **320**, 32-48

[142] Koch, P. M.; Jetzer, Ph.; Puy, D.(2002), *New Astronomy, Volume*, **7**, 587-593

[143] Psaltis, D.; Lamb, F. K. (1997), *APJ*, **488**, 881

[144] Molnar, S. M.; Birkinshaw, M.; Mushotzky, R. F. (2002), *APJ*, **570**, 1-16

[145] Lange, A. E. et al. (2001), *Physical Review D*, **63**, 4

[146] Press, W. H. Schechter, P.; (1974), *APJ*, **187**, 425-438

[147] Padmanabhan, T.; Subramanian, K. (1992), *Astronomical Society of India, Bulletin*, **20**, 1-155

[148] Cooray, A. (2001), *Physical Review D*, **64**, id.063514

[149] Holder, G.; Haiman, Z.; Mohr, J. J. (2001) *APJ*, **560**, L111-L114

[150] Komatsu, E.; Seljak U. (2002), *MNRAS*, **336**, 1256-1270

[151] Jenkins, A. et al. (2001), *MNRAS*, **321**, 372-384

[152] Lacey, C.; Cole, S. (1993), *MNRAS*, **262**, 627-649

[153] Mohr, J. J. (2001), *AMiBA 2001: High-Z Clusters, Missing Baryons, and CMB Polarization, ASP Conference Proceedings*, **257**, (Astronomical Society of the Pacific, San Francisco), 49

[154] Holder, G. P.; Mohr, J. J.; Carlstrom, J. E.; Evrard, A. E.; Leitch, E. M. (2000), *APJ*, **544**, 629-635

[155] Haiman, Z.; Mohr, J. J.; Holder, G. P. (2001), *APJ*, **553**, 545-561

[156] Battye, R. A.; Weller, J. (2003), *Physical Review D*, **68**, id. 083506

[157] Sehgal, N. et al. (2011), *APJ*, **732**, id. 44

[158] Shang, C.; Haiman, Z.; Verde, L. (2009), *MNRAS*, **400**, 1085-1104

[159] Bahcall, N.; Dong, F.; Bode, P.; SDSS Collaboration (2002), *American Astronomical Society*, **34**, 1142

[160] Rosati, P.; Borgani, S.; Norman, C. (2002), *Annual Review of Astronomy and Astrophysics*, **40**, 539-577

[161] Reiprich, T. H.; Bohringer, H. (2002), *APJ*, **567**, 716-740

[162] Stanek, R.; Evrard, A. E.; Bhringer, H.; Schuecker, P.; Nord, B. (2006), *APJ*, **648**, 956-968

[163] Mantz, A; Allen, S. W.; Rapetti, D.; Ebeling, H.; Drlica-Wagner, A. (2010), *American Astronomical Society*, **41**, 713

[164] Vikhlinin, A.; Markevitch, M.; Murray, S. S.; Jones, C.; Forman, W.; Van Speybroeck, L. (2005), *APJ*, **628**, 655-672

[165] Peterson, J. R. et al. (2001), *APJ*, **365**, L104-L109

[166] Markevitch, M. (2011), *eprint arXiv:0705.3289*

[167] Peng, F.; Nagai, D. (2009), *APJ*, **693**, 839-846

[168] Mroczkowski, T. et al. (2009), *APJ*, **694**, 1034-1044

[169] Schwarzschild, M. (1958), *Structure and Evolution of stars*, (princeton university press)

[170] Kippenhahn, R.; Weigert, A. (1990), *Stellar structure and evolution* , (Springer-Verlag)

[171] Gnedin, O. Y.; Kravtsov, A. V.; Klypin, A. A.; Nagai, D. (2004), *APJ*, **616**, 16-26

[172] Rudd, D. H.; Zentner, A. R.; Kravtsov, A. V. (2008), *APJ*, **672**, 19-32

[173] Mroczkowski, T. (2011), *APJL*, **728**, L35

[174] Rephaeli, Y. (1981), *APJ*, **245**, 351-356

[175] Makino, N.; Suto, Y. (1993), *APJ*, **407**, 1-7

[176] Bartlett, J. G.; Silk, J. (1994), *APJ*, **423**, 12-18

[177] Colafrancesco, S.; Mazzotta, P.; Rephaeli, Y.; Vittorio, N. (1994), *APJ*, **433**, 454-463

[178] Colafrancesco, S.; Mazzotta, P.; Rephaeli, Y.; Vittorio, N. (1997), *APJ*, **479**, 1

[179] da Silva, A. C.; Barbosa, D.; Liddle, A. R.; Thomas, P. A. (2000), *MNRAS*, **317**, 37-44

[180] Komatsu, E.; Kitayama, T. (1999), *APJ*, **526**, L1-L4

[181] Molnar, S. M.; Birkinshaw, M. (2000), *APJ*, **537**, 542-554

[182] Cooray, A.; Hu, W.; Tegmark, M. (2000), *APJ*, **540**, 1-13

[183] Rephaeli, Y.; Sadeh, S. (2008), *Modern Physics Letters A*, **23**, 1498-1505

[184] Cole, S.; Kaiser, N. (1988), *MNRAS*, **233**, 637-468

[185] Komatsu, E.; Kitayama, T.; Refregier, A.; Spergel, D. N.; Pen, U. (2000), *eprints arXiv:astro-ph/0012196*

[186] Majumdar, S. (2001) P. hD Thesis

[187] White, S. D. M.; Efstathiou, G.; Frenk, C. S. (1993), *MNRAS*, **262**, 1023-1028

[188] Evrard, A. E. (1997), *MNRAS*, **292**, 289

[189] Nollett, K. M.; Burles, S. (2000), *The Light Elements and their Evolution*, (Proceedings of IAU Symposium)

[190] Burles, S.; Nollett, K. M.; Truran, J. W.; Turner, M. S. (1999), *Physical Review Letters*, **82**, 4176-4179

[191] Burles, S.; Tytler, D. (1998), *APJ*, **499**, 699

[192] Burles, S.; Tytler, D. (1998), *APJ*, **507**, 732-744

[193] Pryke, C. et al. (2002), *APJ*, **568**, 46-51

[194] Netterfield, C. B. et al. (2002), *APJ*, **571**, 604-614

[195] Waxman, E.; Miralda-Escude, J. (1995), *APJ*, **451**, 451

[196] Myers, S. T.; Baker, J. E.; Readhead, A. C. S.; Leitch, E. M.; Herbig, T. (1997), *APJ*, **485**, 1

[197] Grego, Laura et al. (2001), *APJ*, **552**, 2-14

[198] Mohr, J. J.; Mathiesen, B.; Evrard, A. E. (1999), *APJ*, **517**, 627-649

[199] Holder, G. P.; Carlstrom, J. E.; Evrard, A. E. (2000), *Constructing the Universe with Clusters of Galaxies*, (IAP 2000 meeting, Paris, France)

[200] Cen, R. (2001), *APJ*, **546**, L77-L80

[201] Schindler, S. (1999), *A&A*, **349**, 435-447

[202] Laura, G. et al. (2000), *eprint arXiv:astro-ph/0012067v1*

[203] Ettori, S.; Fabian, A. C. (1999), *MNRAS*, **305**, 834-848

[204] Majumdar, S. (2001), *APJ*, **555**, L7-L10

[205] Colafrancesco, S.; Vittorio, N. (1994), *APJ*, **422**, 443-458

[206] David, L. P.; Arnaud, K. A.; Forman, W.; Jones, C. (1990), *APJ*, **356**, 32-40